THE UNIVERSITY of ADELAIDE

Thesis submitted for the degree of

Master of Philosophy

Studies of TeV Gamma-Ray Sources in the Hydrogen-Alpha Optical Line

Rami Alsulami

15th January 2020

Supervisors:

A/Prof. Gavin Rowell

A/Prof. Gary Hill

Faculty of Sciences

School of Physical Sciences

Department of Physics

The University of Adelaide

Principal Superviso:	A/Prof. Gavin Rowell
Co-Supervisor:	A/Prof. Gary Hill
Date of Submission:	15th January 2020

Abstract

The first way humanity explored our Milky Way Galaxy and the Universe was through optical light observations. That led us to explore the cosmos using different electromagnetic wavebands such X-rays, gamma-rays, and radio wavelengths. Since then multi-wavelength studies of sources have started to explain their physical properties. The links between the TeV (10^{12} eV) gamma-ray emission of HESS J1825-137 and an optical supernova remnant (SNR) G18.7-2.2 is helping us to understand the interstellar medium (ISM) in multiple different wavebands (Voisin et al., 2016). G18.7-2.2 is observed in optical Hα, and has a spectral intensity ratio of ionised sulphur to Hα [S II] / Hα indicating that it is a SNR. There is a need to look for similar counterparts in Hα towards TeV gamma-ray surveys that have some interesting features. We use the archival data from optical Hα survey, as well as the HESS galactic plane survey (HGPS), looking for attributes that may link the two emission channels. Moreover, other radio and X-ray surveys are used with some HESS candidates to provide more evidence in different electromagnetic wavelengths. A model is used to calculate the SNR radius as a function of age and density, where this age has been inferred from the energetic pulsars which have been left behind in the formation of the SNR. Additionally, a stellar wind bubble (SWB) model is used to estimate the radius of the stellar wind shock produced by the SNR progenitor star. In this work, There are some TeV sources that have no features in the Hα. However, there are many notable candidates that have been investigated in this study. We found that HESS J1356-645. HESS J1912+101 and HESS J1804-216 have an arcs in the optical Hα line which indicates a plausible relationship. HESS J1303-631 and HESS J1640-465 have an interesting Hα emission

morphology that may be related to the stellar wind bubble created by the progenitor star. Finally, we present the unique Hα jet structure and the bow shock morphology in the region of HESS J1826-148 which may be linked to a powerful microquasar in the galactic plane.

Declaration of Originality

I certify that this work contains no material which has been accepted for the award of any other degree or diploma in my name in any university or other tertiary institution and, to the best of my knowledge and belief, contains no material previously published or written by another person, except where due reference has been made in the text. In addition, I certify that no part of this work will, in the future, be used in a submission in my name for any other degree or diploma in any university or other tertiary institution without the prior approval of the University of Adelaide and where applicable, any partner institution responsible for the joint award of this degree.

I give consent to this copy of my thesis, when deposited in the University Library, being made available for loan and photocopying, subject to the provisions of the Copyright Act 1968.

I also give permission for the digital version of my thesis to be made available on the web, via the University's digital research repository, the Library Search and also through web search engines, unless permission has been granted by the University to restrict access for a period of time.

Date

Signature

Acknowledgements

I would first like to thank my thesis advisor Assoc. Prof. Gavin Rowell of the school of Physical Sciences at The University Of Adelaide. The door to Assoc. Prof. Rowell's office was always open whenever I ran into trouble or had a question about my research or writing. He consistently allowed this thesis to be my own work, but steered me in the right the direction whenever he thought I needed it.

I would also like to thank other the experts who were involved in the helping me in this thesis work: Dr. Sabrina Einecke, Dr. Fabien Voisin, Peter Marinos, Kristy Feijen. Also, would also like to thank my friends Salem Alshamsi, Adam Virgili, Minh for helping me.

I would like to thank The Virginia Tech Spectral-Line Survey (VTSS), the Southern H-Alpha Sky Survey Atlas (SHASSA), the Wisconsin H-Alpha Mapper (WHAM) are all funded by the National Science Foundation. I also acknowledge the access to the data and software that forms the on-line SuperCOSMOS H-alpha Survey (SHS) of the Southern Galactic plane.

This work was done as part of the scholarship provided by King Abdulaziz University. I would also like to acknowledge Prof. Hassan Basurah and the Astronomy department at KAU as the supporter for me all the time. And Dr. Hassan Asiri head of the Astronomy department at KAU, for whom I am gratefully indebted to for his for very valuable comments on this thesis.

Finally, I must express my very profound gratitude to my parents and to my friends for providing me with unfailing support and continuous encouragement throughout my years of study and through the process of researching and writing this thesis.

This accomplishment would not have been possible without them. Thank you.

Contents

List of Figures

List of Tables

1 Introduction

The study of the Universe is one of the key drivers of human curiosity. The understanding of how the interstellar med (ISM) emits across the electromagnetic spectrum from their interactions with shock waves transmitted by nearby active sources is developing. Supernova explosions are some of the most violent shock waves that occur in the cosmos. As such, scientists, especially astrophysicists, work in analysing observational data and simulation models of titanic explosions to gain the maximum possible insight into the associated gas interactions.

1.1 Searching For Optical Supernova Remnants Towards TeV Gamma-ray Sources

Studies of supernovae (SN) and the structure and mechanism of the ISM help us understand how the ISM is constructed. In this thesis, we discuss the search for supernova remnants (SNRe), potentially associated with TeV gamma-ray sources. Stars with a mass of more than 5 to 10 solar mass ($M_{\odot}$) will end their life as SNe, with the explosions surrounding them with ionised gas. The environment of SN explosions are observable in the optical band for a few months after they occur. During this time the SNR will start to radiate. The resulting structure of the SNR depends on the mass of the progenitor star and the surrounding environment of the interstellar medium (ISM) which interacts with the SN shock wave. These classifications arise from the existence of the hydrogen spectral line. If this is observed, the SN is type II, and

otherwise, it is type Ia. These two main types of SN (see Figure 1.1), are described as follows:

- Type Ia results from a binary star system in which a white dwarf orbits a larger star. As the white dwarf accumulates the material from the companion star until it exceeds the Chandrasekhar limit ($< 1.4 M_{\odot}$), at which point it undergoes a supernova explosion. These supernovae are known for their lack of hydrogen emission lines (Weiler and Sramek, 1988).

- Type II (Core collapse) is powered by gravitation and occurs for massive stars larger than 8 $M_{\odot}$. These explosions are fainter than type Ia by 2.5 orders of magnitude (Weiler and Sramek, 1988). There are two different subtypes, type Ic and Ib. In type Ib the Si II(6150 Å) emission line is absent, whereas Ic is associated with more massive stars which have less Helium (He). As a result, the hydrogen (H) and He emission lines are less intense in type Ic SNe.

As SNRs interact with the surrounding ISM, providing the shell edge with a large amount of energy they form a variety of morphologies, enabling their detection in several ways. One of these is via optical arcs, which remain detectable for up to a million years due to the initial speed of the ejected material, and the subsequent deceleration caused by collisions with the ISM around the progenitor star (Reynolds, 2008).

Many expected SNRs have been discovered using other wavelength bands such as radio, X-rays or even gamma-rays which show possible candidate SNRs created in the galactic plane (Green, 2019). There are also a few new SNRs, candidates discovered in the TeV gamma-ray band (H.E.S.S. Collaboration, 2018a). However, the optical detection of SNRs still provides important clues in terms of whether the candidate is related to an SNR.

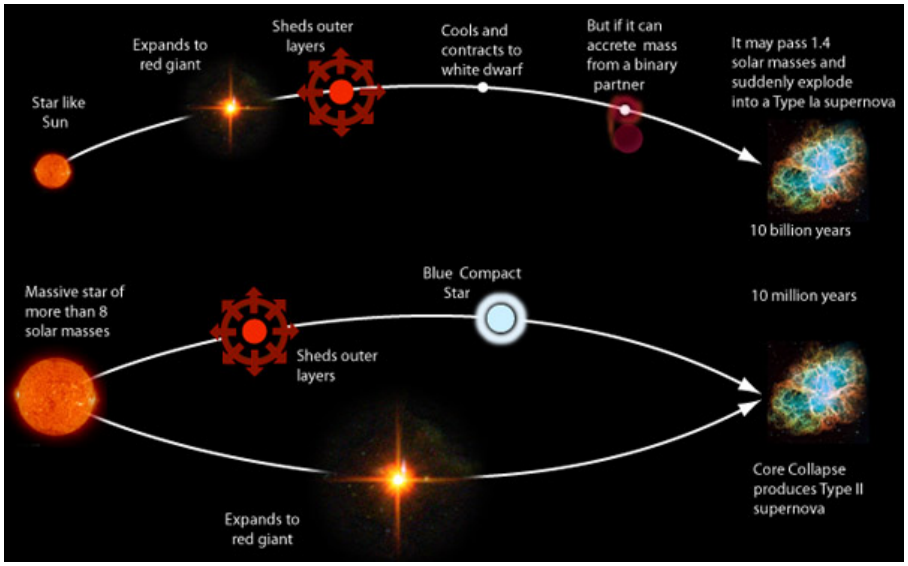

Figure 1.1: Formation of both types of supernova (SN): (Top) Type 1a, showing the interaction with binary companion star; (Bottom) core collapse , which occurs when there is no nuclear fusion in the core of the star.

This thesis will discuss the usage of the High-Energy Stereoscopic System (HESS) which studies TeV gamma-rays using Cherenkov light in the atmosphere. The HESS galactic plane survey (HGPS) that covers the gamma-ray sources in our galaxy was recently updated. Figure 1.2 shows the HESS survey result, which covers $b \leqslant \pm 3^{\circ}$ and $l = 260$ to 65°, and has more than 78 sources (H.E.S.S. Collaboration, 2018b).

Over half of these gamma-ray sources are still unidentified with no obvious counterparts in other wavebands. Figure 1.3 shows the number of sources, and how many of these are known and classified as supernova remnants (SNRs) shell, pulsar wind nebulae (PWN), binary systems, which is a system of two stars orbiting around common barycenter, composite that contain SNR shell and PWN, not associated with any known high energy sourc, or unidentified. Some of the TeV SNRs have been detected via optical emission lines such as Hα. However, around eight of the SNR sources were identified from HGPS (table 1.1).

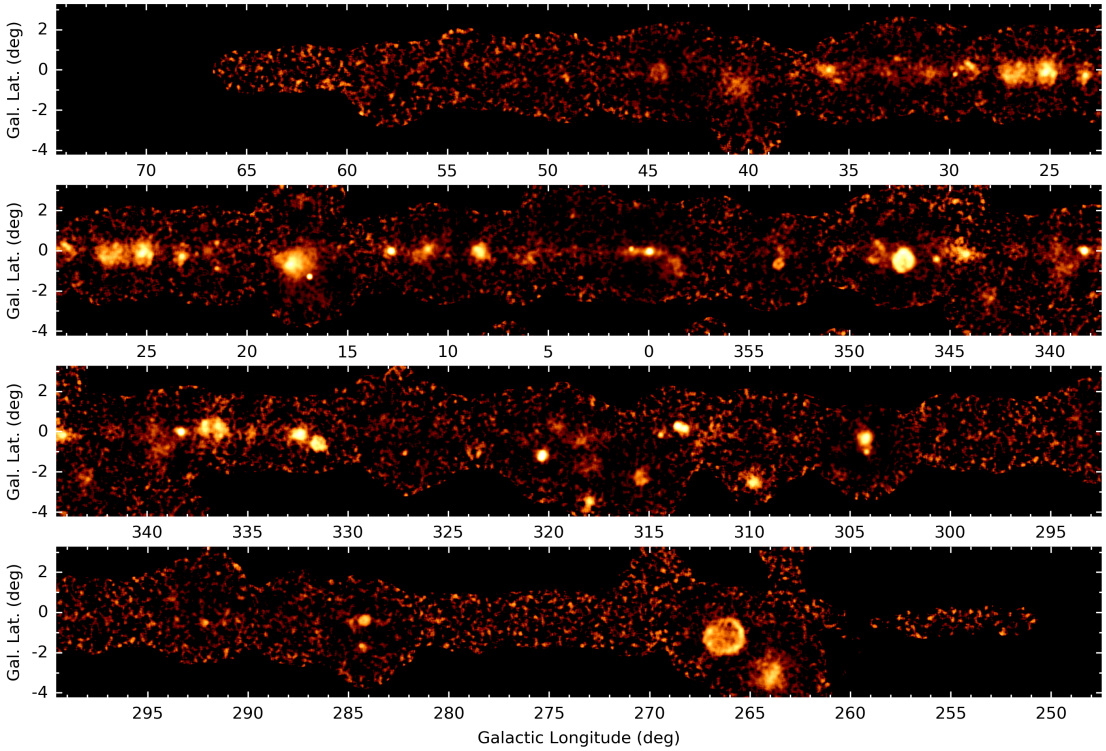

Figure 1.2: Overview of significance map from HESS Galactic Plane Survey in TeV gamma-rays (H.E.S.S. Collaboration, 2018b).

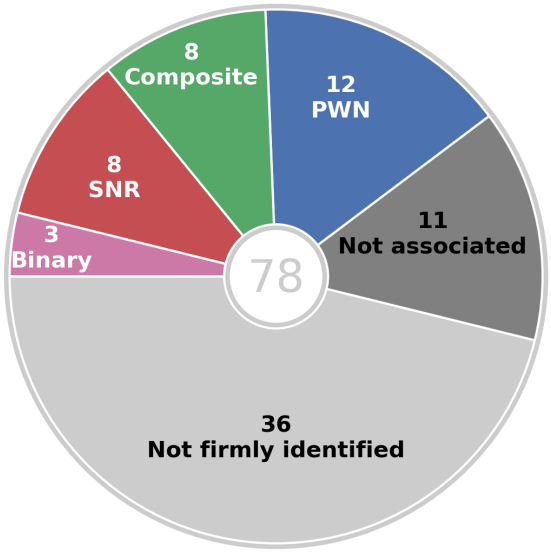

Figure 1.3: Summary of gamma-ray sources discovered by HESS in each class (H.E.S.S. Collaboration, 2018b).

Source name	Identified object	Class	Evidence
HESS J0852−463	Vela Junior	SNR	Morphology
HESS J1442−624	RCW 86	SNR	Morphology
HESS J1534−571	G323.7−1.0	SNR	Morphology
HESS J1713−397	RX J1713.7−3946	SNR	Morphology
HESS J1718−374	G349.7+0.2	SNR	Position
HESS J1731−347	G353.6−0.7	SNR	Morphology
HESS J1801−233	W 28	SNR	Position
HESS J1911+090	W 49B	SNR	Position
HESS J1119−614	G292.2−0.5	Composite	Position
HESS J1640−465	G338.3−0.0	Composite	Position
HESS J1714−385	CTB 37A	Composite	Position
HESS J1813−178	G12.8−0.0	Composite	Position
HESS J1833−105	G21.5−0.9	Composite	Position
HESS J1834−087	W 41	Composite	Morphology
HESS J1846−029	G29.7−0.3	Composite	Position
HESS J1930+188	G54.1+0.3	Composite	Position

Table 1.1: Firmly-identified SNRs from the HGPS (H.E.S.S. Collaboration, 2018b).

Gamma-ray photons are formed in several processes (see appendix A.2) within regions that contain a high energy source or a shock wave providing a particle accelerator. The unidentified candidates clearly need more observation using different wavelengths together with further interpretation concerning their origin.

HESS J0852-463 (Vela Junior) is one of the SNRs that has optical [O III], [S II] and Hα emission discussed by (Maxted et al., 2018). Moreover, emission in optical Hα and [S II] with radio, infrared and X-ray has been shown for HESS J1801-233 (W 28) (Pannuti et al., 2017; Aharonian et al., 2008b). Also, an optical Hα and [S II] image for HESS J1442-624 (RCW 86), a type Ia supernova, was presented along with other infrared and X-ray data in Williams et al. (2011). These sources are a sample of some HESS sources with optical emission. As a result, the relation between the optical Hα survey and HESS candidates has been not studied in depth. This connection will be considered as a main motivation for this thesis.

1.2 Why Consider H-alpha?

The Southern Hα Sky Survey Atlas (SHASSA) is shown in Figure1.4 and mapped the sky with angular resolution of 0.8 arc-min (Gaustad et al., 2001). The Hα spectral line at wavelength 6563 Å, which spreads through the interstellar medium, is extremely important for determining the amount of ionised gas. Hα light is emitted when an electron transitions from the third to the second energy level of the hydrogen atom. The electron moves from the second to the third energy level in the opposite absorption processes. Narrow band surveys such as SHASSA and others provide us with intensity and velocity with a spectral resolution (0.026, 12 km^{-1}) for the Hα (Gaustad et al., 2001). This optical line helps us study the structure of the ionised ISM in the Milky Way.

This survey is available on-line [1], and it contains 2168 Flexible Image Transport System (FITS) images covering the Galactic plane from $\delta < +15^{\circ}$ (Figure 1.4) (Gaustad et al., 2001). In addition, we use the Wisconsin Hα Mapper (WHAM) (Figure 1.5) survey , a northern sky survey with an angular resolution of 1°, considerably less than SHASSA.

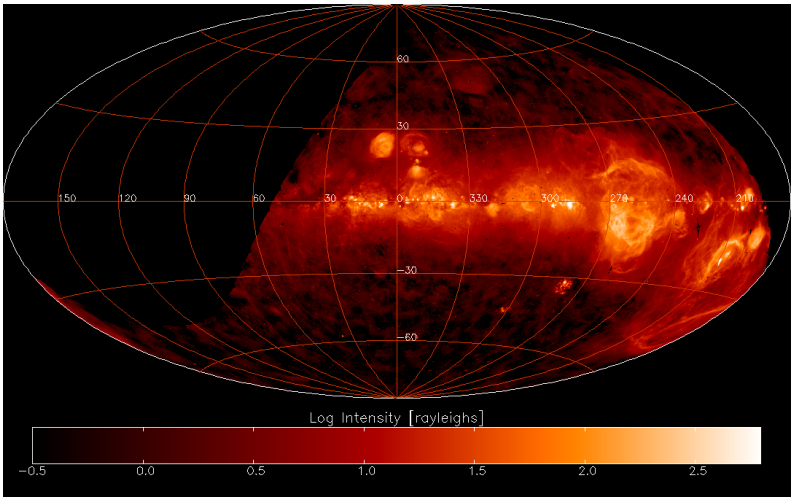

Figure 1.4: Hα sky map covered by the SHASSA survey (Gaustad et al., 2001).

[1] (http://amundsen.astro.swarthmore.edu/SHASSA/)

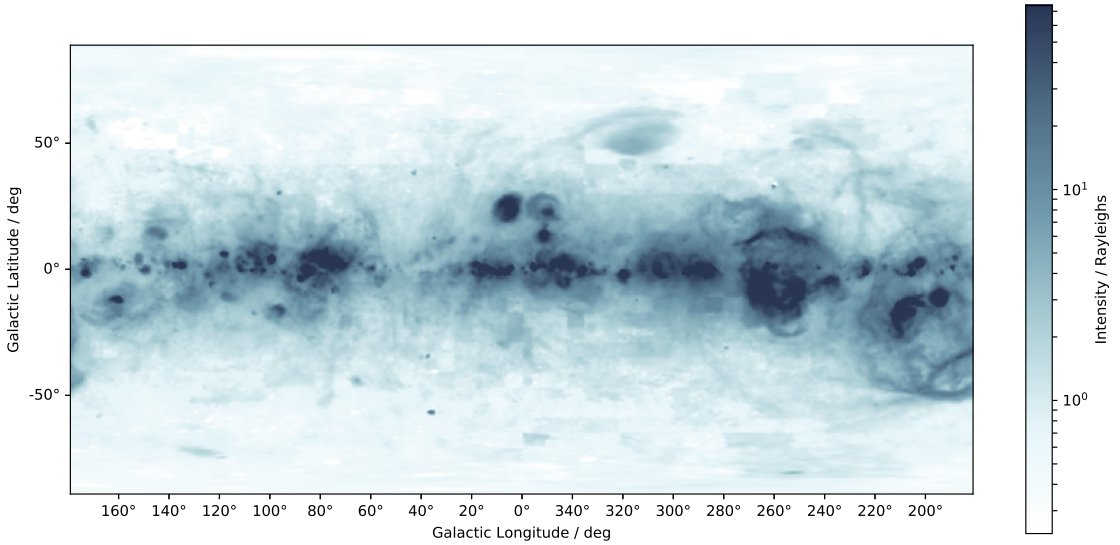

Figure 1.5: WHAM Hα covering the Galactic plane (Haffner et al., 2003).

The optical observation for the Hα line has another potential use in explaining the gas in the Universe. Details about the warm ionised medium (WIM) in the galactic plane is given in (Haffner et al., 2003). The WIM are regions that have a low density which can be found around H II regions or in some cases hot stars or pulsars (Hill et al., 2012). These surveys will determine the structure of the ionised gas in the galactic plane.

1.3 Examples of SNRs Seen in H-alpha and other wavelengths

SNRs are detected via optical observations, along with radio, X-ray, and gamma-ray observations. SNR coordinates and observations wave band are presented by (Green, 2019). In many cases, SNRs can be observed in multiple bands such as CTA 1 which is observed in optical, radio, X-ray, and gamma-rays as described by (Halpern et al., 2004; H.E.S.S. Collaboration, 2018c). Analysis of optical bands has revealed many SNRs with different morphologies. Some example of SNRs studied at an optical wavelength are discussed below.

Roberts et al. (2001) presents the ASCA catalogue of 30 sources in the 2-10 keV X-ray band. The number of SNRs discovered in the Galactic plane is approximately two hundred and eighty (Green, 2019). However, this number does not account for all SNRs since the study of SN explosions and pulsar birth rates plus an average SNR lifetime of a 10^5 years, implies around one thousand SNRs in our galaxy (Frew et al., 2018). This shows that only around one third of SNRs have been discovered, which makes searching for SNR counterparts to HESS sources a potential goal.

Stupar and Q. Parker (2011) propose that around 20% of these objects were discovered by the ratios in visible light spectrum. Fesen et al. (1985) were the first to detect SNRs via optical line ratios. As a result, the intensity in Hα sky map can be used to identify SNRs.

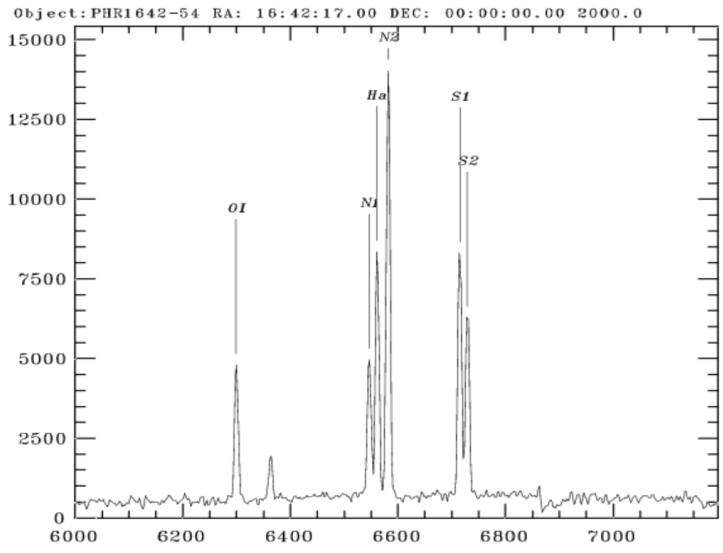

Figure 1.6: Spectrum for the red zone 5800–7300 Å G332.5-5.6 showing the emission lines (Parker et al., 2004).

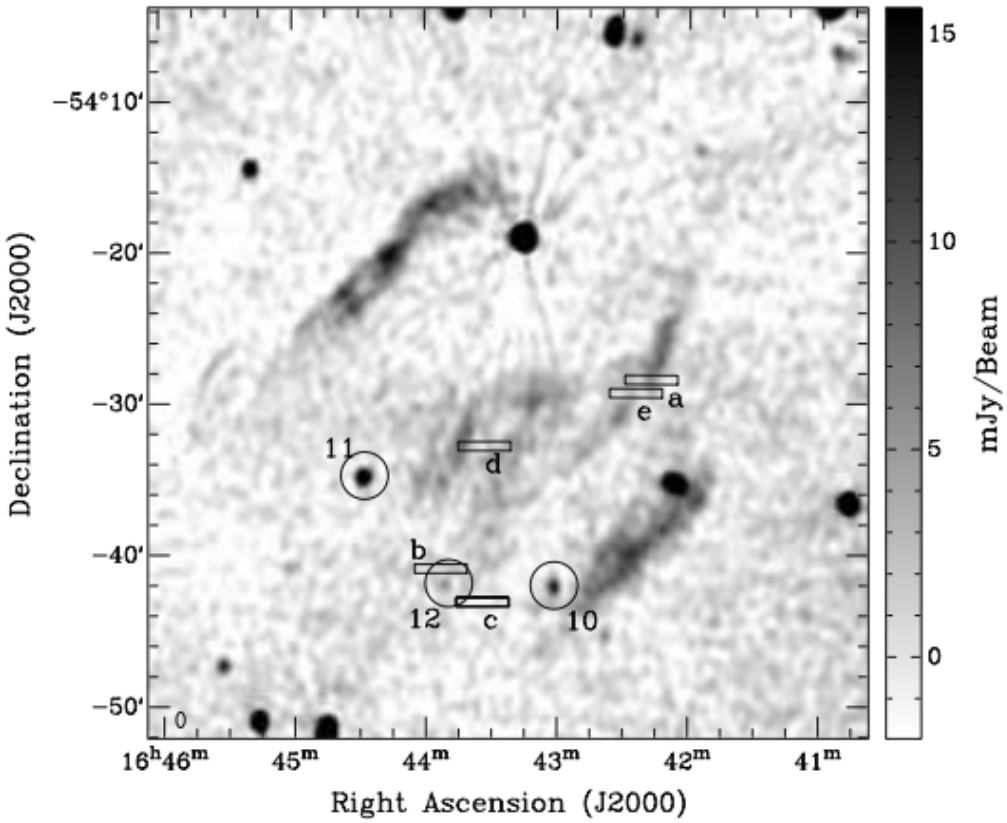

Figure 1.7: 843 MHz image for SNR G332.5-5.6. for the region a, b and c the ratio of $[S\,II]/H\alpha$ is 1.8, 2.32 and 1.84, respectively. In addition, there are three circles for radio sources (Stupar et al., 2007a).

Moreover, we know that all SNRs emit at most electromagnetic wavelengths. In this study, we are interested in gamma-ray and optical emission, and how they can be connected. In 2007, a study was conducted using optical line ratios for the detection of SNRs (Stupar et al., 2007b). They showed that the line ratio $[S\,II]/H\alpha \geqslant 0.5$ is an indication of an SNR shock. If this ratio is less than 0.5, a planetary nebula or H II region is more likely the favoured interpretation (Stupar et al., 2008).

Parker et al. (2004) found an optical line detection leading to a newly identified SNR (G332.5-5.6) using a combination of optical lines. The spectrum of G332.5-5.6 is shown in Figure 1.6 with clear Hα emission line at 6563 Å. Figure 1.8 shows the

intensity of lines in the G332.5-5.6 region and values of the lines ratios. The [S II] line at ∼6730 Å is also strong, and it indicates a high ionisation shock. In addition, we can see the [O I] line at 6300 Å with high intensity.

λ (Å)	Flux (Hβ=1.0)		λ (Å)	Flux (Hβ=1.0)	
3727	[OII]	9.25	6300	[OI]	1.40
4101	Hδ	0.46:	6364	[OI]	0.48
4340	Hγ	0.45:	6548	[NII]	2.16
4861	Hβ	1.00	6563	Hα	3.81
4959	[OIII]	0.49	6584	[NII]	6.40
5007	[OIII]	1.30	6717	[SII]	3.80
5199	[NII]	0.58	6731	[SII]	3.14
5755	[NII]	0.09:	7135	[AIII]	0.14:
5876	HeI	0.23:	7325	[OII]	0.51:

6717/6731 = 1.21; [NII]/Hα = 2.25; [SII]/Hα = 1.82
Hβ flux = 1.86x10^{-14} ergs cm^{-2} s^{-1}

Figure 1.8: Line fluxes for G332.5-5.6 comparing Hβ with the $[S\ II]/H\alpha$ and $[N\ II]/H\alpha$ ratios (Parker et al., 2004).

Stupar et al. (2007a) found further evidence to improve the identification of the SNR G332.5-5.6, which is at a distance ∼3-4 kpc and a diameter of ∼ 30 pc. In addition, for this object, they took five spectral observations of different regions. The SNR shell structure observed in the region by radio at 843 MHz, and the spectroscopy slits position are shown in Figure 1.7 (Stupar et al., 2007a) and the position of optical arcs for SNR G332.5-5.6 is shown using optical data from the AAO/UKST observatory. Stupar et al. (2007c) found another SNR in the Galactic plane via the same method. The value of the [S II]/ Hα ratio for SNR G315.1+2.7 arcs was found to be 1.13. In addition, other optical lines for the shock wave were observed. Radio observations were used to reveal the shell of the SNR G315.1+2.7 (Stupar et al., 2007c). An Hα image of the white arcs (Figure 1.9) shows the filament which has been discussed by Stupar et al. (2007c). The result of this work reinforces the study of the SNR in the optical band.

The SNR studies in optical bands needs to be augmented by studies in other electromagnetic bands such as radio, X-ray or gamma-ray. Table 1.2 shows each optical SNR considered by Stupar et al. (2007b) associated with multiple energy bands. Also,

RCW 59 (G293.0+4.5) which is a H II region, shows a ratio similar to SNR shock and there is a high possibility of mixture morphology. Some of these SNRs are already linked to existing high energy candidates, however, other SNRs are still under investigation.

The number of SNRs tends to increase with higher resolution observations at optical and radio wavelengths. Stupar et al. (2008) provides a catalogue of SNRs discovered using optical line ratios. The initial origin of these SNRs is ambiguous, and it is essential to further investigate these examples. Stupar et al. (2008) matched optical observations with radio observations and found that 11 of the candidates had clear radio counterparts. Eighteen SNRs have been confirmed and identified, and they are listed with their optical lines ratios in Table 1.2. In addition, they showed that [S II] provides a good indication of the age of an SNR.

Standard ID	Extent (')	[N II]/Hα	[S II]/Hα	[S II] 6717 Å /6731 Å	Radio	X-ray	Pulsar
G253.0+2.6	6	1.07	1.16	1.11	Y*	N	N
G243.9+9.8	16	0.65	0.89	1.55	Y	N	N
G283.7-3.8	120	1.38	1.47	1.33	N	Y	N
G288.7-6.3	2.5	0.46	0.54	0.93	Y	Y*	N
G281.9+8.7	150	1.39	3.59	1.40	N	Y	N
G288.3+4.8	"5 , 15 "	0.62	1.46	1.37	N	Y	N
G289.7+5.1	"7 , 15 , 22 "	0.60	1.38	1.40	Y	Y	N
G289.2+7.1	30	0.71	1.80	1.29	N	Y*	N
G292.9+4.4	100	0.65	0.97	1.40	Y	Y*	N
G303.6+5.3	240	0.58	0.74	1.42	N	Y	Y
G306.7+0.5	25	0.55	0.85	1.36	Y*	Y	Y
G315.1+2.7[2]	11	1.42	1.13	1.41	Y	Y*	N
G332.4+0.6	30	1.12	1.02	1.20	N	N	Y*
G343.4+3.6	"4, 7 "	0.81	0.59	1.35	Y	N	N
G332.5-5.6[3]	30	2.42	1.92	1.23	Y	Y	N
G329.9-7.8	7	1.77	1.18	1.27	N	N	N
G348.2-1.8	"5 , 8 "	0.94	0.82	1.42	Y	N	N
G18.7-2.2	30(120*)	0.72	1.33	1.34	Y*	N*	N*

Table 1.2: The SNRs with their optical line ratios from (Stupar et al., 2008), and their radio and X-ray emission states. (*) Indicates an uncertain detection.

Following this survey, optical line observation for the SNR G279.0+1.1 by Stupar and Parker (2009) showed that the [S II]/ Hα ratio was between 0.7 and 1.1, giving a reasonable indication for the SNR shell and the presence of [O II], Hβ and [O III]. The contours of the radio emission slightly overlapped the interesting Hα arcs.

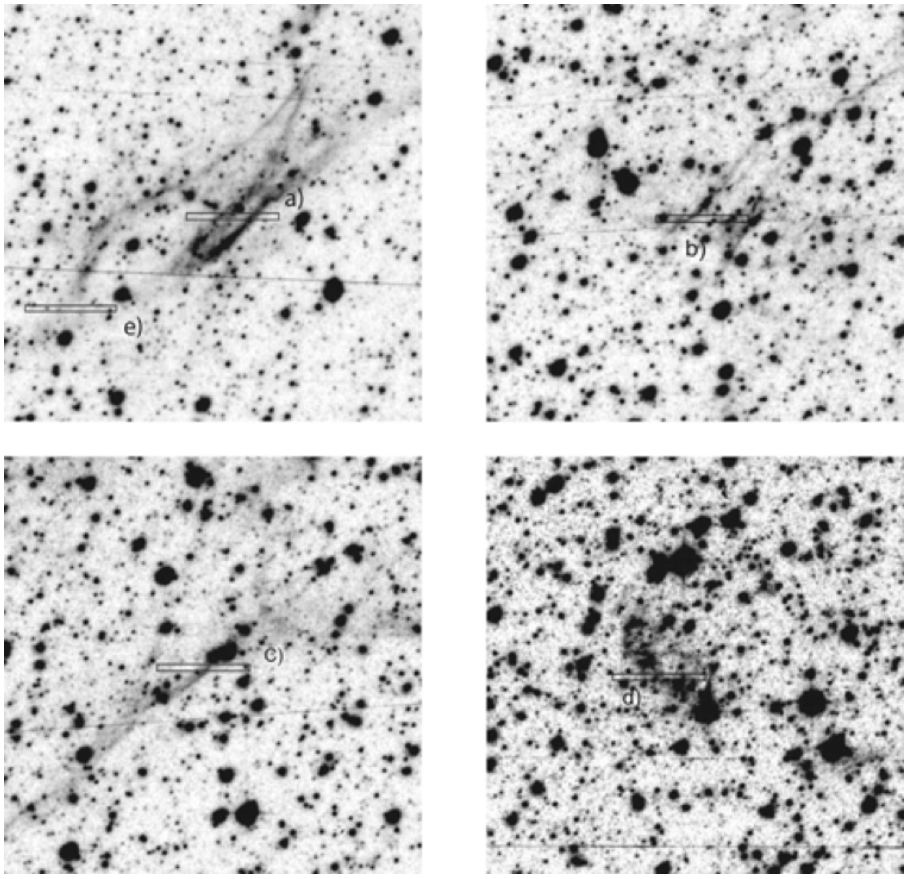

Figure 1.9: Hα image for G315.1+2.7 the blacks arcs show the shocks of SNR the spectrum where taken at the black rectangles (Stupar et al., 2007c).

Furthermore, M. Stupar et al. (2011) discussed the Wolf-Rayet stellar ejecta of WR 60 and found that the arc at that region is misidentified, suggest that the Hα shell in the direction of WR 60 star is in fact SNR shell. The SNR G310.5+0.8 ratio of [S II]/ Hα gives a value of 0.53, which is high enough to suggest an SNR origin. Figure 1.10 is an Hα image from the SuperCOSMOS H-alpha Survey (SHS) and Figure 1.11 shows the optical spectrum.

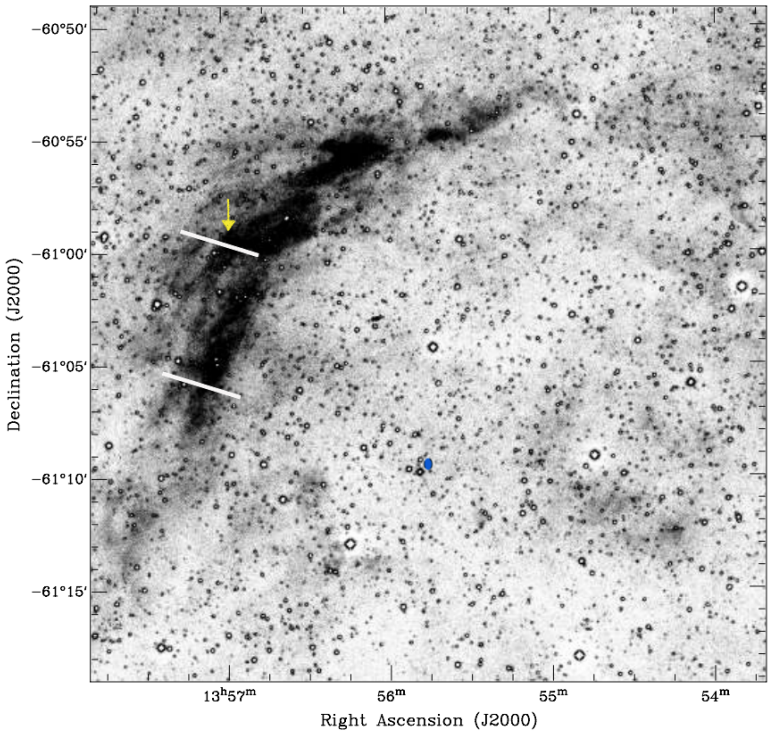

Figure 1.10: Hα image toward G310.5+0.8 and the spectrum slit position shown in white. The yellow arrow points at the location of optical spectrum slit (M. Stupar et al., 2011). The blue dot is the location of the WR 60.

Further, there are optical detections for SNR G213.0-0.6 with a [S II]/Hα ratio of between 0.5 and 1.1 depending on the filament region Milorad Stupar and Q. A. Parker (2012). Most recently, Ren et al. (2018) conducted studies of S 147 (SNR G180.0-01.7) using the Large sky Area Multi-Object Fiber Spectroscopic Telescope (LAMOST). From the spectral line of the SNR, the radial velocity and line ratios, they confirm older studies. They found that the [S II]/Hα ratio is 0.77, and the speed of the filament varied from 100 to -100 km s^{-1}.

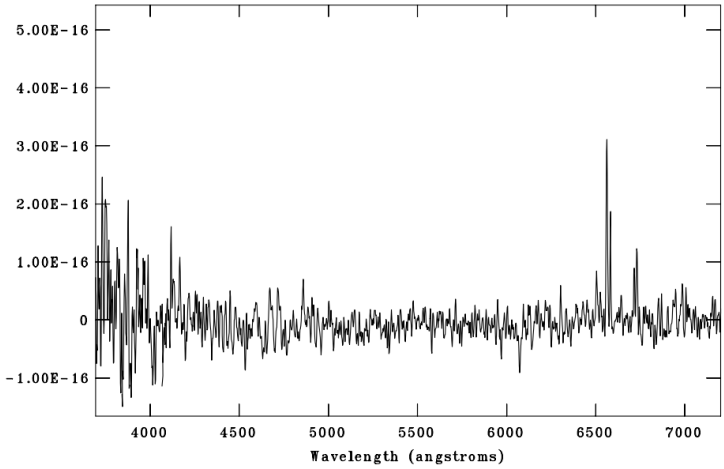

Figure 1.11: Slit spectrum from the northern white line in figure 1.10 (M. Stupar et al., 2011).

This optical detection ratio method is not only used for Galactic objects, but also to reveal SNR from other galaxies. Blair and Long (2004) studied M83, (NGC5236) a spiral galaxy at a distance of 3.75 Mpc, and they found 71 SNRs in this galaxy using optical lines. Primarily, their study used the [S II]/ H$\alpha > 0.4$ criterion to identify the SNRs. Figure 1.12 shows an Hα image of M83 including the identified SNR.

There are many undefined sources in the HESS TeV survey, and it will be useful to use this method to estimate the origin of the gamma-rays. The Hα surveys can be used as a tool to predict association of SNR filaments generated by the same initial source with the gamma-rays at the same field of view. As a result, the knowledge of the original source will help to clarify the age and the ISM structure around the regions. The age and the distance to the gamma-ray source will play an essential role in the prediction. Moreover, this can be helpful as the information for predicting and estimating SNR model can help find the filaments or arcs in optical light provided by the possible source for the TeV gamma-ray.

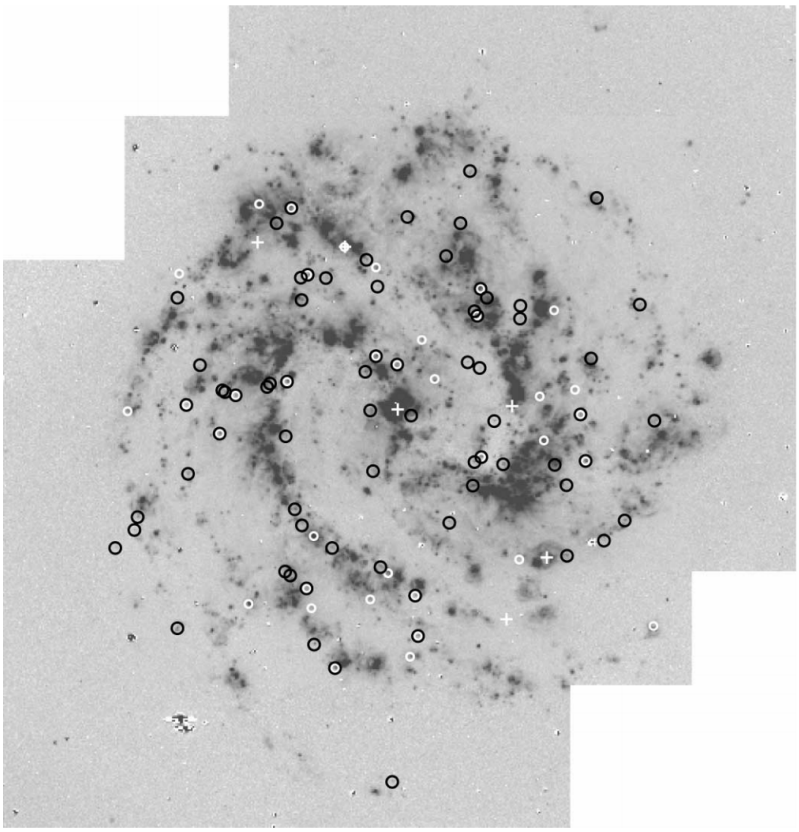

Figure 1.12: Continuum-subtracted Hα for M83 with black circles indicating the SNR and white circles indicating the nebulae with strong [O III] emission (Blair and Long, 2004).

We adopt this method to reveal and explore the sources in the HESS survey. The relation between SNRs and gamma-rays observation is through the progenitor supernova. In this project, we test the assumption that the gamma-ray and the Hα are connected by an SNR. Here we present a prominent example of the PWN HESS J1825-137 which has been discussed by Duvidovich et al. (2019), H.E.S.S. Collaboration (2019), Voisin et al. (2016), and Aharonian et al. (2006a) in multiple wavebands.

1.3.1 HESS J1825-137 and its Optical Supernova Remnant Counterpart

As one of the most luminous sources in HESS, HESS J1825-137 is one of the brightest PWNe. The pulsar that powers this source is believed to be PSR J1826-1334, a high energy pulsar with spin-down power $\dot{E} = 2.8 \times 10^{36}$ erg s^{-1} at a distance of 4 kpc and age of $\tau \sim 20$ kyr. HESS J1825-137 is one of the TeV sources that is classified as PWN (H.E.S.S. Collaboration, 2018b).

The SNR regions of the initial SN were not discussed until 2016 (Voisin et al., 2016). Using a potential method to investigate the possible relations of both bands can help to find new SNR candidates (Stupar et al., 2008). The optical SNR shell for HESS J1825-137 is clearly presented Figure 1.13.

As shown in Figure 1.13, This region has more than one TeV gamma source. There is HESS J1825-137, HESS J1826-130 and HESS J1826-148. In addition to HESS J1825-137, HESS J1826-130 to the north is still unidentified. The nearby PSR J1826-1256 with $\tau \sim 13$ kyr, $\dot{E} = 3.6 \times 10^{36}$ erg s^{-1} and period P=100 ms powering X-ray PWN G18.5-04 may be also related (Voisin et al., 2016). Also, in this region to the south there is the microquasar (LS 5039) HESS J1826-148 which has point like TeV emission morphology (H.E.S.S. Collaboration, 2018b).

The gamma-ray spectrum of the source together with observations have indicated that PSR J1826-1334 is the energetic source for the region (Aharonian et al., 2006a). HESS J1825-137 and other TeV source sources shown in Figure 1.13 are complex regions that contain many H II regions and SNRs. Voisin et al. (2016) studied these sources via millimetre-wave radio and Hα observations and through mapping the surrounding ISM to understand this region. In addition, they show the relation of the optical SNR discovered on the left side of the source.

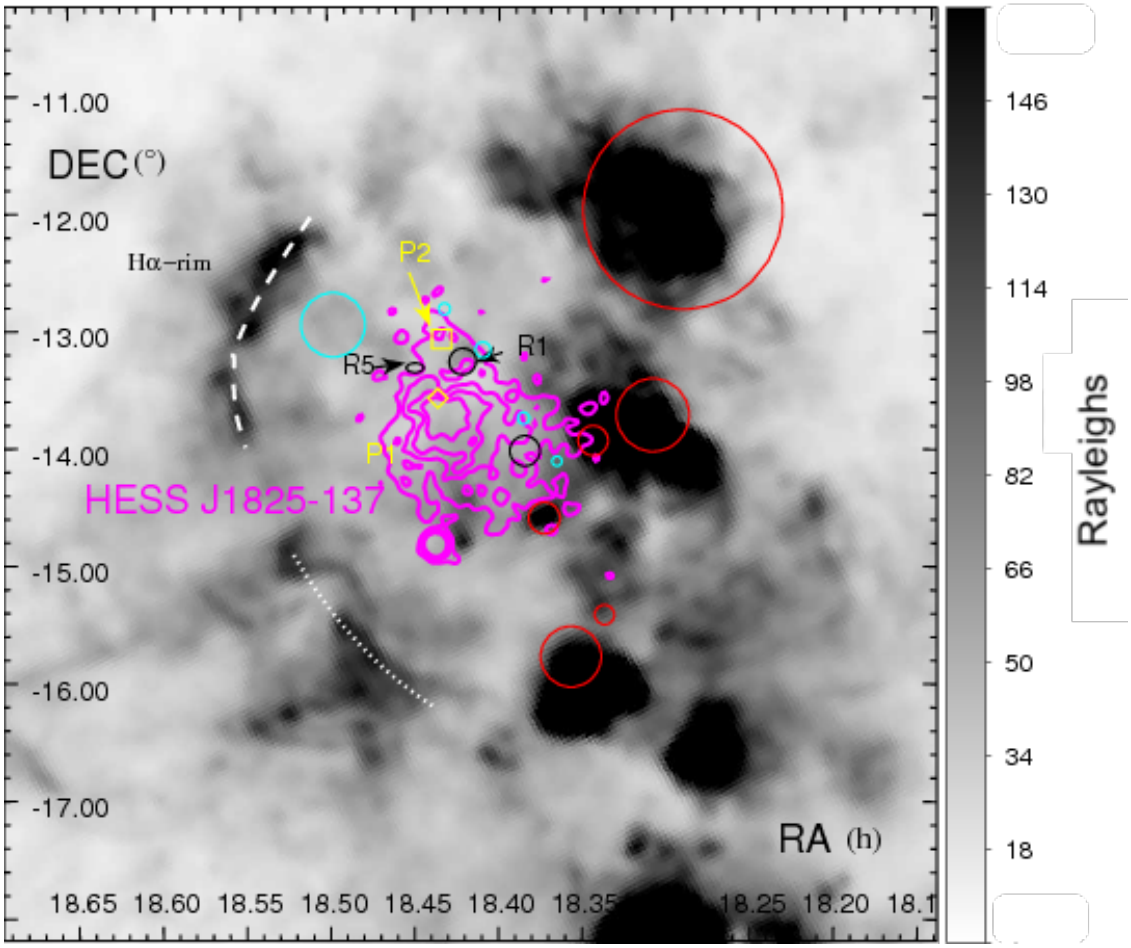

Figure 1.13: Optical Hα image From Voisin et al. (2016), pulsars are in yellow PSR J1826-1334 (P1) and PSR J1826-1256 (P2), and the region of HESS J1825-137 and its TeV emission is the contours in magenta. The radio sub millimeter observations is noted in black region. The SNR arcs are dashed white lines. The SNRs in this region is in cyan circles and the red circles are H II regions (Voisin et al., 2016).

However, HESS J1825-137 is surrounded by many H II regions in which there are 3 extended regions to the north those shown in red circles of Figure 1.13. The optical arc in Hα were announced by Voisin et al. (2016) and the link of this Hα optical arc which known as SNR related to the HESS J1825-137. This is considered as the first link between optical SNR arc and TeV gamma-ray source by HESS.

More than half of the HESS sources are PWN or unidentified candidates, providing an opportunity to investigate optical Hα around HESS sources which makes a large space

for investigating optical Hα around HESS candidates. This thesis aims to investigate the optical Hα and TeV HESS observations, and to look for possible connections between them, such as HESS J1825-137.

2 Gamma-ray and H-alpha Production in Supernova Remnants and Supernova Remnant Evolution

Understanding the mechanisms and models explaining the evolution of supernova remnants is critical to relate both the optical and gamma-ray energy bands. Models that describe the evolution of supernova remnant have been established for several decades. In this Chapter, we will outline the production of gamma-rays, Hα from SNRs , and how SNRs will evolve with time.

2.1 The Evolution of SNRs

Supernova remnants (SNRs) are the result of supernova explosions which eject a mass M_{ej} with a high-velocity v_s and energy E_{SN}. The shock velocity (v_s) will decrease over time due to the swept-up ISM mass. The estimate of the ISM mass depends on its density ρ (Reynolds, 2008).

The free expansion phase is during the first 10^{2-3} yr, which will heat, compress and accelerate the ambient medium. As a result, two different shocks are formed: the forward shock and the reverse shock. These interaction shocks decelerate over time the speed of the SNR shocks and increase the temperature of the shock medium. In this phase, the ISM pressure is negligible due to the supersonic velocity of the shock wave. The shock velocity v_s can be estimated by assuming that the supernova energy,

E_{SN}, will be transferred into kinetic energy (Reynolds, 2008).

$$v_s = \left(\frac{2E_{SN}}{M_{ej}}\right)^{0.5} \tag{2.1}$$

where M_{ej} is the ejected mass. The shock radius R_s at time t can be found using:

$$R_s(t) = v_s t. \tag{2.2}$$

The SNR shock moves through the ISM and compresses it, meaning that the interstellar and stellar material are separated by a contact discontinuity, which is a surface between interstellar and stellar where both have similar pressure and velocity but different densities. Also,the reverse shock will start to move towards the centre of the SN with respect to the ejected material. The accumulated material from the ISM starts to affect the expansion by compressing the region between the contact discontinuity and the forward shock. The radius of the SNR R_{SW} at the end of this so-called swept-up phase that was created by interstellar material swept up by the free expansion shock is given by;

$$R_{SW}^3 = \frac{3M_{ej}}{4\pi\rho_o}, \tag{2.3}$$

where ρ_o is the initial density of the ISM. During the free expansion phase, the SNR shock structure starts to deviate from spherical geometry due to the reverse shock wave that travels inward and further heats the stellar material. The pressure then stabilizes and the next phase of the SNR begins is the Sedov-Taylor phase where the thermal pressure of the gas drives the expansion.

In the Sedov-Taylor phase (around 10^4 yr), the material in the SNR is at high temperature, approximately 10^6 K and the energy losses by thermal radiation are small, which means the gas will be cooled by adiabatic expansion. Thus, the solution for the free expansion phase is not valid. In the Sedov-Taylor phase, we use the self-

similar solution for a pressure-driven explosion and assume a small geometrical shell ($\triangle R/R \ll 1$) and a mass which is similar to the swept-up mass and as a result the pressure P will be relevant. These assumptions, along with the relationship $v_s \propto t^{3/5} \propto {R_s}^{-3/2}$ by Sedov (1959) and Taylor (1950) and using the first law of thermodynamics, which describes the change of the internal energy, can be applied to the equation of motion (EoM) giving;

$$\frac{d}{dt}\left(\frac{4\pi}{3}R_s^3\,\rho_o\dot{R}_s\right) = 4\pi R_s^2 P\,. \tag{2.4}$$

Here, we have the mass of shell $\left(\frac{4\pi}{3}R_s^3\,\rho_o\,\right)$ at radius R_s and $\dot{R}_s$ is the rate of change of the radius in the radius of the shell. Assuming V is the volume and $PV = (\gamma-1)E$ for $\gamma = 5/3$ we can find:

$$R_s = 1.54\times10^{19}\text{cm}\,(E_{51}^{1/5}/n_0^{1/5})\left(\frac{t}{10^3\text{yr}}\right)^{2/5} \tag{2.5}$$

$$v_s = 1950\,E_{51}^{1/5}n_o^{-1/5}\left(\frac{10^3\text{yr}}{t}\right)^{3/5}\ \text{km}\ s^{-1} \tag{2.6}$$

$$T_s = 5.25\times10^7\,E_{51}^{2/5}n_o^{-1/5}\ \text{K}\ , \tag{2.7}$$

where R_s is the shock radius, v_s is the velocity, T_s is the temperature of the shock and n_0 is the ISM density. At this stage, one third of the energy is released as radiation (Sedov, 1959; Taylor, 1950).

The last phase is the radiative phase where the SNR cools and expands adiabatically until a critical temperature of 10^6 K. Below this temperature the ionised atoms start to capture free electrons e^- and lose energy through radiation. The expansion rate in this phase falls because of the drop in the thermal pressure during the post shock. The SNR enters the snow plough phase and ISM accumulates until the swept up mass is greater than the ejected stellar mass. The shell breaks after this phase to form individual arcs and potential shells tht can be seen in various wavebands.

2.2 Gamma-rays

The production of gamma-rays require the interaction of high-energy particles with radiation or matter. The gamma-ray production is commonly classed as leptonic or hadronic based on the nature of the parent particles producing the gamma-ray. Leptonic origin gamma-rays result when electrons interact with low energy or soft photons and are scattered through the Inverse-Compton (IC) effect or interact with matter to produce IC radiation. Hadronic origin gamma-ray are due to protons accelerating to a state that results in losing most of their energy in an interaction with ISM matter.

The production of gamma-rays for the hadronic channel in SNRs is related to the cosmic-rays (CRs) accelerated by the SNR shock front. Dermer and Powale (2013) suggested that CRs that are accelerated by the shock interact with ISM matter and produce neutral pions π^o, which will decay to produce gamma-rays as shown in Figure 2.1. This is the main type of hadronic radiation involves the collision of a proton with a stationary atom to create a neutral pion.

Observing TeV gamma-rays reveals the presence of multi-TeV particle accelerators, usually thought to be either SNRs, pulsar wind nebulae, pulsars, jets from stellar black-holes, or from extragalactic sources such as Active Galactic Nuclei (ANG). However, identifying these different accelerators in our galaxy is challenging due to the complex structure of the interstellar medium. There are many TeV gamma-ray sources that still have an uncertain origin as discussed in chapter 1. Figure 1.3 shows that we have many undefined objects, leaving a gap in our understanding of the gamma-ray emission in Milky Way (H.E.S.S. Collaboration, 2018b).

The number of unidentified sources is related to the method of illustrating and explaining the origin or the production methods of the TeV objects. For example, HESS J1641-463 and HESS J1741-302 are still unidentified. In addition, HESS J1702-420 lies near PSR J1702-4128, is an asymmetric PWN to be associated by the observed

Very high energy gamma-rays. In addition, HESS J1804-216 is suggested to be associated with SNR G8.7-0.1 and molecular gas from CO observations, but the connection is not conclusive to the high observed energy (H.E.S.S. Collaboration, 2006). Frew et al. (2018) confirms a presence of an optical SNR around G6.31+0.54 which may be related to HESS J1801-233 or the well known SNR W 28.

The identification of the TeV gamma-ray sources depends on many factors. Firstly, in many scenarios high energy gamma-rays (> 10 TeV)are thought to be initiated by the hadronic scenario (Angüner et al., 2017). However, most of the TeV sources discussed here remain unidentified owing to their complex extended morphology. An exception is the point-like morphology of HESS J1741-302, suggesting a binary system by Angüner et al. (2017).

Yamazaki et al. (2006) used the X-ray and TeV gamma-ray flux ratio to indicate the evolution states of SNR:

$$\left[R_{TeV/X-ray} = \frac{F_{\gamma-ray}(1-10\ \mathrm{TeV})}{F_{X-ray}(2-1\ \mathrm{KeV})}\right] > 2\,, \tag{2.8}$$

where $F_{\gamma-ray}$, and F_{X-ray} are gamma-ray and X-ray fluxes. The result of their calculations of the SNR evolution shows that the flux ratio in (Table 2.1) can be different in each phase.

Yamazaki et al. (2006) made the assumption that the shock velocity depends on the SNR age and neglected the magnetic field on the dynamics of the SNR. They found that in the Sedov-Taylor phase, there is a noticeable increase in the flux with SNR age, and that the primary method for X-ray production is synchrotron emission. Here, Yamazaki et al. (2006) assumed production of TeV gamma-ray via the hadronic channel. The radiative phase is affected by the temperature of SNR shock, which cools over time, and hadronic TeV gamma-ray emission dominates the emission. If the SNR evolves close to a giant molecular cloud (GMC) the TeV emission from the hadronic channel can be significantly enhanced. Here, the GMC acts as a target for

SNR accelerated cosmic-rays (protons) to collide with (see Figure 2.1).

SNR phases and ISM	$R_{\text{TeV/X-ray}}{}^{a}$	$R_{\text{TeV/GeV}}{}^{b}$	$R_{\text{TeV/radio}}{}^{c}$
young SNR Sedov-Taylor phase	7.6×10^{-2}	0.36	9.8
old SNR Sedov-Taylor phase	1.6	0.25	6.6
old SNR radiative phase	82	6.6	47
SNR shock interact with GMC	6.9	74	9.7×10^{3}
GMC illuminated by SNR accelerated particles	5.9×10^{2}	5.8	3.5×10^{2}

Table 2.1: Flux ratios for different SNR evolution phases and ISM situation (Yamazaki et al., 2006).

[a] $R_{\text{TeV/X-ray}} = F_{\gamma}(1\text{–}10\ \text{TeV})/F_{X}(2\text{–}10\ \text{keV})$.
[b] $R_{\text{TeV/GeV}} = F_{\gamma}(1\text{–}10\ \text{TeV})/F_{\text{GeV}}(1\text{–}10\ \text{GeV})$.
[c] $R_{\text{TeV/radio}} = F_{\gamma}(1\text{–}10\ \text{TeV})/F_{\text{radio}}(10\ \text{MHz–}100\ \text{GHz})$.

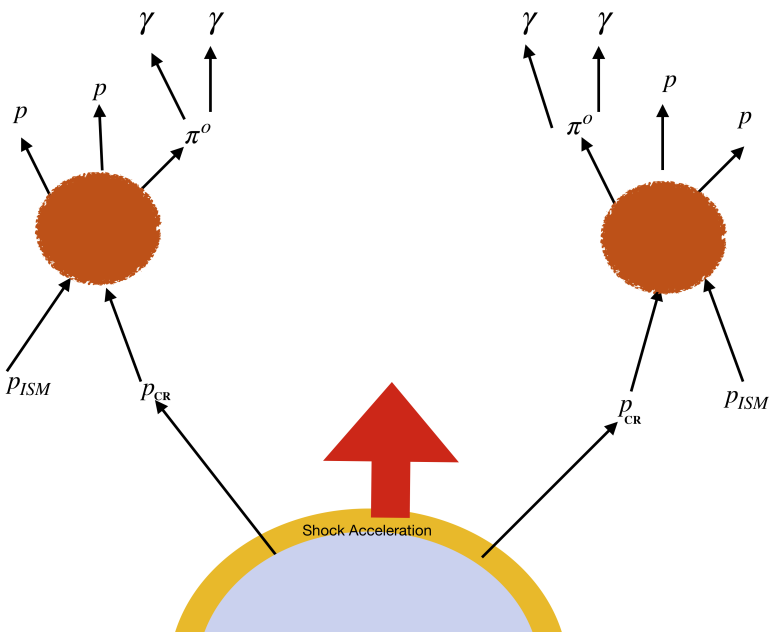

Figure 2.1: Production of gamma-rays from CRs accelerated by an SNR shock interaction with the surrounding ISM e.g a GMC.

The number of the TeV source candidates depends on the scenario that create such high energy sources. Yamazaki et al. (2006) presents the estimated number of 3×10^{3} TeV candidates from old SNR or giant molecular cloud interacting with SNR shocks.

Unidentified TeV sources are due to the complex ISM. For example, the probability that an old SNR or a giant molecular cloud interacte with SNR shocks and it leaves some of the SNR shock propagate and observed by HESS as unidentified.

2.2.1 Model of SNR Expansion

Predicting the SNR morphology is an important aspect in linking unidentified TeV sources to SNRs. Given that the SNR age is related to the surrounding ISM conditions, we can compare the TeV gamma-ray and Hα morphology to the expectation under an SNR hypothesis. The evolution of an SNR in the ISM is complex and non-trivial to estimate because of the contribution of gas density and temperature. We use a supernova remnant model that takes into consideration the density of the medium around the source, and the modelling will consider essential parameters that are already discussed such as age and initial mass. The prediction will consider the ages from the presented literature. The SNR age can be obtained from its radius r (pc) using the following equation (Dermer and Powale, 2013):

$$dt = \frac{dr}{v_0}\left(1 + \frac{4\pi\rho r^3}{3M_0}\right)^{1/2} \text{ yr}, \tag{2.9}$$

where dt is the SN age, dr is the change in radius, v_0 is the initial velocity, ρ is the density of the ISM which is assumed to be 1.6×10^{-28} kg cm^{-3} or a value suggested by literature, and M_0 is the initial mass of the progenitor star. It is possible to estimate the radius of the SNR shell and apply this to a search for optical arcs or related features in the Hα line. As this function requires an expected radius for the initial SN, using it as the predicted radius for the SNR will have an uncertainty range, according to the uncertainties in the age, distance, and/or density. With this method, we can predict the SNR radius that may form around TeV gamma-ray emission. Similarly, there is a radius range to indicate the location of filaments or arcs that might be seen in Hα. Figure 2.2 shows how the SNR radius changes with time and describes, the SNR radius

and its relationship to the initial mass for the progenitor star. A general prediction for this mass is used, assuming a mass of 10 ($M_{\odot}$) for SN type II (core-collapse), and 1.4 ($M_{\odot}$) for type Ia.

Equation 2.9 can also be used to determine the approximate ISM density by applying it to cases where there is an existing SNR shock related to a pulsar or TeV source, assuming we know the distance to the SNR. In Table 2.2 we illustrate the average ISM density in the Milky Way. Given that SNRs typically evolve into voids of density (especially type II), we will assume an initial values for the hot to warm and ionised gas of ~ 0.1 cm^{-3}. The change in the SNR radius can vary depending on the age of the SNR. We will assume an SNR age based on the age of any potentially associated pulsar (if known), or a typical mature age SNR as 10 kyr in the absence of any details evidence for an SNR.

Another method that will be used in our search for SNR components around HESS sources is the ratio of PWN radius (r_{pwn}) to SNR radius (r_{SNR}). Based on the numerical analysis of a spherically symmetric model, the SNR radius from a middle aged ($\sim$ 10 kyr) PWN, $r_{SNR} \sim 4\, r_{PWN}$ can be predicted (Van der Swaluw, 2001). We can therefore use PWNs as an additional constraint to look for evidence of optical SNRs in Hα. However, the short-comings of this method is when the reverse SNR shock from SNR constraint collides with the PWN for old SNR of age $\sim 10^5$yr.

2.2.2 ISM Density in Galactic Plane

The ISM density can vary considerably for different regions in the Milky Way. Ferrière (2001) summarised the different densities for different regions in the galactic plane which is shown in Table 2.2. The molecular clouds are cold, and as a result they tend to have more atoms which results in a contained expansion of the SNR. Atomic clouds are usually slightly warmer, and have fewer particles than molecular clouds. The warm atomic regions and the warm ionised regions have a similar ISM density. The

hot ionised gas has the lowest ISM density but the highest temperature. Thus, there is a differences in terms of each source region where the density plays an essential role in the radius of the SNR. For example, the case of HESS J8125-137 (Voisin et al., 2016) uses a density of 0.003 cm^3 based on CO(1-0) measurements and the type II SNR that produced the associated PWN.

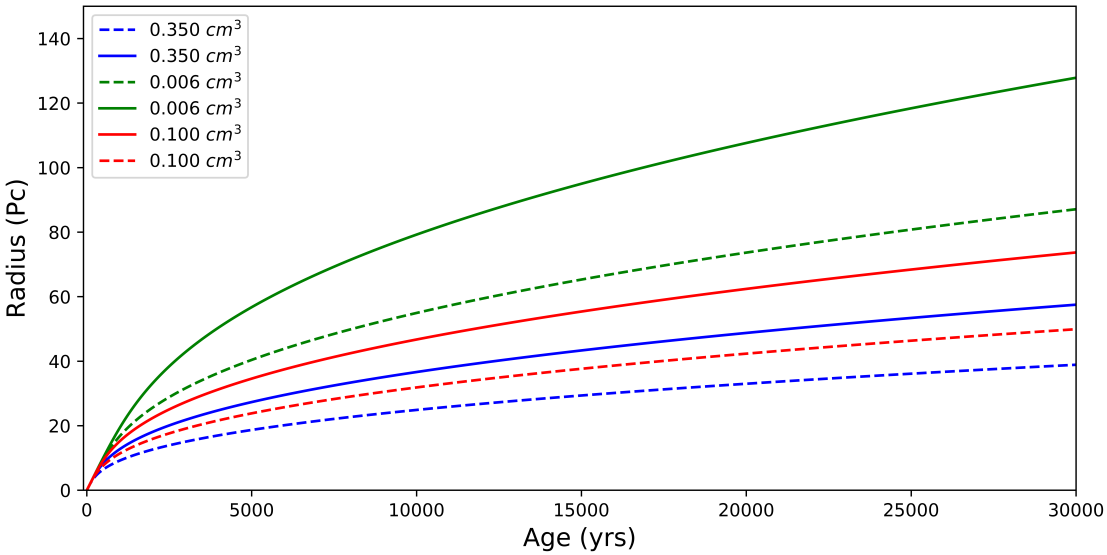

Figure 2.2: SNR radius vs time from Equation 2.9. The radius is shown for various ISM densities, where the solid lines are for core collapse type II supernova and the dashed lines represent type Ia supernova.

Component	T (K)	n (cm^{-3})
Molecular	$10 - 20$	$10^2 - 10^6$
Cold atomic	$50 - 100$	$20 - 50$
Warm atomic	$6000 - 10000$	$0.2 - 0.5$
Warm ionised	~ 8000	$0.2 - 0.5$
Hot ionised	$\sim 10^6$	$< 10^{-2}$

Table 2.2: Descriptive parameters of the different components of the interstellar gas. T is the temperature and n is the number density of hydrogen atoms or nuclei (Ferrière, 2001).

Thus, to estimate the radius of each SNR model we will use an approximate value

for the ISM density. In the case of PWNe, the age of the powering pulsar from the literature has been used. However, this age can also affect the modelled radius of the SNR. Figure 2.2 highlights the evolution of the SNR radius versus time for different ISM densities. A lower ISM density will allow the SNR radius to expand further and vice versa for high ISM density. In summary, we have two approaches to calculate the ISM number density. First, we can assume an average initial ISM number density in the galactic plane of n=0.1 cm^{-3} as suggested by Dermer and Powale (2013), or we can vary the number density in our calculations based on literature and Table 2.2.

2.2.3 Stellar Wind Bubbles

Another potentially interesting feature that may appear in Hα is related to the stellar wind bubble. Following the formation from a dense molecular cloud, progenitor stars start to produce powerful stellar winds which have velocities of the order 1000 km s^{-1}. This wind interacts with the ISM or the clouds around it and inject energy to the surrounding medium. Using the pulsar location as the progenitor-star, the stellar wind bubble (SWB) and the surrounding cavity (a result from the stellar wind interacting with the ISM and a thin shock layer in the surrounding environment) can be calculated to look for a further possible sign, of a type II SN in the Hα emission. There are different models for predicting SWB radius commonly used in the literature. In this study, a stellar wind bubble model with a radiative forward shock was chosen to estimate the shell radius of the initial star. In our SWB model, we have assumed massive stars, i.e. with spectral types O9-O2. Weaver et al. (1977) presented a model for predicting the radius of the SWB shock wave (R_{SWB}) around a star with ISM density n$_0$=0.1 cm^3, as follows:

$$R_{SWB} = 27 \left[\frac{L_{36}}{n_0} \right]^{1/5} (t_6)^{3/5} \text{ cm} , \tag{2.10}$$

where t is the age of the star divided by 10^6 yr, $L_{36} \equiv L_w/10^{36}$ erg s^{-1}, and L_w is the

wind luminosity in units of erg/s, which can be found as follows:

$$L_w = 0.5\dot{M}{v_w}^2, \tag{2.11}$$

where $\dot{M}$ is the mass loss rate from the initial star, and v_w is the velocity of the wind. However, it should be noted that this equation neglects the bow shock of the radiation pressure which will not affect the SWB model radius with a huge factor.

2.3 Production of Optical Emission in SNRs

Radio observations have been used to detect most SNRs (Green, 2019). X-rays are very sensitive to PWNe and SNRs similar to radio (see Prinz and W. Becker (2014)). Optical line detection of SNRs is now the fruitful method to detect SNRs. There are many SNRs that can be detected by visible light. Here, we will present methods for detecting SNRs using optical lines.

2.3.1 Optical Line Ratios

The presence of emission lines in the ISM depends on the excited state of the atoms, often located around a shock. Ratios of various spectral lines can be used to estimate the temperature, abundance, electron density, and the shock velocity. Optical ratios show the physical condition of the ionized gas in the ISM which will vary in SNRs, planetary nebulae (PNe), and H II regions. The characteristics of old SNRs ($> 10^3$ yr) in the band of 3500-7500 Å are strong emissions from H, [O III], [O II], [S II], and [N II], and fainter emissions from [He I], [He II], [Ne III], [N I], [O I], [Fe II], [Fe III], [Ca II], and [Ar III] (Fesen et al., 1985). On the other hand, young SNRs ($< 10^3$ yr) enhanced by their ejected material show an abundance of the ambient ISM with an amount of small interference from the interstellar dust grains. The electron densities can be calculated from the intensity I ratios:

$$R = I(^2D_{3/2} \rightarrow^4 S)/I(^2D_{5/2} \rightarrow^4 S), \tag{2.12}$$

where the ratio R is between two electron transitions, namely from the atomic states $^2D_{3/2}$ to ^4S and $^2D_{5/2}$ to ^4S.

The essential lines are as follows: the [O II] at 3726-29 Å, [S II] at 6731-17 Å, [Cl III] at 5538-18 Å, [Ar IV]at 4740-11 Å and [K V] at 4163-23 Å (Saraph and Seaton, 1970). The line [O III] 4363-4959-5007 Å indicates the temperature of the ISM is important. The ratio between [O III] 5007 Å and [O III] 4959 Å is fixed to the value 3 due to both lines being emitted by a transition from the same electron energy state. Since both of these lines are from same upper atomic level, the intensity of the line 4363 Å rises as the temperature increases, and therefore the temperature can be found via the ratio $I(4959 + 5007)/I(4363)$ (Osterbrock, 1989). When the temperature and density are known, the abundances of the medium can be calculated.

The shock velocity can be found by the ratio of Hα to Hβ, which decreases at high shock speed. In addition, the intensity of He I 4686 Å is stronger relative to Hβ for shock speeds between 80-120 km s^{-1}, and the [O III] line reaches its highest intensity at a velocity of 80 km s^{-1}. In slower shocks, i.e. < 100 km s^{-1}, [O II] 3727 Å is strong because at the maximum temperature, most emission is from O II.

Fesen et al. (1985) present a line ratio that can be used to identify SNRs. This ratio [SII]/Hα exploits the photo ionization shock coming from the SNR. If this ratio is less than 0.5, the observed region is likely a planetary nebulae or H II region (Stupar et al., 2008). Fesen et al. (1985) found additional ratios $([OI]/H\beta)$ and $([OII]/H\beta)$, to support claims that the observed filament might be an SNR shell or arc (Stupar et al., 2008). There are other optical lines that support classification of the SNRs, such as [O II], [O III], [N II] and $H\beta$ with wavelengths of $3727,\ [4959,\ 5007][6548,\ 6584]$ and 4861 Å respectively (Stupar and Parker, 2009). These ratios are consistent with those found by Dopita et al. (1984). In this thesis we will rely mostly on the work of (Stupar

et al., 2008) who used the ratio of $[SII]/H\alpha > 0.5$ and Hα images.

2.3.2 H-alpha Observation

In the optical part of the spectrum, there are many recombination lines such as [S II], Hα, [O III], Hβ, and [O II]. For the production for each of these recombination lines there are physical constraints imposed by the surrounding medium. Here we will discuss the Hα line.

The Wavelength of H-alpha

The Hα line is part of the Balmer series and occurs as a result of the transition of the electron from the quantum number $n = 3$ to$n = 2$ in the hydrogen atom. The Hα line occurs at 6562.8 Å which is in the red part of the optical spectrum (Figure 2.3). Hα describes the hot ionised medium by a shock that forms from an SNR or a newly formed star. The ambient ISM needs a temperature $< 2 \times 10^4$ K as above this limit the Hα line cannot be emitted. This temperature limit is where the electron is excited to a state that still bonds to the atom. More temperature / energy will ionized the hydrogen atom. We will utilise Hα survey to indicate whether there is some surrounding filament (Finkbeiner, 2003) potentially associated with our chosen TeV sources.

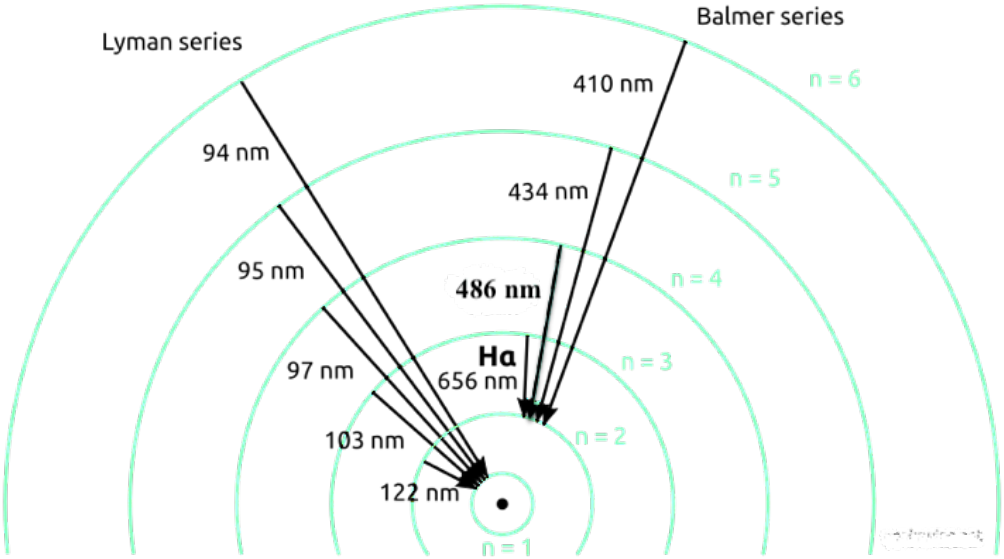

Figure 2.3: Transition of the electron in the hydrogen atom, which produces the Hα line.

The Processes of Balmer Emission from Supernova Remnants

A shock occurs when matter accelerates past the speed of sound in the medium through which it propagates in. There are different types of shocks, with Figure 2.4 showing a schematic of a so-called Balmer shock in SNRs. A Balmer shock needs to satisfy the following conditions: high velocity ($>$ 200 km /s^{-1}), strong hydrogen lines, weak emission of forbidden lines, and the absence of non-thermal X-ray emission (Heng, 2010).

The red dashed line in Figure 2.4 indicates the cosmic-ray and the shock direction where the thick black dashed-line is the shock front (i.e. where the ISM and eject ion shock interact). At the gyroradius (l_{gyro}) of the charged particles(protons or electrons) the material heats up due to the interactions between the shock front and ambient ISM. We can see the number of protons increases in the post-shock region, due to the interaction between ISM and the remnant. Since, the hydrogen atoms dominate the ISM, the number of neutral hydrogen atoms decreases post-shock. The

broad neutrals is the shock transition zone where ionization, charge transfer, and excitation of the medium occurs Figure 2.4 and the broad neutrals is the region that is observable in the Hα optical line.

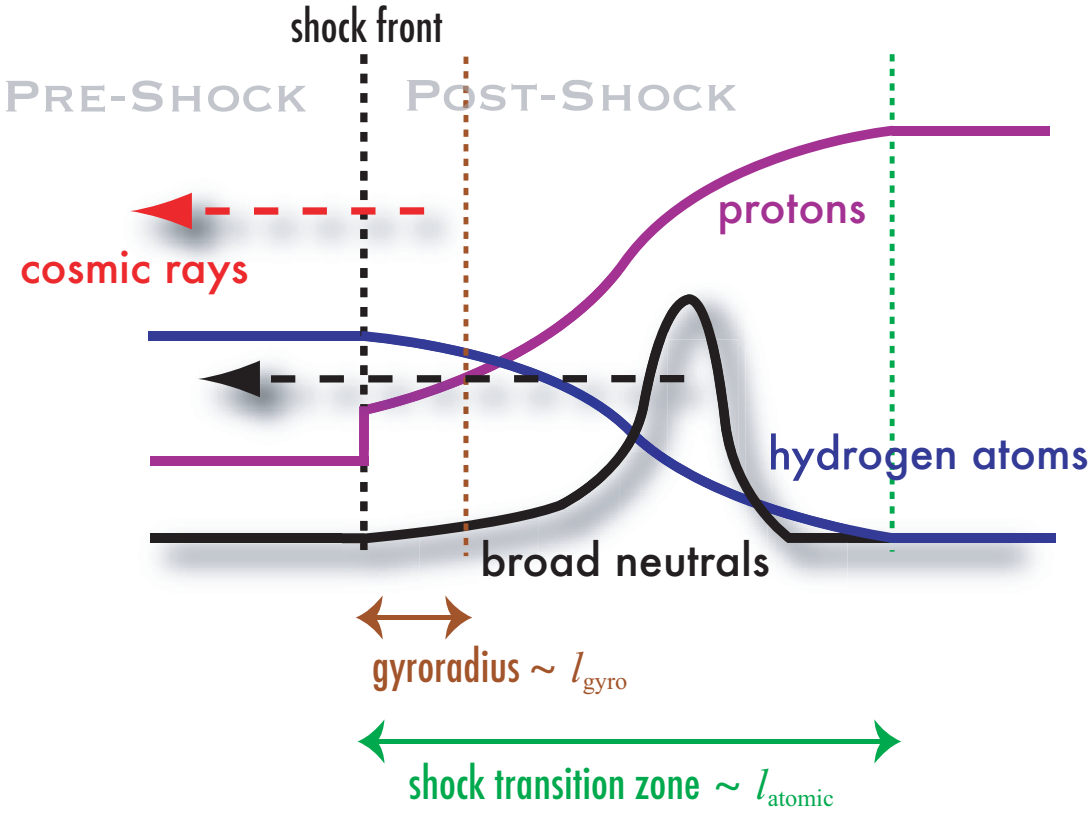

Figure 2.4: Structure of Balmer dominated SNR shocks as they propagate through the ISM (Heng, 2010).

The relationship between the ratio of optical lines and associated gamma-ray emission are an important key for SNR detection. The data from HESS and various Hα sky survey can be a guide to find correlations between both gamma-ray sources and Hα structures. Using the models for SNR and SWB radii and filament detection from the Hα map can help us to link gamma-rays to an optical feature such as SNR.

2.4 H-alpha Voids and bubbles

Another feature worth considering is in fact the lack of Hα emission. Bubbles are volumes of low density, high temperature gas surrounded by ionised and natural shells. The formation of such physical structures is related to hypersonic shocks interacting with the ISM. There are many examples of bubbles in the cosmos such as SWB, planetary nebulae (PNe), and SNR shocks. There are many observable examples of the bubble features, such as the Dumbbell planetary, PN Helix Nebula, SNR SN 1572, and CTB 1 Supernova remnant (Figure 2.5).

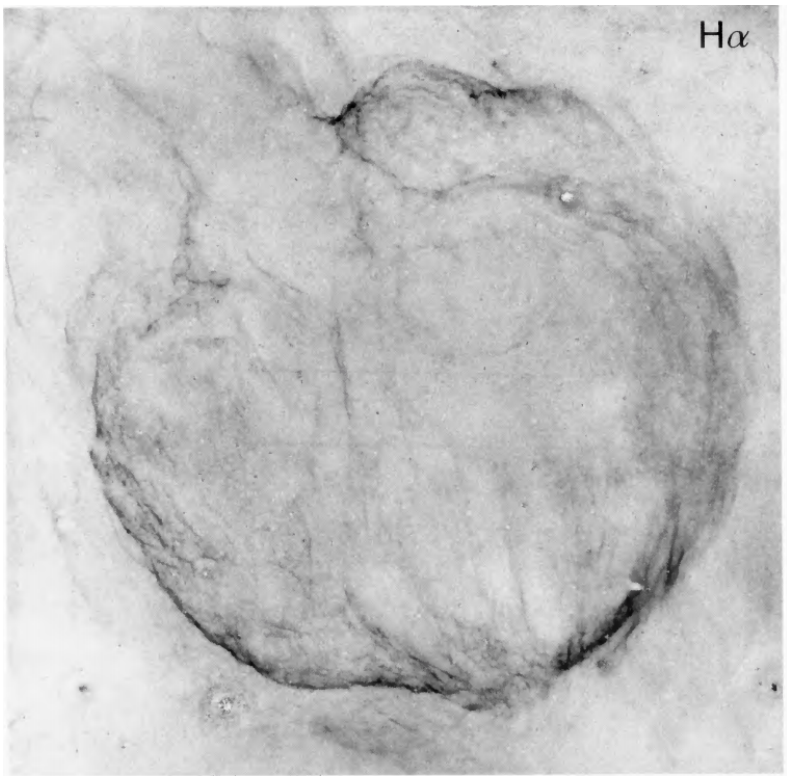

Figure 2.5: Hα image for the CTB 1 supernova remnant, revealing its bubble morphology (Fesen et al., 1997).

These objects have a morphology of a filled disk where the emission of the Hα is not intense in the central region of the sources, meaning it peaks at the edges of the physical source. Due to highly ionized material in the central region, there is less Hα

emission. We will therefore also attempt to search for interesting voids or bubbles in the Hα surveys that might also reveal the presence of SNRs, SWBs or even clusters of massive stars.

3 A First Look at our Selected TeV Gamma-ray Sources

Here, an overview of our Hα and HESS TeV source comparison is presented to concentrate on HESS TeV sources with potentially interesting Hα features. In addition, we discuss these interesting Hα features in the context of their origin as SNRs, stellar wind bubble (SWB), and or pulsar wind nebula. Further discussion of these HESS sources, and the SNR and/ or SWB models is given in Chapters 4 and 5.

3.1 Detection Of TeV Gamma-rays

There are many ways to observe gamma-rays, such as ground-based telescopes that observe Cherenkov radiation interacting with the atmosphere or satellites that preform direct detection of the gamma-ray photon such as the Fermi large area telescope (LAT) can be used for GeV gamma-ray detection from space. Fermi LAT uses a detection method that depends on the interaction of gamma-ray photons producing electrons (e^-) and positrons (e^+) (Atwood et al., 2009). For ground-based gamma-ray observations like HESS, there are two types of observation techniques. The first uses extensive air shower (EAS) arrays, and the second uses imaging atmospheric Cherenkov telescopes (IACTs). IACTs employ an array of telescopes with mirrors that reflect and concentrate Cherenkov light into a camera of photomultiplier tubes to image the Cherenkov emission from gamma particle. This technique provides the energy and direction of the gamma-ray photons. HESS is an example of an IACT array (H.E.S.S. Collaboration, 2018b).

Cherenkov radiation is electromagnetic radiation resulting when particles moving

with a high speed, pass through a medium that has a phase velocity lower than the speed of particle. The particles ionise the surrounding material as they lose speed, and the material emits Cherenkov radiation in the process.

HESS has four twelve metre Cherenkov telescopes arranged in a square that have been operating since 2004. A larger central telescope was added in 2012. The large telescope has a mirror diameter of 28 metres which has been operating since 2013. The observations of gamma-rays by HESS is sensitive down to 1.5% of the Crab Nebula flux in the region of l =283-58 degrees and b = -0.3 $\pm$ 0.7 degrees. Also, HESS has an angular resolution of 0.08 degrees and has an energy range between 0.2 and 100 TeV. The telescopes work independently and observe the same gamma-ray shower, each from a different perspective, allowing us to determine the origin of the gamma-ray. Figure 3.1 shows the Cherenkov radiation detection method principle.

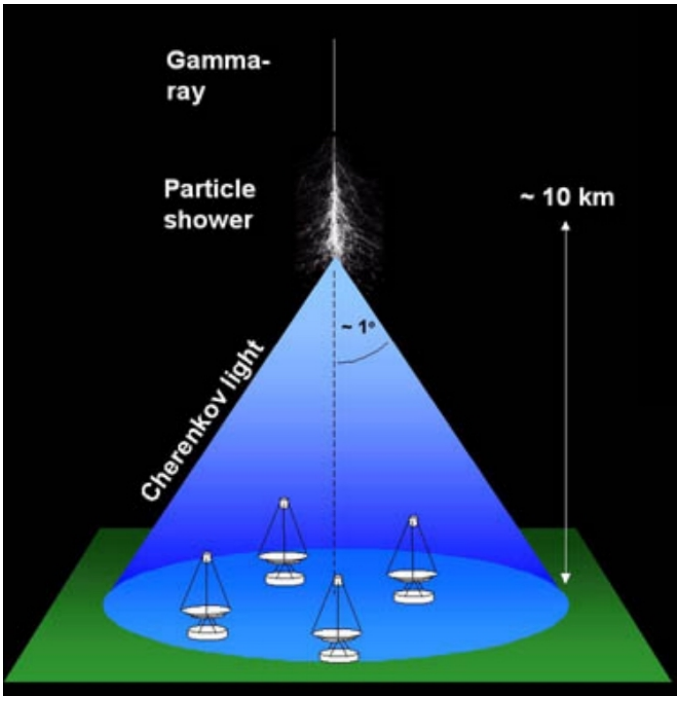

Figure 3.1: Schematics shows how HESS observes gamma-rays, where the gamma-ray interacts with the atmosphere to create Cherenkov light observed by the telescopes.

There are many unidentified TeV sources from the HESS Galactic plane survey (HGPS). In this study, we have taken ten sources from the HGPS (H.E.S.S. Collaboration, 2018b), which have all been chosen due to some interesting features in the nearby Hα emission or its morphology, and avoid considering sources which are already identified such as HESS J0852-463 which is clearly associated with SNR G266.2-1.2 based on its ring-like TeV morphology. The sources that this thesis focused on are listed in Table 3.1, and are all suspected to be either a SNR or a pulsar wind nebula of various ages.

Name of the source	Distant kpc	Age of pulsar kyr	Suspected counterparts
HESS J1303-631	6.6	11	[1]PWNe or SNR
HESS J1356-645	2.4	7.3	[2]PWNe
HESS J1640-465	8.6	5	[3]Old PWNe
HESS J1804-216	4^a	20^a	[4]PWNe
HESS J1813-178	4.7	5.4	[5]PWNe
HESS J1834-087	5.6	60	[7]PWNe
HESS J1837-069	6.6	2.23	[8]PWNe or SNR
HESS J1825-137	4	40	[9]PWN
HESS J1857+026	6.3	21	[10]SNR
HESS J1912+101	4	169	[11]SNR

Table 3.1: Interesting HESS TeV sources considered in this thesis. Information has been collected from [5] Di Palma et al. (2017),[7] Misanovic et al. (2011),[7] Tian, Li, et al. (2007),[8] Anada et al. (2009), [1] Acero et al. (2013), [5] S. Funk et al. (2007), [1] H.E.S.S. Collaboration (2012), [2] Izawa et al. (2015),[3] H.E.S.S. Collaboration (2014),[4] [3] de Wilt et al. (2017), [11] [10] Aharonian et al. (2008c),[9] Abeysekara et al. (2017) and [6] Leahy et al. (2008). (^{a}) There is no information in the literature so we assume a distance 4 kpc. The distance to the nearest pulsar and an age of 20 kyr are assumed for this TeV source.

For each source, the radius of the supernova remnant (SNR) model is assumed to be related to nearby or associated pulsar, and estimated using equation 2.9 (Dermer and Powale, 2013). For our initial investigation, we used the TeV gamma-ray 5σ significance contours of the Galactic plane survey provided by H.E.S.S. Collaboration (2018b). The HESS TeV gamma-ray survey and significance map can be downloaded from the HGPS website[1]. This provides an idea of the distribution of the ISM and the

[1]https://www.mpi-hd.mpg.de/hfm/HESS/hgps/

relationship to the gamma-ray emission.

3.2 H-alpha Full Sky Map

The full sky map for Hα from Finkbeiner (2003) has been used in this work. This map used three surveys: VTSS, SHASSA, and WHAM. The VTSS and WHAM surveys cover the northern hemisphere, while SHASSA covers the southern hemisphere. The Finkbeiner (2003) map has an average resolution of 6 arc-min full width at half maximum (FWHM), which is similar to that of the HESS Galactic plane survey. Therefore, any arc or features detected in Hα can be directly compared to the HESS TeV contours. The Southern Galactic plane observed by the SuperCOSMOS AAO/UKST H-alpha survey (SHS) is used for some TeV sources that require higher resolution. SHS has a high resolution of 0.67 arc-sec and it covers $b = \pm$ 10-13 degrees and l =40-310 degrees (Parker et al., 2005).

The warm ionised medium (diffuse ionised gas) is related to SNRs, planetary nebulae (PNe), H II regions, star formation regions, and O-B stars which produce ultraviolet radiation and/or shocks that heat the ISM and excites hydrogen atoms. To investigate the regions related to HESS sources that are suspected to be associated with Hα features the survey of H II regions from Anderson et al. (2014) and the SNR catalogue provided by Green (2019) will be used. In addition, we use The Australia telescope national facility pulsar catalogue (ATNF pulsar catalogue) to provide us with the details on the energetic pulsars around each source (Manchester et al., 2005a). The age and the distance to each pulsar are taken from Manchester et al. (2005a) or recent literature. Figure 3.2 shows one example in the region at Galactic longitude to l =23-3 degrees with a Galactic latitude of $b\pm$ 6 degrees, where this field of view provides a wide scope to investigate the gas in Hα around the TeV sources.

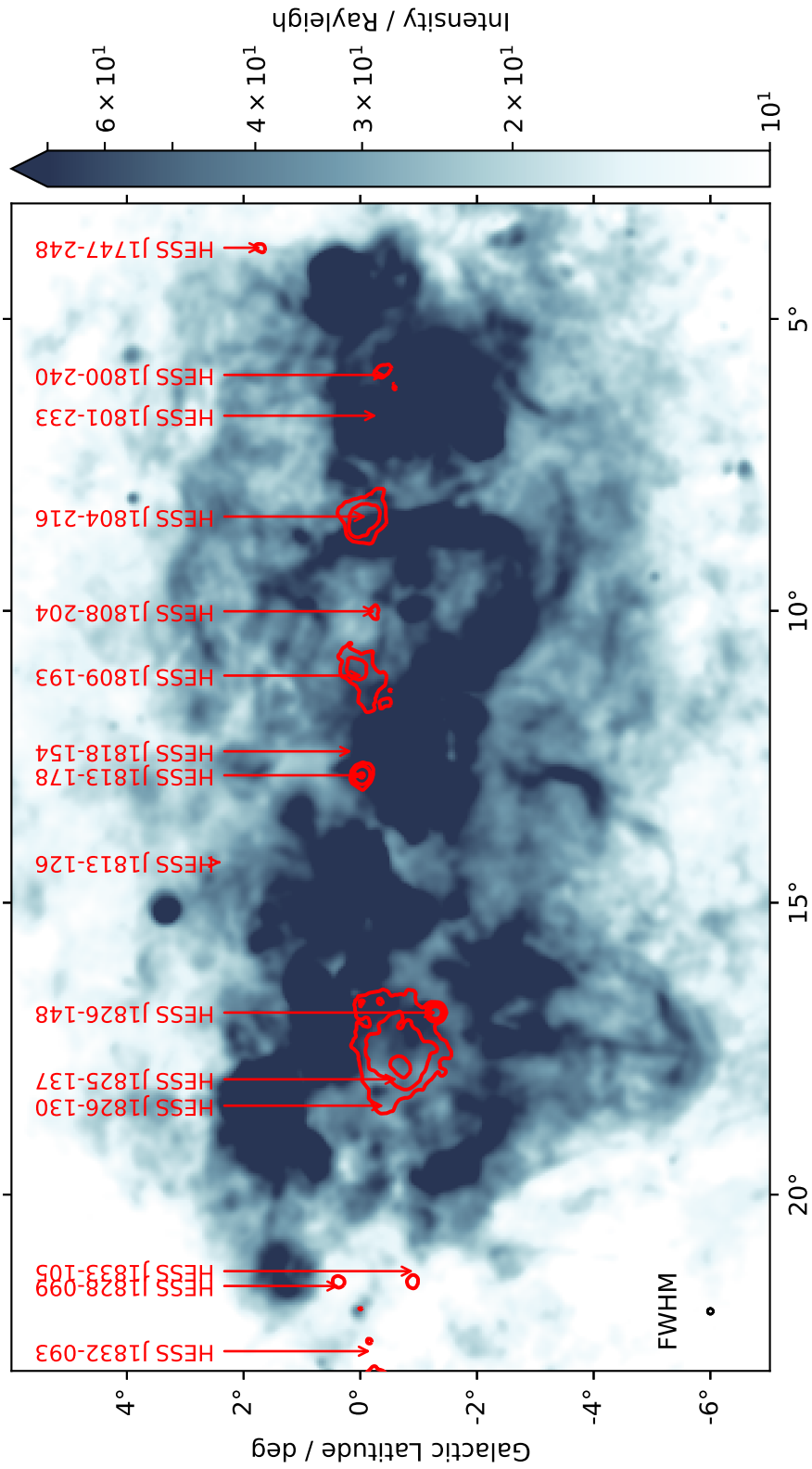

Figure 3.2: An example Hα image by Finkbeiner (2003) map for the region between $l = 0°$ to $23°$ in the Galactic plane. Contours show TeV gamma-ray significance ($5\sigma, 10\sigma, 25\sigma$) from the HESS survey (H.E.S.S. Collaboration, 2018b). See Appendix A.6 for other Hα/TeV comparisons.

For the Hα comparison, Astropy [2], Matplotlib (Hunter, 2007), and Numpy (Virtanen et al., 2019) Python packages were used to overlap the images and the contours. The gamma-ray map shows significance contours at a levels of 5σ,10σ and 25σ, therefore focusing on the convincing TeV gamma-ray detections. Similar Hα TeV comparisons are given in appendix A.6 for other Galactic longitude ranges. We will now provide an initial discussion of the interesting TeV sources listed in Table 3.1.

3.3 HESS J1303-631

HESS J1303-631 was discovered in 2005 by Aharonian et al. (2005b), and it is classified as pulsar wind nebula powered by the pulsar PSR J1301-6305 with a spin-down power $\dot{E} = 1.7 \times 10^{36}$ erg s^{-1}, an age of $\tau_c = 11$ kyr, and a distance of 6.6 kpc. The H.E.S.S. Collaboration (2012) demonstrated that it follows the PWN scenario based on the results of a multi-wavelength gamma-ray, X-ray, and radio studies, which reveal the highest energy gamma-ray and X-ray photons originating from the pulsar. Towards the south, HESS J1302-638 (LS 2883) is a binary system with a distance of 2.6$\pm$0.3 kpc, and it is located 1° from HESS J1303-631. The two TeV sources are unrelated. LS 2883 was observed and discovered by radio surveys and it is located near the open star cluster Cen OB1 (Aharonian et al., 2005b).

The location of HESS J1303-631 is shown in Figure 3.3, and PSR J1301-6305 is offset from the center toward the north-west of HESS J1303-631. We can notice Hα emission on the eastern side and no Hα emission or feature on the western side of the TeV source. We can note the white arc (Figure 3.3) is used to highlight the Hα emission profile. Due to the similarity in the structure of Hα and TeV gamma-ray contours, it might be related to HESS J1303-631 as an SNR or SWB shock boundary with the ISM.

[2] http://www.astropy.org

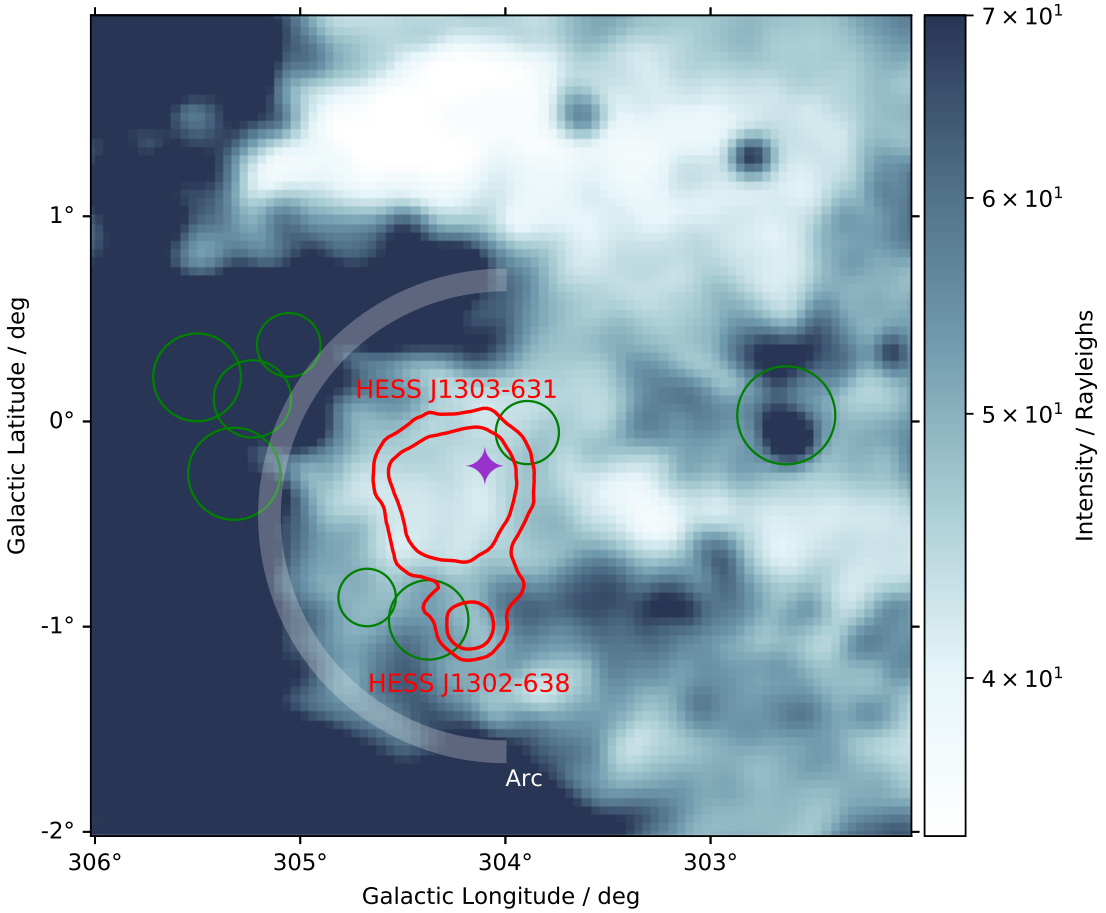

Figure 3.3: Finkbeiner (2003) Hα image in the direction of TeV source HESS J1303-631 and HESS J1302-638 (red contours of the with 5σ and 10σ). H II regions are in green with minimum radius $>$ 500 arc-sec and listed in Table 3.2. The PSR J1301-6305 location is indicated by ✦.

We used the survey of Anderson et al. (2014) to add various H II regions. However, the number of H II regions which we have plotted has been limited due to their larger number. The H II regions with large radius in the FoV of the HESS survey are plotted. These H II regions are listed in Table 3.2.

H II region Name	l degree	b degree	Radius arc-sec	Distance kpc
G302.631+00.030	302.6	0.03	860	4.6
G303.893-00.055	303.8	-0.05	554	
G304.374-00.968	304.3	-0.96	697	
G304.674-00.859	304.6	-0.85	504	
G305.056+00.372	305.05	0.37	558	
G305.233+00.110	305.2	0.1	678	4.9
G305.322-00.255	305.3	-0.25	808	4.9
G305.503+00.214	305.5	0.2	770	

Table 3.2: H II regions located around HESS J1303-631 with their radius and distance provided by Anderson et al. (2014).

3.4 HESS J1356-645

Abramowski et al. (2011) revealed HESS J1356-645 as an extended TeV source with 11% of the Crab nebula flux. This source is associated with the pulsar PSR J1357-6429 with a spin down power of 3.1×10^{36}erg s^{-1}, making a PWN scenario plausible (Abramowski et al., 2011). The pulsar has a distance of 2.4 kpc and an age of τ_c=7.3 kyr, and is the most powerful pulsar around this TeV emission.

Using X-ray observations, Izawa et al. (2015) suggested that the TeV gamma-ray emission of HESS J1356-645 is generated by an old PWN $>$ 10 kyr. Abramowski et al. (2011) studied PSR J1357-6429 with Suzaku X-ray observations, and suggested a distance of 2.4 kpc and a radius of 3 pc. Their results suggest that it is a PWN due to the observed extended region X-ray emission.

HESS J1356-645 is shown in Figure 3.4 and is an interesting candidate due to the presence of a possible Hα arc on the south-east of the TeV source. There is no H II region towards HESS J1356-645.

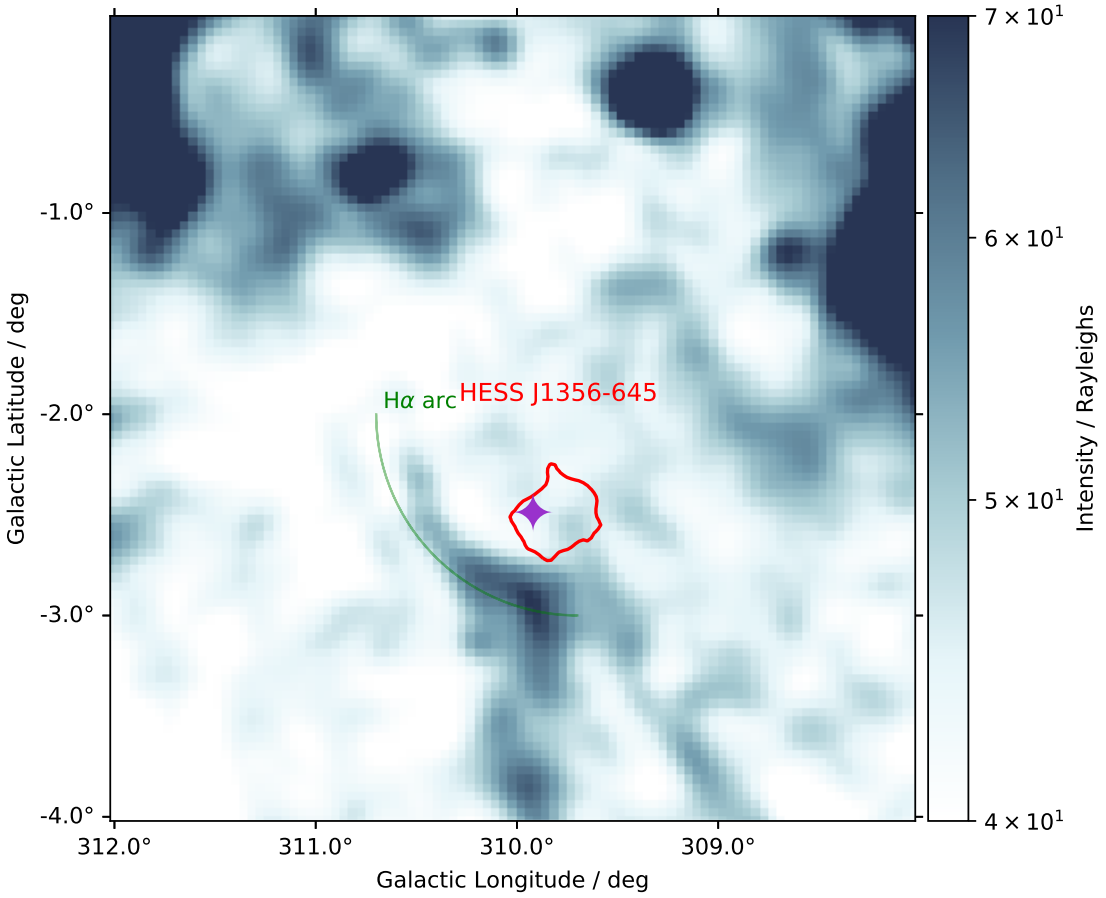

Figure 3.4: Hα image from Finkbeiner (2003) is in the vicinity of HESS J1356-645 (red contour with 5σ significance level). The green line on the west-side overlap an interesting Hα feature. PSR J1357-6429 is denoted by ✦.

3.5 HESS J1640-465 and HESS J1641-463

HESS J1641-463 is located at Galactic (l, b)=(338.52,0.09. HESS J1640-465 is located at Galactic (l, b)=(338.32,-0.02) degrees and it is possibly associated with SNR G338.3-0.0, which was discovered by the 843 MHz Molonglo Galactic Plane Survey (Clark and Caswell, 1976). The diameter of HESS J1640-465 is about 8 arc-min, and the known H II regions are plotted in Figure 3.5. The pulsar PSR J1640-4631 with spin down power 4.4×10^{36}erg s^{-1} has been suggested as a possible generator of HESS J1640-465

(H.E.S.S. Collaboration, 2006). Supan et al. (2016) modelled a hadronic scenario powered by SNR G338.3-0.0 for HESS J1640-465 and found that the model energy which is required for the hadronic scenario is larger than that observed by a factor of 1000 times. However, radio observations obtained by Castelletti et al. (2011) and Lau et al. (2017) studied molecular clouds and gas towards SNR G338.3-0.0 and HESS J1641-463 and conclude that the PSR J1640-4631 may contribute in enhancing the TeV emission from HESS J1640-465 but not from HESS J1641-463.

The presence of HESS J1640-465 is shown in Figure 3.5, and HESS J1641-463 is towards the east of HESS J1640-465. The Hα shows interesting morphology towards the south of both HESS J1640-465 and HESS J1641-463. We will study the possibility of it originating from a SNR or SWB, which in turn could be related to the TeV sources.

Table 3.3 lists the H II regions towards HESS J1640-465 as shown in Figure 3.5. Furthermore, H II regions G338.407-00.918 and G338.679-00.795 at the south side of HESS J1640-465 and G338.4+0.0 and G338.45+0.06 is noticed overlapping on the TeV gamma-ray emission. Also, we notice that there is no emission in Hα between the TeV sources and the H II regions. We display of H II regions to a radius $>$ 300 arc-sec.

H II region Name	l degree	b degree	Radius arc-sec	Distance kpc
G338.350+00.221	338.3	0.2	412	
G338.407-00.918	338.4	-0.9	633	
G338.430+00.048	338.4	0.04	346	
G338.679-00.795	338.6	-0.7	646	
G338.861+00.597	338.8	0.5	460	
G339.169-00.698	339.1	-0.6	584	
G339.233+00.243	339.2	0.2	484	11.2
G339.585-00.104	339.5	-0.1	300	13.3

Table 3.3: List of H II regions presented in Figure 3.5 and their distance (Anderson et al., 2014).

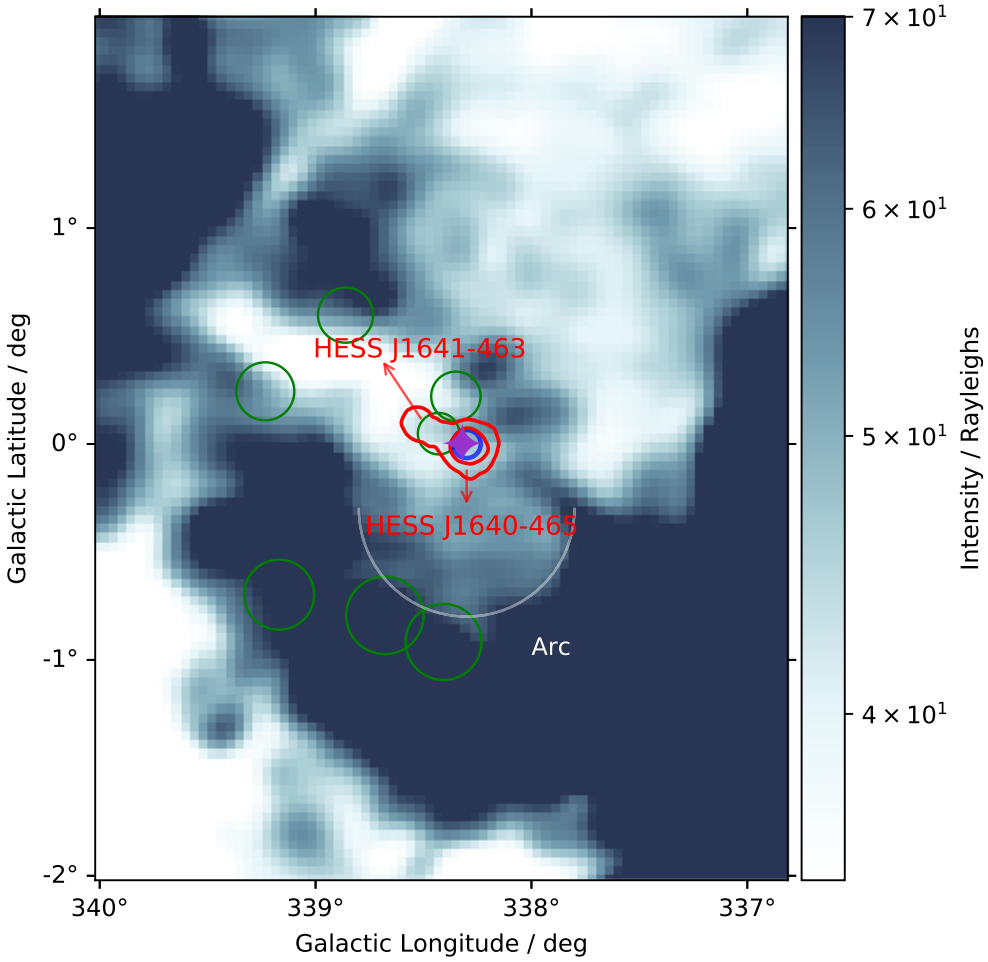

Figure 3.5: Hα image by Finkbeiner (2003) towards the TeV emission of HESS J1640-465 and HESS J1641-463 (red contour 5σ and 10σ significance level). The blue circle indicates SNR G338.3-0.0. PSR J1640-4631 location is denoted by ✦. The H II regions are in green and are listed in Table 3.3. The Hα feature indicated by a white arc.

3.6 HESS J1804-216

The H.E.S.S. Collaboration (2006) described HESS J1804-216 as one of the brightest TeV sources with 25% of the Crab Nebula flux and is shown in Figure 3.6. The region around HESS J1804-216 shows molecular gas in CO observation (de Wilt et al., 2017). The red contours in Figure 3.6 shows that HESS J1804-216 has a major diameter of 1°.

PSR J1803-2137 with 392 km s^{-1} proper motion velocity, is on the north side of the center TeV source and the Hα image shows emission on the west side. It is suggested to be associated with PSR J1803-2137 which has a spin-down power of 2.2×10^{36} erg s^{-1}, an age of τ_c=16 kyr and a distance of 4.4 kpc (Manchester et al., 2005b). Lin et al. (2013) has proposed from the X-ray observation study two possible TeV emission scenarios for this source: first a hadronic scenario powered by SNR G8.7-0.1, and second a PWN scenario powered by PSR J1803-2137. However, an issue with the latter possibility is that the direction of the proper motion of the pulsar is pointed towards the center of the SNR G8.7-0.1 (Brisken et al., 2006).

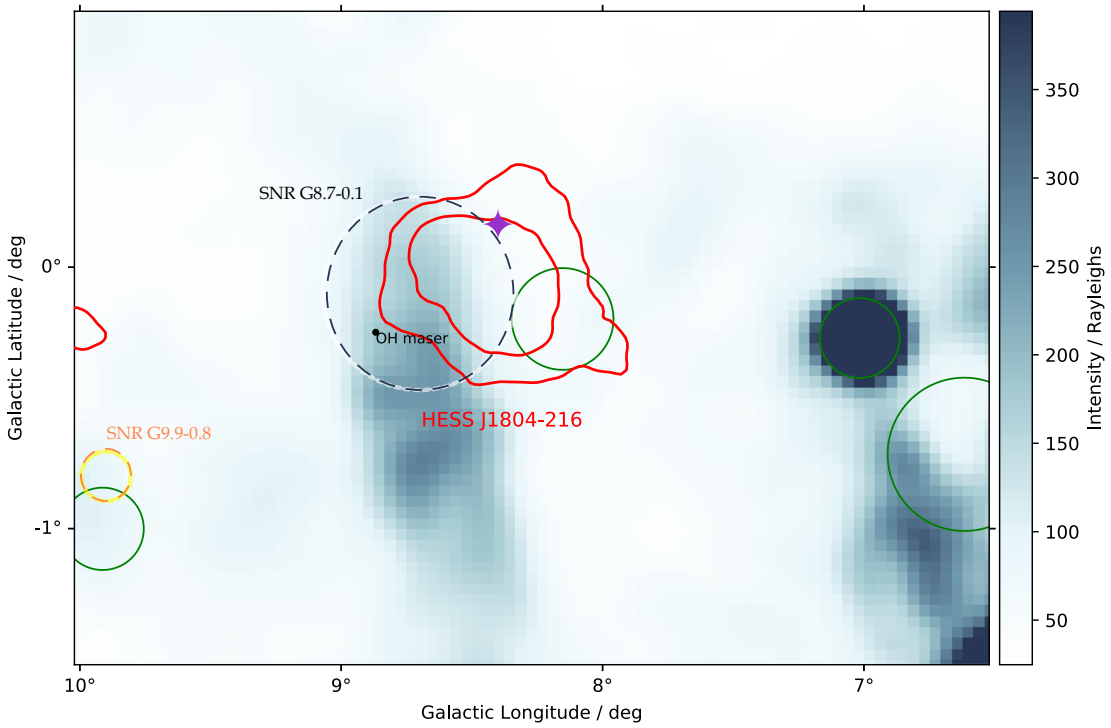

Figure 3.6: Finkbeiner (2003) Hα image towards HESS J1804-216 (red contours 5σ and 10σ significance level). H II region G008.153-00.198 overlap with TeV emission. There is optical SNR (yellow) circle discovered with optical wavelengths by M. Stupar et al. (2011). PSR J1803-2137 is denoted by ✦. The white dash line is for SNR G8.7-0.1. The OH maser is shown in black dot and it is located within the SNR.

The Mopra radio telescope at 22 GHz and southern Galactic plane survey (HOPS) shows that there are dense molecular clouds (de Wilt et al., 2017), as well as a 1720 MHz OH maser[3] (Hewitt and Yusef-Zadeh, 2009). This maser is located at a distance of 4.5 kpc toward HESS J1804-216. The diameter of the SNR G8.7-0.1 is 45 arc min. This represents a shock between the SNR which was presented in Hewitt and Yusef-Zadeh (2009) and the molecular cloud. The optical SNR G9.9-0.8 is indicated by a yellow dotted circle with a diameter of 12 arc-min Figure 3.6 (Stupar and Q. Parker, 2011), but we believe that there is no relation to HESS J1804-216 due to the large separation.

Table 3.4 lists locations and radii of the nearby H II regions, however, their distances have not yet been determined.

H II region Name	l degree	b degree	Radius arc-sec
G006.616-00.717	6.6	-0.7	1056
G007.015-00.271	7.0	-0.27	550
G008.153-00.198	8.1	-0.19	701
G009.913-01.002	9.9	-1.0	567

Table 3.4: H II regions plotted in Figure 3.6 by Anderson et al. (2014).

In this region, an interesting quite notable linear Hα feature appears on the west side of HESS J1804-216. Further discussion on this region will be in chapter 4 using high resolution Hα observations.

[3]Microwave Amplification by Stimulated Emission of radiation which is a physical phenomenon in star forming regions, and evolved stars and in their circumstellar envelopes. 1720 MHz OH maser are specifically created when SNR shock collides with molecular cloud.

3.7 HESS J1813-178

This compact TeV source has been investigated extensively (Brogan et al., 2005; Funk et al., 2007; Araya, 2018; Halpern et al., 2012; Fang, 2010) and is shown in Figure 3.7. The nearby PSR J1813-1749 has an X-ray luminosity of 2×10^{34} erg s^{-1}, and is one of the most energetic pulsars with a spin down power $\dot{E} = 5.6 \times 10^{37}$ erg s^{-1} and an age of 5.6 kyr (Halpern et al., 2012). Also, it is located at a distance of 4.8 kpc and its X-ray pulsar wind nebula has a compact radius of 1.7 pc, which suggests a young age PWN. Using the observation of X-ray and gamma-ray flux in equation 2.8 the PWN ratio $f_x(2-10 \text{ keV}) / f_\gamma(>200 \text{ GeV})$ is approximately 0.4, which fits the age of PSR J1813-1749 (Halpern et al., 2012) .

Previously, PSR J1813-1749 was presumed to be related to the SNR G12.8-0.0, which has a small diameter of 1.5 arc min and a distance of 4 kpc (Brogan et al., 2005). However, Halpern et al. (2012) suggests that SNR candidate G12.82-0.2 and HESS J1813-178 are not related due to the large distance separating them 1-2 kpc.

Table 3.5 listed locations and radii of the H II regions. Looking at the Hα emission in Figure 3.7, we note an arc with clumps in the south side of the TeV gamma-ray emission of HESS J1813-178, and some of these clumps are identified as H II regions. We will investigate a connection between this Hα emission in the south and HESS J1813-178 in Chapter 4.

H II region Name	l degree	b degree	Radius arc-sec	distance kpc	$\pm$distance kpc
G012.197+00.798	12.197	0.799	525		
G012.359-00.554	12.359	-0.553	507		
G012.515+00.066	12.516	0.067	312		
G012.523-00.611	12.523	-0.610	503		
G012.742+00.390	12.743	0.391	537	2.6$\pm$0.7	0.7

Table 3.5: H II regions plotted in Figure 3.7 (Anderson et al., 2014).

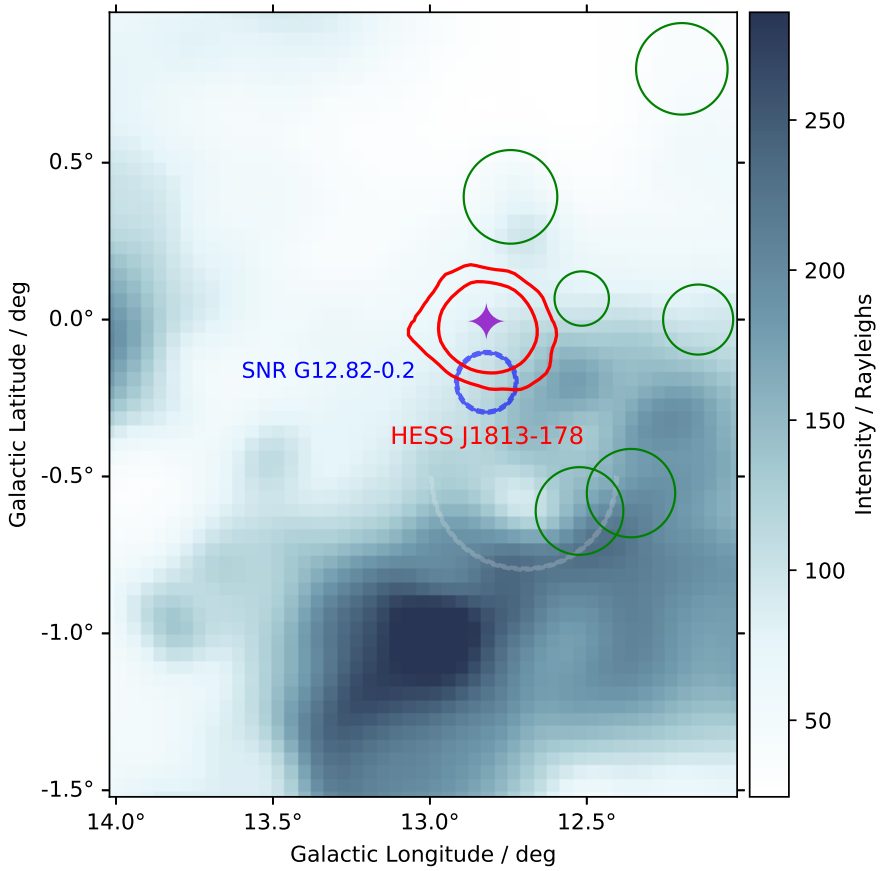

Figure 3.7: Hα image from Finkbeiner (2003) in the direction of TeV gamma-ray emission of HESS J1813-178 (red contours of 5σ and 10σ significance level). The pulsar PSR J1813-1749 is denoted by ✦. The SNR candidate G12.82-0.2 is the blue circle towards the south with a diameter of 1.5 arc min. The Hα arc discussed in text is also labelled.

3.8 HESS J1834-087

The detection of HESS J1834-087 was presented in (H.E.S.S. Collaboration, 2006), and confirmed by the MAGIC telescope (Albert et al., 2006). The location of this source is near the shell-type SNR W41 (G23.3-0.3) (see Figure 3.8). Furthermore, Bartko and Bednarek (2008) proposed that, due to the surrounding highly dense ISM, HESS J1834-087 could not rapidly expand, resulting in a hadronic interpretation.

PSR J1833-0827 is located on the north side of HESS J1834-087. In addition, pulsar PSR J1833-0827 is about 24 arc-min from the center of the observed TeV gamma-rays (Bartko and Bednarek, 2008). The spin down power of the pulsar is $\dot{E} = 5.8 \times 10^{35}$ erg s^{1}, and the age of the pulsar is 150 kyr with a distance of 4.5 kpc (Manchester et al., 2005b). The strong infrared radiation field in this region supports that it may be from the interaction of the SNR shock (Bartko and Bednarek, 2008). PSR J1833-0827 has a spin period of 85 ms, with a proper motion velocity of 740 km s^{-1}, suggesting a relationship with W41 (Petroff et al., 2013b).

Using XMM-Newton observations,Esposito et al. (2011) found that PSR J1833-0827 has an X-ray and radio pulsar wind nebula, and they discussed the relationship of the pulsar and HESS J1834-087. They suggest that PSR J1833-0827 is associated with this source due to the pulsar's age ($\sim$ 150 kyr), and that the proper motion of the pulsar is traced back to the center of TeV gamma-ray emission of HESS J1834-087. However, the ratio $F_{\gamma}(1-10\ \mathrm{TeV})/F_{x}(2-1\ \mathrm{KeV}) \sim 50$, is less than that expected from an old SNR of 10^5 yr. Thus it is not sufficient to radiate the required energy as presented by Esposito et al. (2011).

There are four other TeV sources in Figure 3.8; HESS J1832-085 and HESS J1832-093, both of which have a small diameter compared with HESS J1834-087. The sources, HESS J1832-085 and HESS J1828-099 are still unidentified. HESS J1832-093 is identified as a binary system (K. Mori et al., 2017), with HESS J1833-105 is identified as a PWN (H.E.S.S. Collaboration, 2018b). The Hα emission shows overlap with the gamma-ray emission in the south-side, but there is a lack of Hα emission on the west side. We are interested in a possible Hα emission in the northern region as indicated in Figure 3.8. Finally, Table 3.6 listed locations and radii of the H II regions towards HESS J1834-087.

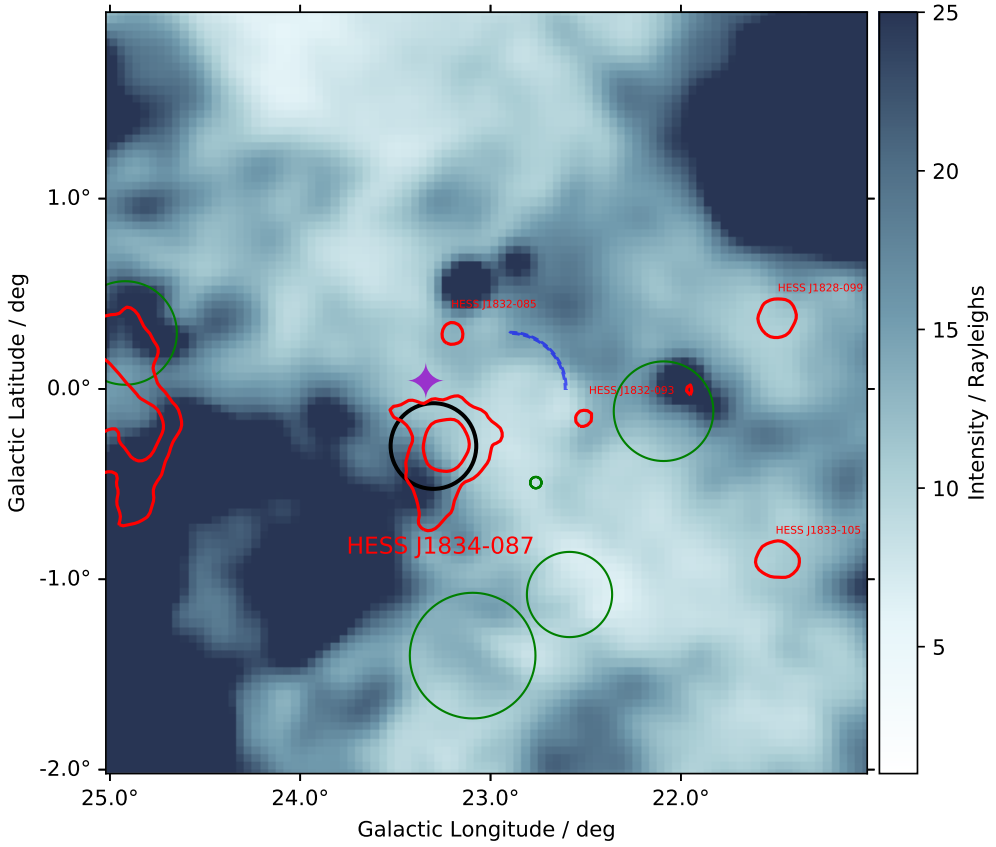

Figure 3.8: Finkbeiner (2003) image of Hα emission towards HESS J1834-087 (red contours 5σ and 10σ level). H II regions are in green circles and listed in Table 3.6. The location of PSR J1833-0827 is denoted by ✦. Many other TeV sources are in the field of view. HESS J1828-099 and HESS J1832-085 were recently detected and still unidentified. HESS J1833-105 is identified as a PWN, and the last source is HESS J1832-093 may have an X-ray XMMU J183245-0921539 counterpart. The blue arc indicates interesting 'arc' region in Hα.

H II region Name	l degree	b degree	Radius arc-sec	Distance kpc
G022.090-00.117	22.09	-0.11	942	4.2
G022.585-01.081	22.5	-1.08	806	
G022.760-0.485	22.76	-0.48	4.8	
G023.094-01.402	23.09	-1.4	1188	

Table 3.6: H II regions in the Figure 3.8 (Anderson et al., 2014).

3.9 HESS J1837-069

HESS J1837-069 was first detected in the second HESS galactic plane survey and it was found that the flux was approximately 13% Crab nebula (H.E.S.S. Collaboration, 2006). Later, it was detected in X-rays by the Advanced Satellite for Cosmology and Astrophysics (ASCA) Galactic plane survey (Anada et al., 2009). However, HESS J1837-069 was studied by Anada et al. (2009), and they confirmed the presence of PSR J1838-0655 which has a spin down power of 5.5×10^{36} erg s^{-1}, it is located at a distance of 6.6 kpc and an age of 22 kyr (Manchester et al., 2005b). The existence of this pulsar led them to suggest a pulsar wind nebula scenario for HESS J1837-069. In the west of HESS J1837-069, there is another TeV source HESS J1841-055 which is suggested to to PWN (Acero et al., 2013).

HESS J1837-069 has high intensity clouds of Hα emission towards its north and south regions. As shown in Figure 3.9, at the centre of HESS J1837-069 there is no Hα emission. Plotting the H II regions from the WISE survey provided by Anderson et al. (2014), we notice that there is an interesting H II region partially overlapping the TeV emission (see Table 3.7). This H II region, G25.867+0.11, is located at a distance of 6.5 kpc. TeV source, HESS J1841-055 is located 1.5° to the west and Sguera et al. (2009) suggests that it is related to the SNR candidate G26.6-0.1.

H II region Name	l degree	b degree	Radius arc-sec	Distance kpc
G024.734+00.087	24.735	0.087	85	6.4±0.8
G024.919+00.294	24.920	0.294	979	
G025.867+00.118	25.867	0.119	644	6.5
G026.797-00.113	26.797	-0.112	783	10.8
G024.805+00.101	024.805	+00.101	6.3±0.6	

Table 3.7: H II regions in Figure 3.9 (Anderson et al., 2014).

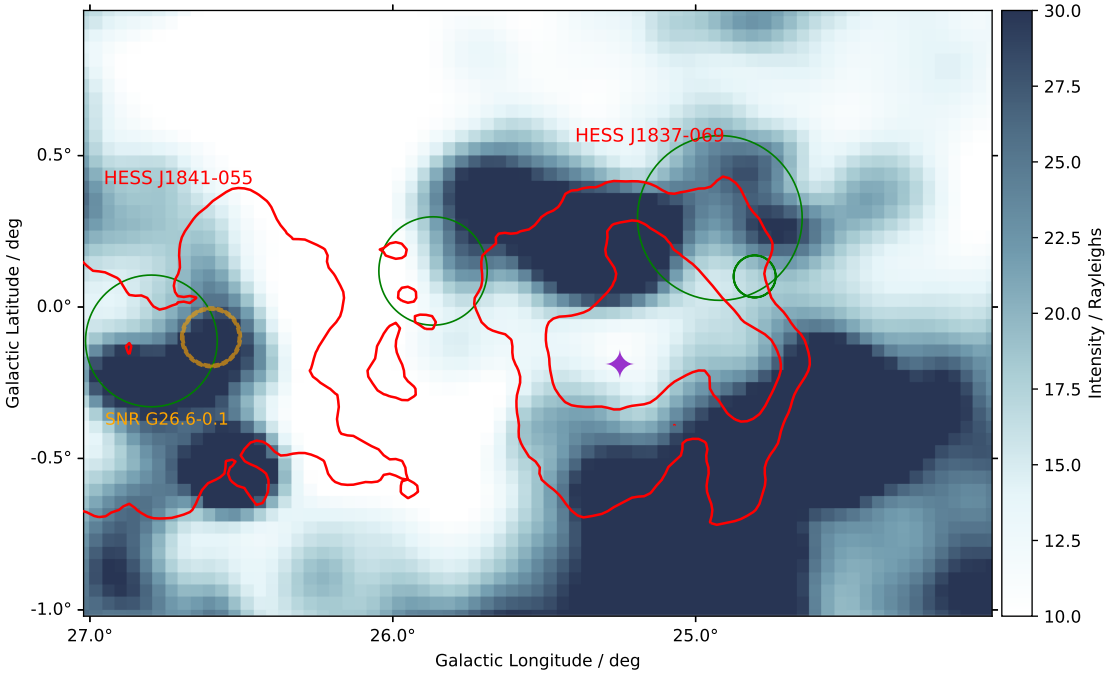

Figure 3.9: Hα image by Finkbeiner (2003) towards the TeV emission HESS J1837-069 (red contour with significance 5σ and 10σ). The location of PSR J1838-0655 is denoted by ✦. H II regions are in green circle and listed in Table 3.7. There is on the right HESS J1841-055 and in orange the SNR candidate G26.6-0.1 is shown.

3.10 The HESS J1825-137 region

This region has several TeV sources which have a complex morphological form that contains many Hα clouds and arcs (see Figure 3.10). Voisin et al. (2016) investigated the HESS J1825-137 PWN, powered by PSR J1826-1334 with spin down power of 2.8$\times$ 10^{36} erg s^{-1}, an age of 20 kyr, and located at a distance of 4 kpc. Another pulsar PSR J1826-1256 which has spin down power $\dot{E} = 3.6 \times 10^{36}$ erg s^{-1}, is located at 1.5 kpc, and has an age of 14 ky (Manchester et al., 2005b). PSR J1826-1256 has a period of P=100 ms and powers the X-ray PWN G18.5-04 which may also be related to the adjacent HESS source HESS J1826-130 (Voisin et al., 2016).

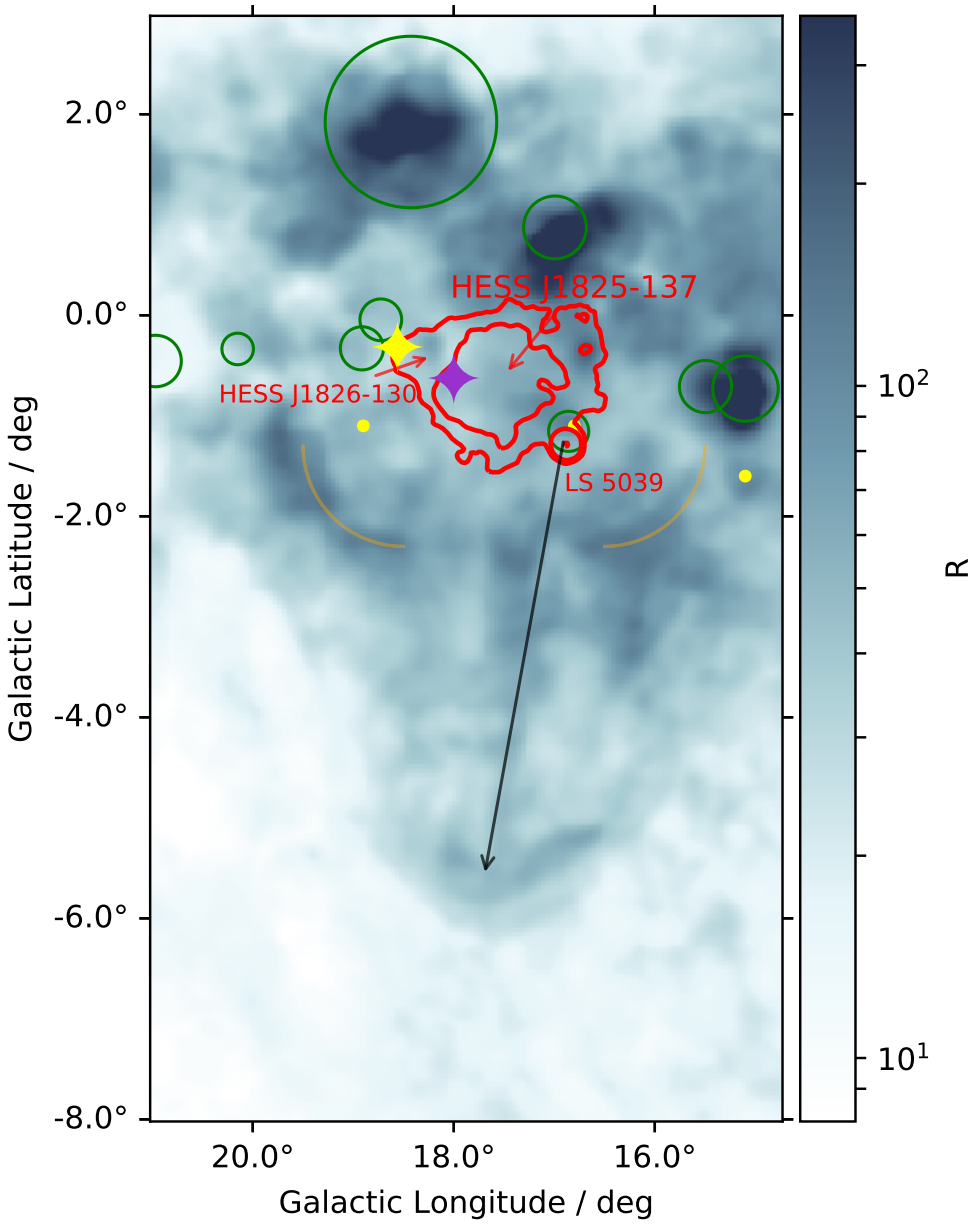

Figure 3.10: Hα image by Finkbeiner (2003) towards the TeV emission of LS 5039 HESS J1826-148 is noted and HESS J1825-137 and HESS J1826-130 (red contour 5σ, 10σ and 50σ). The location of the high energetic pulsars PSR J1826-1256 and PSR J1826-1334 are denoted by ✦. The Hα jet and bow shock is clearly seen in the south and it extends 4° away. The orange arc is the Hα SNR discussed in Voisin et al. (2016) and Stupar et al. (2008).

Furthermore, The microquasar LS 5039 was detected by HESS in TeV gamma-rays

(Aharonian et al., 2005a; Aharonian et al., 2006b), and was denoted as HESS J1826-148. It has a point like TeV emission morphology and it is located at a distance of 2.9 ± 0.8 kpc (H.E.S.S. Collaboration, 2018b; Yamaguchi et al., 2018). This binary system has two objects; a star with spectral type O7A, and another compact object. It is not clear if this compact object is a black hole or neutron star.

Interestingly, when we zoom out to a field of view of $>4^{\circ}$ from this region in the Hα image Figure 3.10, there is what appears to be a jet, which indicates an outflow streaming in a southerly direction. At the end of the jet, there appears to be bow shock morphology which can be traced back to the TeV emission, and is clearly shown in Figure 3.10. This high speed material propagating through the ISM possibly may need a powerful source such as a black hole, neutron star or pulsar which are generally believed to generate such phenomena. Similar to quasars, the compact object (black hole or neutron star) can create streams of material from a companion star. The accretion disk heats up the material by friction and jets are formed perpendicular to the accretion disk. Jets may also be created in asymmetric SN explosion such as in long gamma-ray burst (LGRBs). In chapter 5 we will investigate this Hα jet and its possible relation to HESS J1825-137 or HESS J1826-148 (LS 5039).

3.11 HESS J1857+026

HESS J1857+026 is an unidentified TeV source and the pulsar PSR J1856+0245 with an age of 21 kyr was discovered with radio observations. It is estimated to be located at 9 kpc distance (Aharonian et al., 2008a). PSR J1856+0245 is shown on the northern side of HESS J1857+026 ()Figure 3.11). As it is a powerful pulsar with spin down power 4.6×10^{36} erg s^{-1} (Manchester et al., 2005b) in this region, we will assume that this is also the distance to HESS J1857+026 . X-ray observations showed no evidence of a PWN, and the source was also observed in gamma-rays by *Fermi*-LAT and MAGIC (Aleksić et al., 2014). The lack of extended GeV-TeV observed by other

surveys suggests a composite SNR scenario (Aleksić et al., 2014).

HESS J1858+020 is another nearby source that is located at approximately 0.4° from HESS J1857+026 as seen in Figure 3.11. Paron et al. (2011) studied this source in radio wavelengths and concluded that the TeV emission of HESS J1858+020 is a result of the hadronic interaction of the accelerated cosmic rays with molecular gas. HESS J1858+020 is related to SNR G035.6-0.4 Paron et al. (2011). The presence of H II regions at 3.7 kpc, found next to a molecular gas cloud, and a two generator scenario is possible due to the extended emission at 1 TeV.

The most interesting feature we found was circular Hα dip emission in a bubble morphology towards the TeV gamma-ray contours of HESS J1857+026 and HESS J1858+020. Figure 3.11 shows both TeV sources. The top panel is with H II region listed in Table 3.8. Bottom panel shows the dip in Hα. To check the existence of this circular feature, we will use independent Hα survey (VTSS and SHASSA) to investigate this feature in Chapter 4.

H II region Name	l degree	b degree	Radius arc-sec	Distance kpc
G035.187+00.892	35.18	0.89	972	8.9
G035.559-00.824	35.5	-0.8	876	9.9
G036.634-00.812	36.6	-0.8	859	
G037.236+00.741	37.2	0.7	713	
G037.028-00.202	37.02	-0.2	420.0	6.8
G037.347-00.147	37.34	-0.14	594.0	10.0

Table 3.8: H II regions are presented in Figure 3.11 using Anderson et al. (2014) survey.

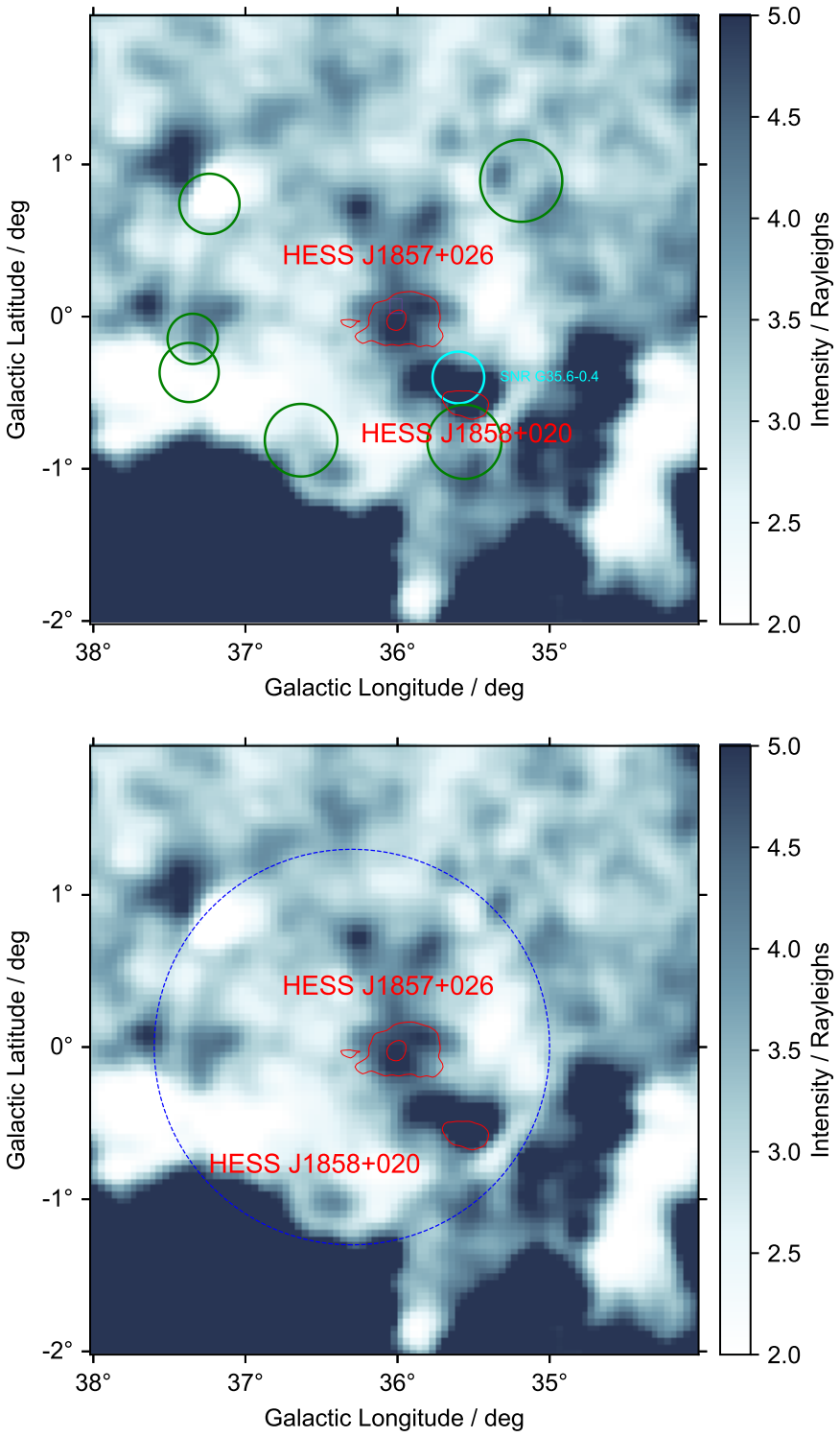

Figure 3.11: (Top)Hα image by Finkbeiner (2003) towards HESS J1857+026 and HESS J1858+020 (red contours 5σ and 10σ significance). The location of PSR J1856+0245 is denoted by ✦. H II regions are in green and listed in Table 3.8. SNR G35.7-0.4 shown in cyan. (Bottom) Hα image by Finkbeiner (2003) towards HESS J1857+026 and HESS J1858+020 (red contours 5σ and 10σ significance). The location of PSR J1856+0245 is denoted by ✦. The blue dashed circle indicates the ring-like Hα feature discussed in text.

3.12 HESS J1912+101

HESS J1912+101 was reported by Aharonian et al. (2008c) with a flux approximately 10% of the Crab nebula Figure 3.12. The nearby pulsar PSR J1913+1011 has a spin down power of 2.9×10^{36}ergs s^{-1}, a characteristic age of 170 kyr, a period of 35.9 ms, and it is located at a distance of 4.5 kpc (Manchester et al., 2005b). The observation by Aharonian et al. (2008c) represents the first prediction of this source as a PWN with the presence of the pulsar. However, HESS J1912+101 was more recently suggested to be an SNR candidate based on its TeV shell-like morphology (H.E.S.S. Collaboration, 2018a).

HESS J1912+101 at the 5σ significance level is shown in Figure 3.12. The Finkbeiner (2003) Hα image shows that there is a lack of Hα map intensity toward the TeV gamma-ray emission contours. On the south-east side, we note there is a possible Hα arc. There are several H II regions towards HESS J1912+101 and they are listed in Table 3.9. We will further discuss this arc in Chapter 4.

H II region Name	l degree	b degree	Radius arc-sec	Distance kpc
G044.224+00.085	44.2	0.08	319	7.7
G044.379-00.327	44.3	-0.32	302	6.1
G045.002-00.611	45.0	-0.61	350	4.9 near -7.1 far
G045.191-00.486	45.19	-0.48	333	

Table 3.9: A list of the H II regions in Figure 3.12 with their radii and distances (Anderson et al., 2014).

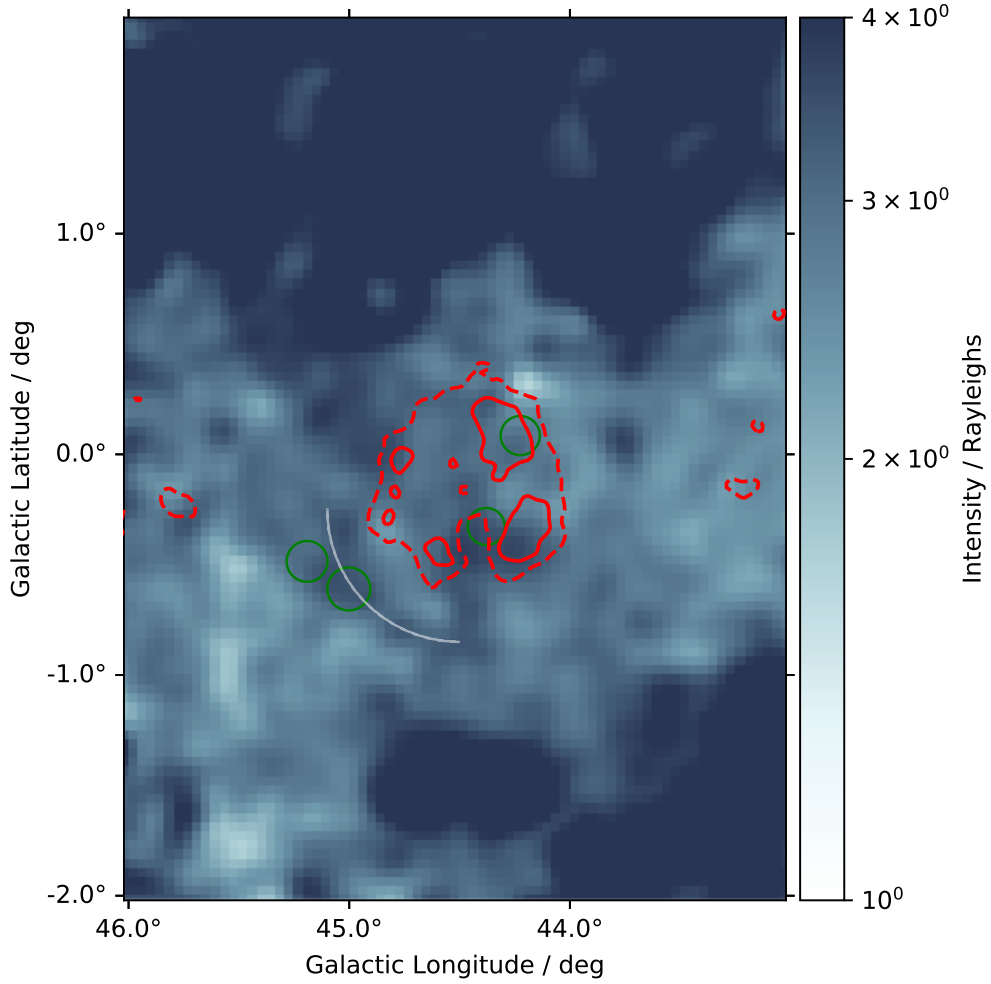

Figure 3.12: Finkbeiner (2003) Hα image towards the TeV emissions of HESS J1912+101 (red contours with 5σ level and dashed line with 3σ level). PSR J1913+1011 is indicated by the ✦. There are H II regions in green and they are listed in Table 3.9.

4 A closer look at our chosen TeV gamma-ray sources

Here, we will expand our work from chapter 3. Models for the SWB and SNR expansion will be implemented in all of our chosen sources. The SWB model is based on equation 2.10 where we assume two limits for the energetics of the progenitor star having spectral types O2 and O9. Assuming ISM number density of 0.1 particle per cm^3 the SWB radius for the spectral types O2 is 221 pc and radius for the spectral types O9 is 148 pc. The SNR model uses equation 2.9 which depends on the ambient density and the initial star mass and time since the SN event. Table A.1 shows the result of different ISM number densities on the SNR radius model. The radius of the SNR varies with time and ISM number density n=0.1 cm^{-3} where at 10^3 yr and 10^4 yr radii $\sim$ 10 pc and $\sim$ 46 pc respectively. The SNR radius model Table 2.2 is used as a guide for our calculations in term of the ISM number density. Also, we will present the model which matches any interesting features in Hα potentially associated with the TeV emission, or from the literature.

As per Chapter 3 we have adopted a minimum significance of 5σ for our TeV contours to define the edges of the sources and to support our morphology discussion. However, in some cases, we used the 3σ level TeV gamma-ray contours to investigate possible extensions to the TeV emission. Additionally, archival catalogues are used to indicate the H II regions and to investigate plausible relations between the Hα emission and our chosen HESS TeV sources.

Furthermore, Radio continuum observations are one of the most helpful tools to investigate the observed optical features such as the Hα optical line. As a shock wave propagates through the ISM at high speeds ($\sim$ 2000 km s^{-1}), SNRs lose energy

through radiation in radio and other electromagnetic wavelengths. The SNRs catalogue from Green (2019), and the NRAO radio 8.35 GHz survey from Langston et al. (2000) were used to compare with observed features in Hα and to support our model predictions. We have limited the contours in these radio observations to be above the noise level which is around 1-2 Jy beam^{-1} (Langston et al., 2000).

We will now discuss each TeV source and investigate any interesting features in some depth.

4.1 HESS J1303-631

The first source that we will present is HESS J1303-63 which is classified as a PWN (H.E.S.S. Collaboration, 2012). Towards the east side of HESS J1303-63, we notice the Hα emission "wraps" around the TeV emission as seen in Figure 4.1 (see also white arc). Application of the SNR model assuming an ISM number density shows the SNR shock location prediction in relation to any Hα feature. The SNR model requires assuming a progenitor star age and distance to the source. For the age estimation, we use the characteristic age and dispersion measurement (DM) of the powerful pulsar towards the TeV gamma-ray emission or the associated pulsar assumed by the literature. PSR J1301-6305 here, using an ISM density of 0.006 particle per cm^3, and the age and distance of the PSR J1301-6305, we can estimate the radius of the predicted SNR. We used a characteristic age for PSR J1301-6305 of 11 kyr and a dispersion measurement distance of 6.6$\pm$0.5 kpc (Sushch et al., 2017). This dispersion measure distance is not always a reliable technique, and can affect the pulsar distance. Therefore, the SNR model in Figure 4.1 assumes an error of ± 0.5 kpc in regards to its distance which is indicated by annulus. The SNR model gives a radius of 0.71° at ISM number density of n=0.006 cm^{-3}, which is almost overlapping the TeV gamma-ray emission for HESS J1303-631 in the low ISM density case.

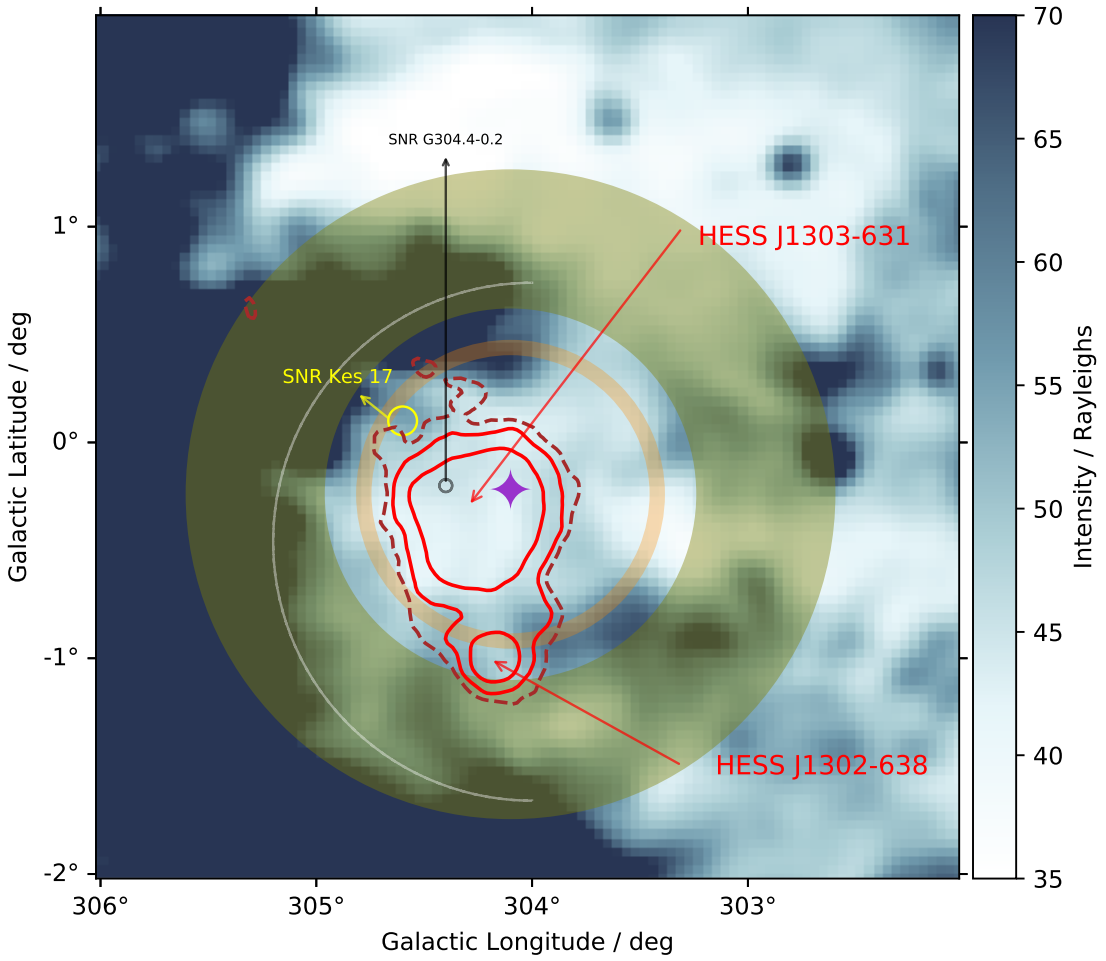

Figure 4.1: Hα image by Finkbeiner (2003) towards the TeV emission. Red contours are for 5σ and 10σ, and the red dashed line is for the 3σ level of HESS J1303-631. The model of the SNR radius is in orange with density of n=0.006 particle per cm^3 is shown. The location of the pulsar is denoted by ✦. The light-green ring is for our SWB model with ISM density 0.1 particle per cm^3 and progenitor stars of spectral types O9 to O2. SNR Kes 17 (yellow) SNR G304.4-0.2 (black circle) locations is shown. The white line indicated the feature in Hα we notice.

SNR G304.6+0.1 (Kes 17) is in the north-east side of HESS J1303-631 and at a distance of 9.7 kpc. However, the separation between Kes 17 and PSR J1301-6305 is around 3 kpc which probably makes them unrelated (Koo et al., 2016). Sushch et al. (2017) suggested a recent SNR G304.4-0.2 candidate which has 36 pc diameter SNR at a distance of 6.6 kpc as an origin for PSR J1301-6305. The diameter for SNR G304.4-

0.2 is way too small compared with the TeV emission which makes both sources unrelated. The SNR model covers SNR candidate, but there is no emission in Hα toward this SNR.

The SWB model, (equation 2.10), has also been applied to HESS J1303-631 using the PSR J1301-6305 location as a progenitor star to search for the effect in ISM around the TeV emission. As for the SNR model, we used the dispersion measure distance of pulsar PSR J1301-6305, but we have assumed a slightly higher ISM density of n=0.1 cm^{-3} due to the avarage ISM density suggseted by Dermer and Powale (2013). Since it overlaps the dense Hα emission to the left the uncertainty in the SWB radius depends critically on the initial spectral type of star. There, we assumed a lower limit of a O9 spectral progenitor star, and a higher limit of O2 spectral type. The SWB model is indicated as light-green ring in Figure 4.1, assuming a distance of 6.6 kpc to the SWB, as per the pulsar distance. The Hα emission void-like feature on the east side suggest a morphology which wraps around the TeV contours of HESS J1303-631 and we note that there is an overlap between the Hα emission and our SWB modelled radius.

The change in the ISM density that we have adopted between the SNR and SWB is due to the SWB shock which decreases the density of the ambient medium around the original system. As a result, the SNR shock will propagate through a lower density medium.

In summary, the morphology of the Hα emission here matches the HESS J1303-631 towards its east, south and north side. This may indicate the presence of the progenitor SWB bubble associated with HESS J1303-631 and PSR J1301-6305.

4.2 HESS J1356-645

HESS J1356-645 will be investigated in term of the noticeable Hα feature (Chapter 3). HESS J1356-645 is known as a PWN (Abramowski et al., 2011), and the optical Hα

image from Finkbeiner (2003) are shown in Figure 4.2. Towards HESS J1356-645, the pulsar PSR J1357-6429 with a spin down power of 3.1×10^{36}erg s^{-1}, will be considered the progenitor star for our SNR model. This pulsar has a distance of 2.4 kpc and characteristic age of τ_c=7.3kyr (Abramowski et al., 2011). This region has no other pulsar with a spin down power $> 10^{34}$ erg s^{-1}. (Shan et al., 2019) used the Red Clump (RC) stars method to determine the distance to the candidate SNR G309.8-2.6 which is suggested to be 2.3$\pm$0.2 kpc. The SNR G309.8-2.6 candidate is at the same direction of HESS J1356-645 and at the same approximated distance. However, the diameter of the SNR G309.8-2.6 candidate is varies from radio 35×15 arc-min to X-ray 1×2 arc-min. Therefore we can not make any further conclusions.

HESS J1356-645 has a likely energetic pulsar lying in the range of the gamma-ray emission, where the orange ring refers to the SNR prediction using the pulsar as the progenitor star. We assumed $\pm$ 0.5 kpc as an uncertainty in distance for the SNR model.

Shown in Figure 4.3, is the high resolution Hα image from Parker et al. (2005). We notice that the Hα arc feature seen in the Finkbeiner (2003) image is clearly resolved. The Hα arc can be noted on the east side of the HESS J1356-645 which lies on the expected SNR model radius. The arc has interesting match with our SNR model the TeV sources is not 'generator'

We created a mosaic of nine different images towards HESS J1356-645 to build a wide field view for the Hα arc feature towards the south east. The arc discussed in Figure 4.2 is clearly shown in high resolution SHS Hα observation. We note that the Hα arc intensity increases as with distance from the TeV emission of HESS 1356-645.

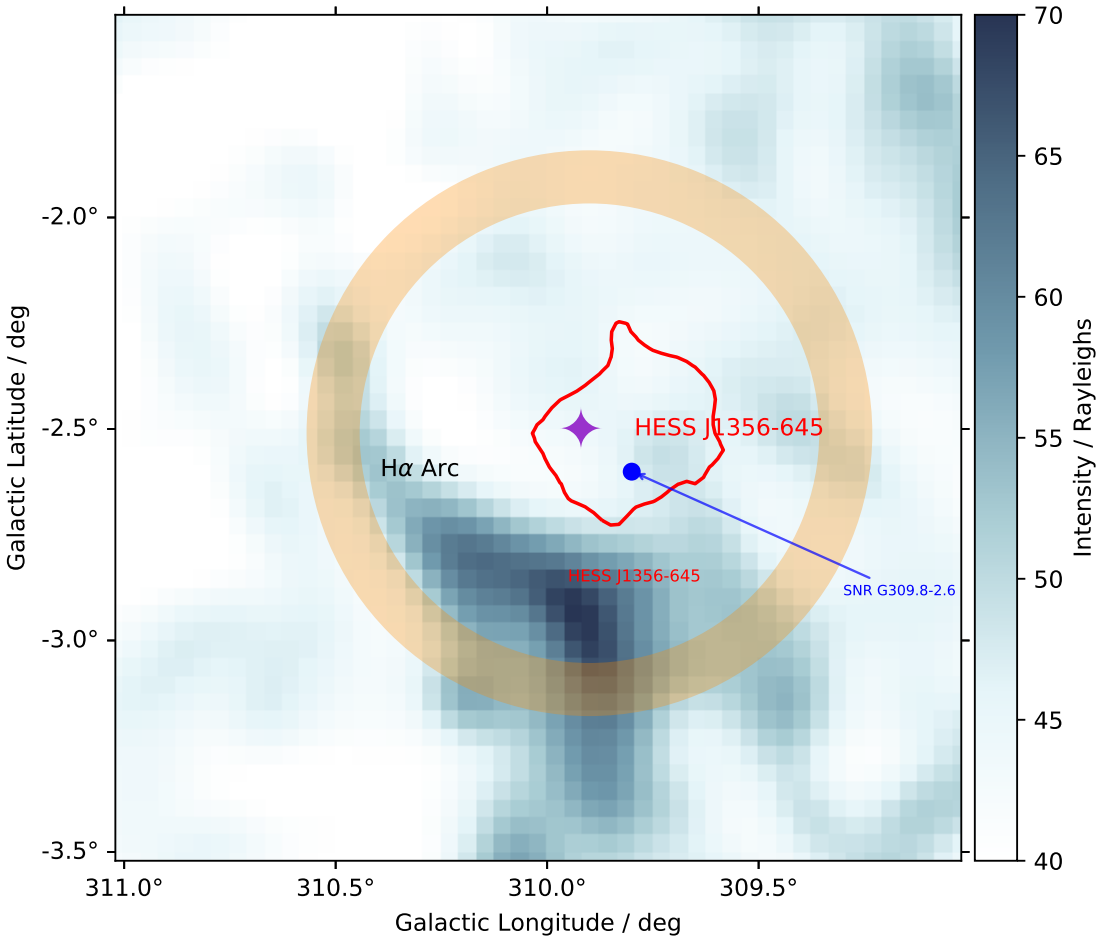

Figure 4.2: Hα image by Finkbeiner (2003) towards the TeV emission with red contour significance of 5σ level. The SNR model is in orange assuming a density of n=0.35 particle per cm^3. The location of the pulsar is denoted by ✦. The SNR candidate G309.8-2.6 locator is denoted (•) (Shan et al., 2019).

We discussed in Chapter 2 a method that reveals the excitation measurement for Hα arc (e.g. SNR) shock. To confirm the arc nature, further spectroscopic observations of the arc are needed. The ratios $[S\,II]/H\alpha$ and $[N\,II]/H\alpha > 0.5$, as assumed in Chapter 2, can suggest that the arcs or filaments were formed by an SNR shock, and it is therefore related to the TeV emission towards HESS J1356-645. Thus, we would suggest new observation of the [S II] and [N II] lines would be very useful.

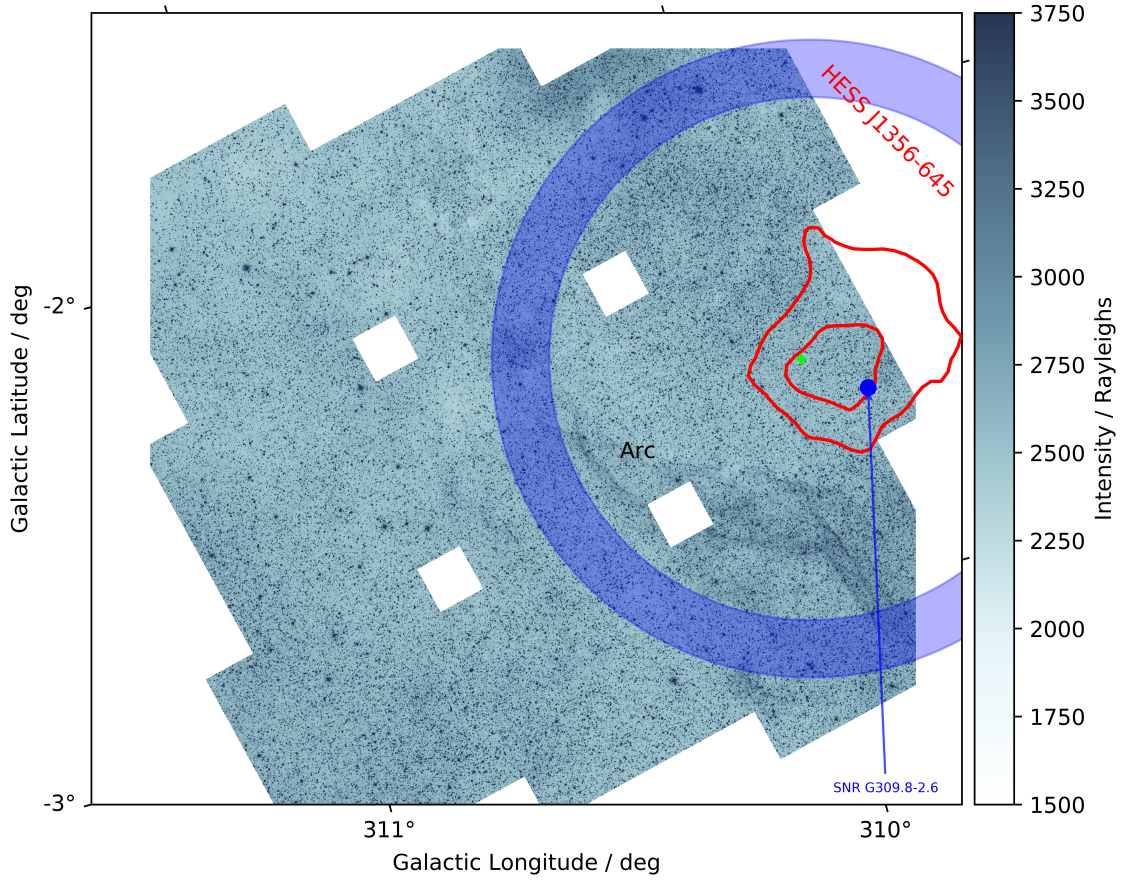

Figure 4.3: Hα image from Parker et al. (2005) towards HESS J1356-645 and the Hα arc. The SNR model assuming an ISM density of 0.1 particle per cm^3 is shown in blue. The pulsar is in green ✦ and the Hα arc almost overlaps with the SNR model toward the south-east. SNR G309.8-2.6 is denoted (•) (Shan et al., 2019). The HESS J1356-645 is shown in red contours(significance of 5σ and 7σ level).

The Sydney University Molonglo Sky Survey (SUMSS) radio survey at 843 MHz with limiting peak brightness at 6 mJy beam^{-1} and signal of 1 mJy beam^{-1} was used (Bock et al., 1999) to further search for signs of any SNR activity. The radio image in Figure 4.4 indicates the possible presence of an arc, at 3 mJy beam^{-1}, about 0.5° from the TeV source, and in the same direction of the Hα arc. Here we investigate the SNR model density that will overlap with the arc shown in the radio observation. We found that an ISM number density of 0.006 particle per cm^3 for the SNR model overlaps with the radio arc as shown in Figure 4.4.

Even though the radio arc emission is close to the noise limit, the morphology at the center of HESS J1356-645 shows a extended structure. Notably, the radio arc emission around HESS J1356-645 may be related to the SNR G309.8-2.6 candidate which agrees with the hypothesis from Kirichenko (2015) that explain the extend radio emission observed.

With this analysis we suggest the radio arc and Hα may indicate the presence of the progenitor SNR associated with PWN HESS J1356-645. Since, the radio arc is rather weak, however, further observation (e.g. with MWA and/or ASKAP) will be needed to confirm its presence.

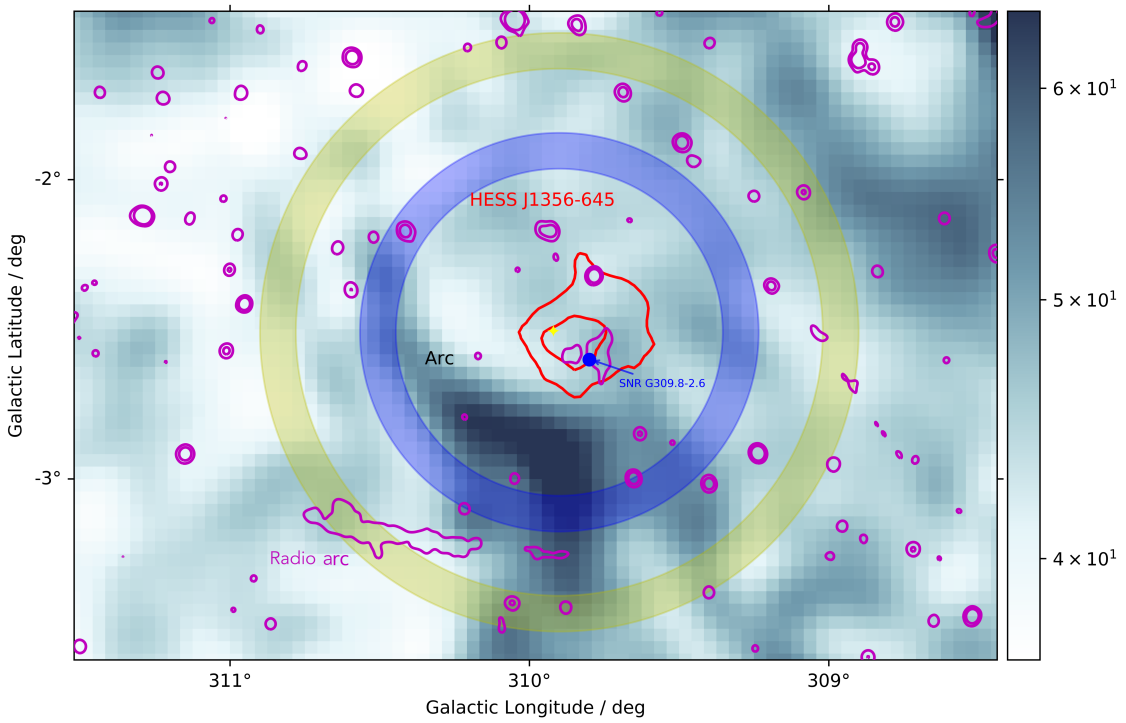

Figure 4.4: Hα image by Finkbeiner (2003) and SUMSS 843 MHz radio (Bock et al., 1999). (purple contours at 10 to 3 mJy beam^{-1}) towards HESS J1356-645. The two SNR models with n=0.1 and n=0.006 particle per cm^3 are applied centred on the pulsar PSR J1357-6429 noted in yellow. SNR G309.8-2.6 is denoted (•) (Shan et al., 2019).

For the SWB model, we used the distance and location of the pulsar PSR J1357-6429 as per the SNR model. Figure 4.5 shows the SWB model with the TeV emission

contours in red (5σ and 10σ). The SWB model for HESS J1356-645 extends over 10° due to the nearby assumed distance to the TeV emission around 2.4 kpc and the assumed ISM number density. Much of the surrounding ISM region overlapping the SWB model is showing a lack of Hα emission. However, on the north-west side the Hα emission overlaps with the SWB model. There is however no obvious morphological connection between the SWB model and the Hα emission, and thus we find no evidence for any such bubble.

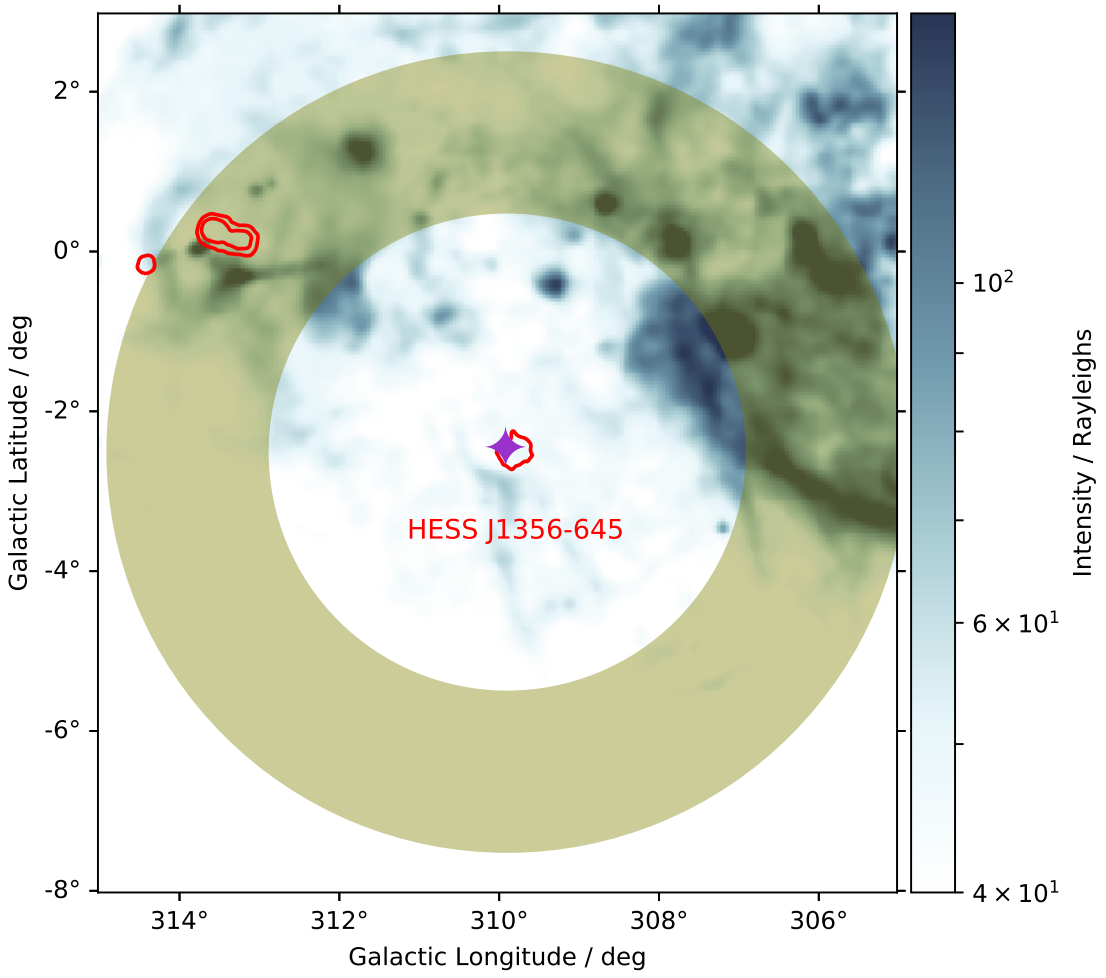

Figure 4.5: Hα image by Finkbeiner (2003) towards HESS J1356-645 (red contours 5σ and 10σ significance). The SWB model is shown in light green assuming a density of n=0.1 particle per cm^3 and O9 to O2 limits on stellar wind luminosity. The location of the pulsar PSR J1357-6429 is denoted by ✦.

4.3 HESS J1640-465 and HESS J1641-463

HESS J1640-465 is classified as a PWN, and it is likely to be related to SNR G338.3-0.0 and the PSR J1640-4631 (Acero et al., 2013; Lau et al., 2017) (see Figure 4.6). The Hα emission towards the south of the source wraps in a way that indicates a related structure to the TeV emission. The measured distance to this pulsar varies between 8.5 kpc (near) and 13 kpc (far) based on HI absorption. For the SNR model towards HESS J1640-465, we used the distance for SNR G338.3-0.0 and location of the PSR J1640-4631. The age of PSR J1640-4631 is around 3 kyr (Gotthelf et al., 2014) and it has a spin down power of 4.4×10^{36}erg s^{-1}. The SNR G338.3-0.0 overlaps the TeV contours of HESS J1640-465, and the distance to the SNR G338.3-0.0 is suggested to be $11.7^{+2.0}_{-0.5}$ kpc (Lau et al., 2017). SNR G338.3-0.0 is likely located in the Norma arm of our galaxy, and there are H II regions located at the same distance (Lau et al., 2017). The study by Oya et al. (2014) towards this region did not reveal the origin of HESS J1640-465 TeV emission.

In Figure 4.6, the SNR model for HESS J1640-465 is shown as the orange ring with a radius 0.22° which has an annulus due to the distance uncertainty of $\pm$1 kpc and assuming a ISM number density of n=0.1 cm^{-3}. The SNR model radius is also in agreement with the real diameter of SNR G338.3-0.0 and overlaps partially with an adjacent SNR G338.5-0.1.

The hadronic model presented by Supan et al. (2016) uses the spectrum of gamma-ray observations from HESS and Fermi-LAT, and concludes that the hadronic model is in a match with the HESS J1640-465 as the initial origin from a SNR. Molecular observations towards HESS J1640-465 and HESS J1641-463 are discussed by Lau et al. (2017), and concludes that the TeV gamma-ray emission from HESS J1640-465 and HESS J1641-463 are due to hadronic interaction due to the dense clouds located and around both sources.

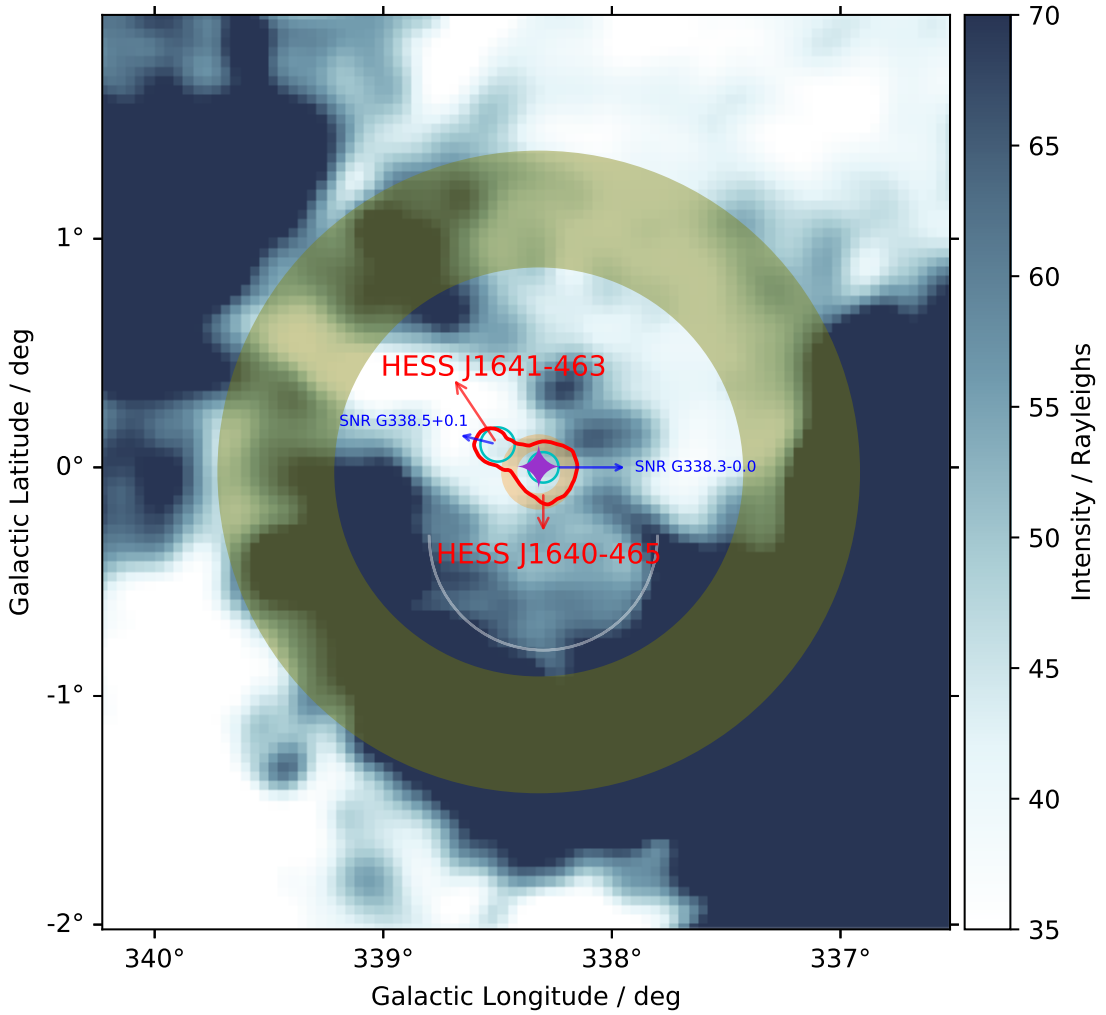

Figure 4.6: Hα image by Finkbeiner (2003) towards the TeV emission of HESS J1640-465 and HESS J1641-463 and the red contour shows a significance level of 5σ. The SNR model in orange assuming a density of n=0.1 particle per cm^3 is shown and it overlaps with the discovered SNR G338.3-0.0 and G338.5+0.1 in cyan by (Green, 2019). The location of the pulsar PSR J1640-4631 is denoted by ✦. The light-green ring shows the SWB model assuming ISM density 0.1 particle per cm^3. The SWB is overlapping the Hα emission in south of the TeV emission. The white arc indicates the interesting Hα feature.

Lau et al. (2017) (using Mopra ^{12}CO(1-0) data) shows a bubble morphology towards SNR G338.5-0.1 (see Figure 3 Lau et al. (2017)). The density in the bubble has not been estimated but it would be much less than the ISM number density n=100 cm^{-3}

assumed by Lau et al. (2017) for the surrounding dense gas. Hence, this evidence of a core collapse SN is presented and SNR G338.5-0.1 would be the origin of HESS J1641-463. There is no currently pulsar believed to be associated with HESS J1641-463. Therefore, we assume that both sources HESS J1641-463 and HESS J1640-465 are related to the same pulsar.

The adjacent TeV source, HESS J1641-463 has a hard gamma-ray photon spectrum with no cut-off sign in the TeV range and a photon index $\sim \Gamma = 2.07$ (Oya et al., 2014). In contrast, observation by Fermi-LAT towards HESS J1641-463 revels a soft GeV spectrum (Lau et al., 2017). The GeV emission could be created by less energetic CRs from the old SNR G338.5-0.1 interacting with the ambient gas, and the TeV emission could be formed by highly energetic > 10 TeV CRs escaping from the nearby young SNR G338.3-0.0 (Lau et al., 2017).

The SWB model is centred at the pulsar location for HESS J1640-465. The limits of the SWB model are stars with spectral type O9 and O2. The SWB model matches the Hα emission toward the south of HESS J1641-463 TeV emission as shown in Figure 3.5 and 4.6.

HESS J1640-465 and HESS J1641-463 are located at a large distance of $\geq$ 8.5 kpc (Lau et al., 2017) which means the Hα features may be in foreground. However, the observable Hα morphological feature towards HESS J1640-465 may be related to SWB of the progenitor star as it is interacting with the ISM surrounding it. The morphology of the Hα indicate a relation between the SWB and the pulsar.

4.4 HESS J1804-216

HESS J1804-216 is an interesting source due to the overlap with both SNR G8.7-0.1 and the 1720 MHz OH maser which indicates a SNR shock and ISM interaction as shown in Figure 4.7. The 1720 MHz OH maser confirms the SNR shock from SNR G8.7-0.1. We have applied the SNR model using the location of the pulsar PSR B1800-

21 (PSR J1803-2137). This pulsar has characteristic age of 16 kyr, is located at a distance of 3.4 kpc and has a spin down power of 2.2×10^{36} erg s^{-1} (Kijak et al., 2016; Manchester et al., 2005b).

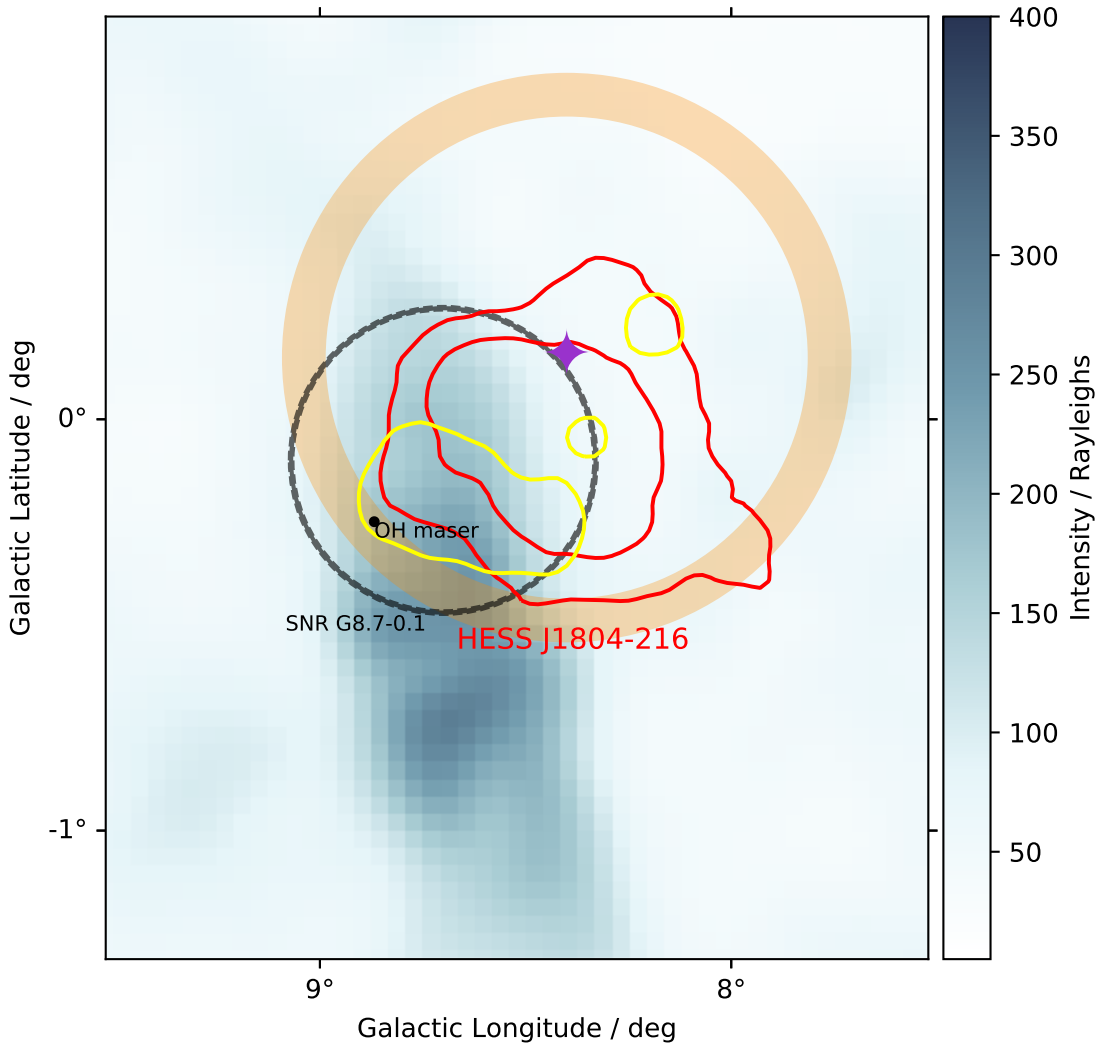

Figure 4.7: Hα image by Finkbeiner (2003) towards HESS J1804-216. (red contours with 5σ and 10σ significance). The SNR model is in orange assuming a density of n=0.35 particle per cm^3. The 1720 MHz OH maser (•) is located towards edge of the SNR G8.7-0.1. The location of PSR B1800-21 is denoted by ✦. The SNR G8.7-0.1 is the black circle. Radio 8.35 GHz contours by Langston et al. (2000) with limits 5-10 Jy beam^{-1} are shown in yellow. H II region G008.153-00.198 is green circle with no distance known yet.

The SNR model shown in Figure 4.7 assumes an uncertainty in distance of $\pm\, 0.5$ kpc based on the dispersion measurement method used to find the pulsar distance. We note that SNR G8.7-0.1 overlaps with most of the TeV emission towards HESS J1804-216, and the SNR model we have applied overlaps with the TeV emission and most of SNR G8.7-0.1. There is strong Hα emission feature running in a north-south direction to the west of HESS J1804-216 Finkbeiner (2003).

We suspect that the region of SNR G8.7-0.1 might be optically active because of the location of the 1720 MHz OH maser, and the intense Hα emission. Therefore, high resolution Hα observations by Parker et al. (2005) were used to further investigate of HESS J1804-216 region and SNR G8.7-0.1 at a fine resolution of 1 to 2 arc-seconds.

Using high 356-645α observations (Figure 4.8), we have found a Hα arc structure that has not been classified as a H II region or an SNR. This arc has an interesting location with respect to our SNR model. Figure 4.8 shows this interesting arc towards HESS J1804-2016 and the SNR model is in orange colour and SNR G8.7-0.1 in grey circle. The location and orientation of the Hα arc matches the edge of SNR G8.7-0.1. The arc's morphology indicates an origin direction toward the TeV emission. Further spectroscopic observations for the arc are needed to show the ratio of $[S\,II]/H\alpha$ and $[N\,II]/H\alpha$ which will test the origin of the arc as due to the excitation by the SNR G8.7-0.1 shock.

The SNR model in Figure 4.7 shows overlaps with most of the TeV emission, SNR G8.7-0.1. The 1720 MHZ OH maser overlaps with the SNR model uncertainty level. The Hα arc displays interesting morphology as well as the region in Figure 4.8 where the dashed line indicates a potential Hα emission region excited by the SNR shock. There is no further evidence for any other Hα shocks toward HESS J1804-2016.

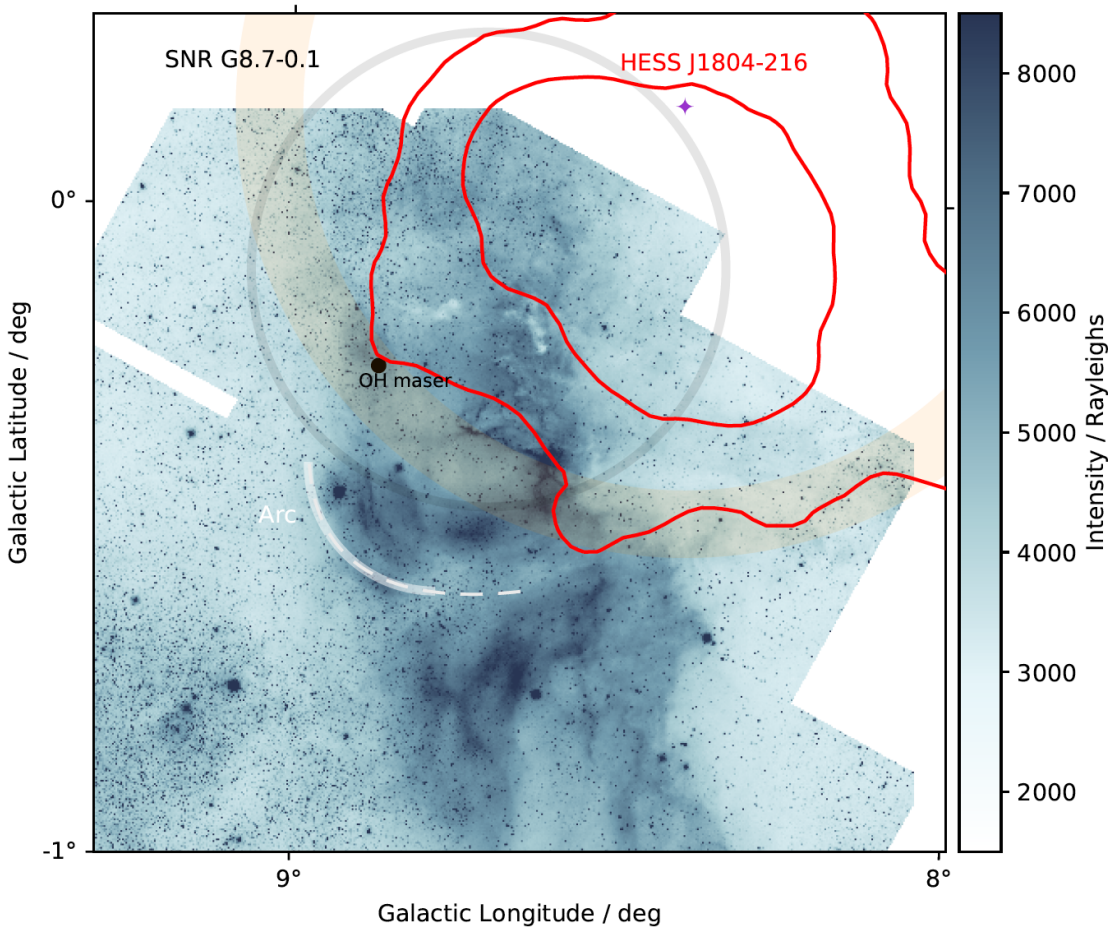

Figure 4.8: Hα image from Parker et al. (2005) SNR G8.7-0.1 in grey circle. HESS J1804-216 red contours (5σ and 10σ) the SNR model is the orange ring. The 1720 MHz OH maser (•) is shown. The location of PSR B1800-21 is denoted by ✦. The white arc indicates the interesting feature in Hα and the dashed line is toward possible extended feature.

For the SWB model, we use the location and distance of PSR B1800-21 as the progenitor. The SWB model is an extended region around HESS J1804-2016, where 3.7° and 2.5° is the radius limits of the SWB model for spectral type star of O2 and O9 respectively. At that range there are no features that show a link to HESS J1804-216 nor to any large scale Hα feature. We will therefore show the SWB model in appendix Figure A.4.

4.5 HESS J1813-178

HESS J1813-178 is very bright, a compact TeV source, and is classified as a PWN (Halpern et al., 2012). PSR J1813-1749 with $\dot{E} = 5.6 \times 10^{37}$ erg s^{-1} at distance 4.8 kpc is associated with HESS J1813-17, and it powers the PWN (Halpern et al., 2012).

The SNR model for HESS J1813-178 shown in Figure 4.9 used PSR J1813-1749 as the progenitor location. The SNR model radius is 0.6° and it is covers the 5σ and 10σ significance gamma-ray emissions contours. We assumed a number density n=0.1 cm^{-3}.

There are two small SNRs, G12.7-0.0 and G12.8-0.0, located towards the center of the TeV emission (Green, 2019). Both SNRs have no age and distance measurement available in the literature. There is some optical Hα emission in the south side, but there are no obvious signs in Hα of any shell or arc in this region. Araya (2018) suggests that the GeV gamma-ray emission toward HESS J1813-178 is from a hadronic scenario and they suggest SNR G12.8-0.0 to be associated to HESS J1813-178. However, this speculation is not conclusive.

Using the PWN/ SNR radius relationship (Van der Swaluw, 2001) $r_{SNR} \sim 4r_{PWN}$ where r is the radius, for HESS J1813-178 we will have an SNR radius of 2.8 pc which is 0.02° in the field of view of Figure 4.9 (Halpern et al., 2012). This is a very small radius compared to the TeV emission at the location of PSR J1813-1749. This SNR radius prediction may be affected by the PWN measurement and the ISM density. Thus, the origin of the TeV gamma-ray emission toward HESS J1813-178 may be a combination of a SNR and a PWN.

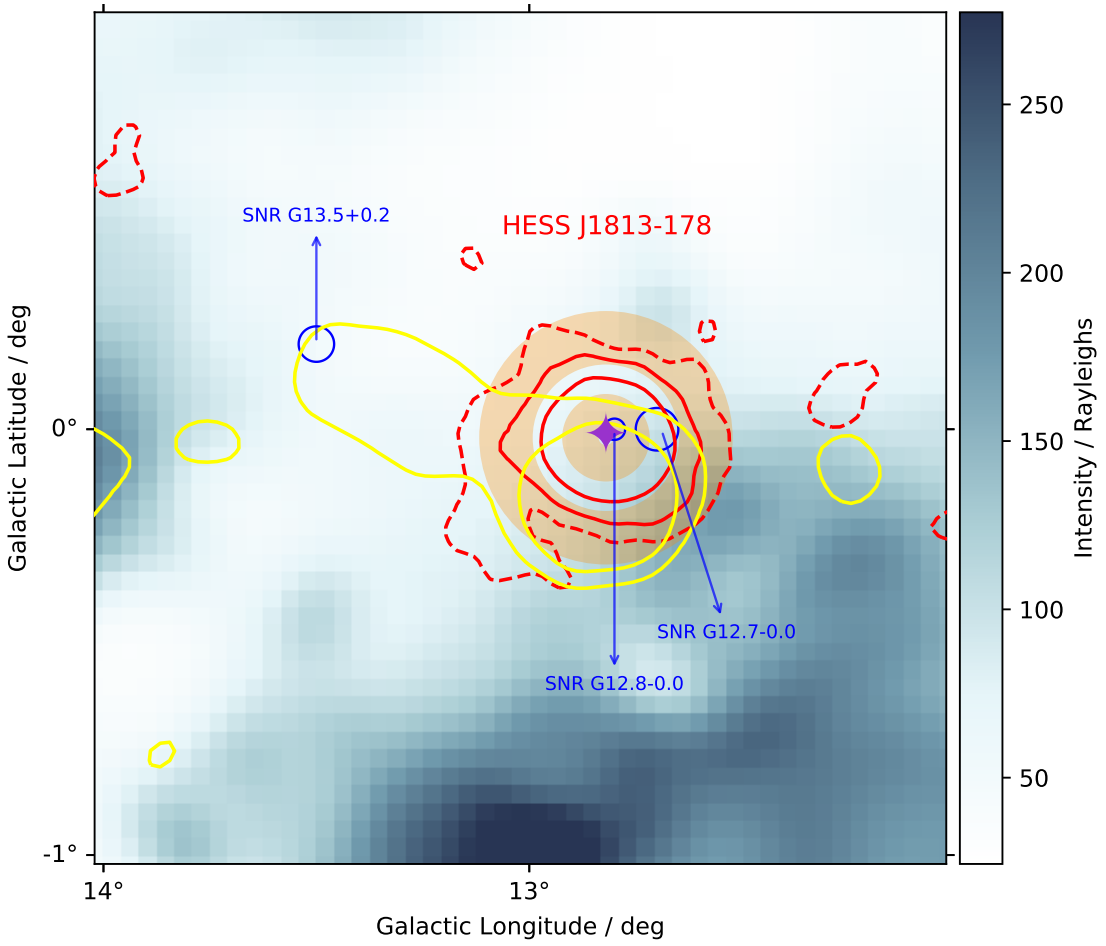

Figure 4.9: Hα image by Finkbeiner (2003) towards HESS J1813-178 (red solid contours 5σ and 10σ) while the dashed red line shows the 3σ level for HESS J1813-178. The SNR model is shown in orange assuming a density of n=0.1 particle per cm^3. The location of the pulsar is denoted by ✦. SNR G13.5+0.2, SNR G12.7-0.0 and SNR G12.8-0.0 are shown in blue near the center of HESS J1812-178. Radio 8.35 GHz contours with 5-10 Jy beam^{-1} are shown in yellow (Langston et al., 2000).

Radio 8.35 GHz emission by Langston et al. (2000) shown in Figure 4.9 overlaps HESS J1813-178 and extends towards the north west to the known SNR G13.5+0.2. This SNR may be not related to HESS J1813-17 given the angular separation $\sim 0.6^\circ$. Lastly, the SNR model towards HESS J1813-178 matches the radio and TeV gamma-ray contains with minimum significance 5σ.

We have also applied the SWB model for HESS J1813-178 using a number density of

0.1 cm^{-3}. The SWB model has a radius of 1.8° and 2.7° for a star with spectral type O9 and O2 respectively. There is no clear correspondence in Hα with the TeV source; therefore, we include it in the appendix Figure A.5.

4.6 HESS J1834-087

HESS J1834-087 is one of the interesting TeV candidates observed by HESS due to the Hα emission arc toward the north of HESS J1834-087 discussed in chapter 3 Figure 4.10. We use the location of the pulsar PSR J1833-0827 as the progenitor of the initial SN, as it argued that it is associated with this source (Misanovic et al., 2011). Noticeably, the pulsar is located outside the TeV contours towards the north. The age of this pulsar has been assumed to be 150 kyr, and it is at a distance of 5.6 kpc, with a spin down power of $\dot{E} = 5.8 \times 10^{35}$ erg s^{-1} (Petroff et al., 2013a; Cordes and Lazio, 2002). Due to the dispersion measurement method used to find the distance, we assumed a distance uncertainty of 0.5 kpc, leading to the annulus shown in Figure 4.10.

The SNR model has a radius of 0.53°, using an ISM number density of 0.1 particle per cm^3. Our SNR model overlaps with most of the TeV emission and also overlap SNR G23.3-0.3 (W41). SNR model does not overlaps with the Hα arc discussed in Chapter 3 and highlighted in Figure 4.10.

Another TeV source HESS J1832-085 is also in the field of the SNR model. HESS J1832-085 is still an unidentified TeV source, but a recent study by Maxted et al. (2019) suggests a relationship between the TeV emission and the SNR candidate G23.11+0.18. The SNR W41 is overlapping almost with the field of view of HESS J1824-087. Leahy et al. (2008) suggested that the distance to SNR G23.3-0.3 (W41) is 3.9-4.5 kpc, based on radio observations. This indicates that it may be related to the TeV emission (Ranasinghe and Leahy, 2018). SNR G22.7-0.2, shown in Figure 4.10, is to the east of HESS J1834-087, and is at a distance of 4.7$\pm$0.2 kpc (Ranasinghe and Leahy, 2018).

It is thought to be not related to the TeV emission of HESS J1832-093 Mori et al. (2017), and the age of this SNR is estimated to be 20 kyr (Stafford et al., 2019). However, SNR G22.7-0.2 and W41 are suggested to have formed from the same giant molecular cloud GMC G23.0−0.4 (Su et al., 2014). The H II region G022.76-0.48 is at a distance of 4.8 kpc and it is suggested to be related to GMC G23.0−0.4 (Su et al., 2014).

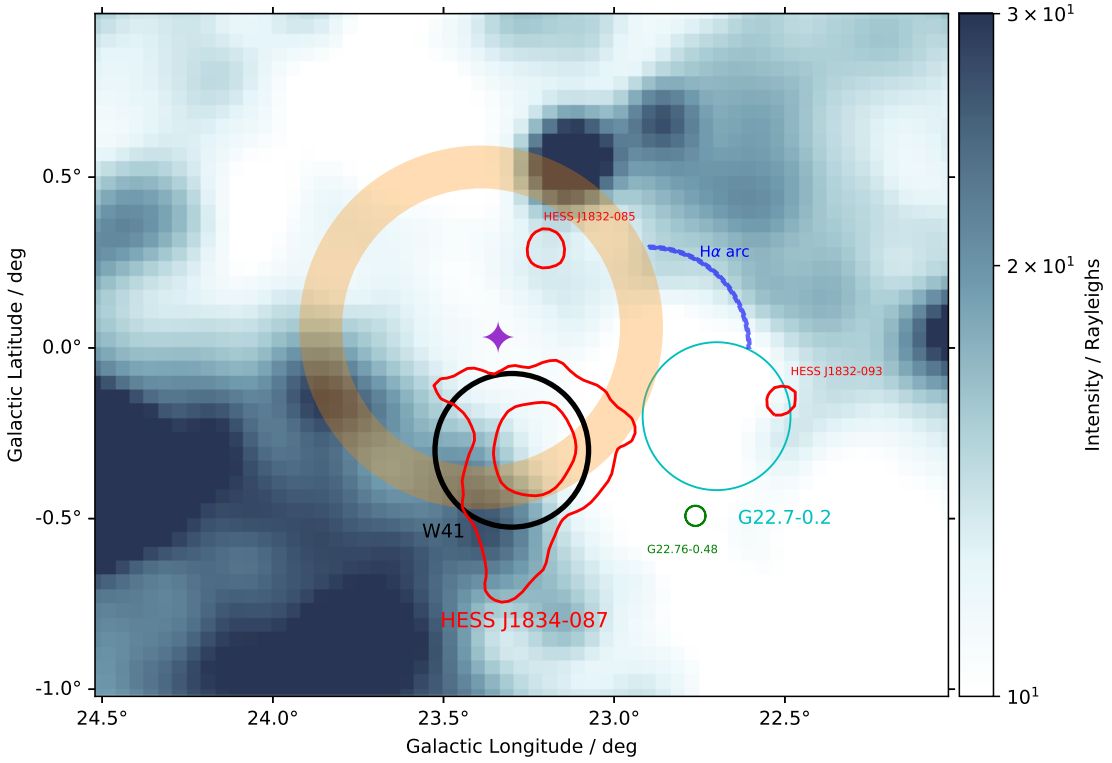

Figure 4.10: Hα image by Finkbeiner (2003) towards the HESS J1834-087 (red contours at the 5σ and 10σ). HESS J1832-085 and HESS J1832-093 are shown with 5σ contour. The SNR model is shown in orange assuming a number density of n=0.1 particle per cm^3. The location of the pulsar PSR J1813-1749 is denoted by ✦. The W41 SNR with radius of 27 arc-min is in black, overlap the TeV emission. The H II region G022.76-0.48 is indicated by a green circle. SNR G22.7-0.2 is indicated is in cyan circle. The Hα suspected arc is in blue.

To summarise, the optical Hα emission towards HESS J1834-087 does not show indication that matches the SNR model. SNR W41 is believed to be associated with

the TeV emission as a hadronic source.

The SWB model for HESS J1834-087 was also applied using a number density 0.1 cm^{-3} and the location and distance of the PSR J1813-1749. However, there is no clear correspondence to arc in Hα. The SWB model has a radius of 2.1° for a star with spectral type O9 and 3.1° for astar with spectral type O2. Therefore, we include it in appendix Figure A.7.

4.7 HESS J1837-069

Next, we consider the region of TeV gamma-ray emission of HESS J1837-069. The Hα emission towards this TeV source in Figure 4.11 shows a lack of emission at the center of HESS J1837-069. This is an interesting TeV source because it contains PSR J1838-0655 which has a high spin down power of 5.5×10^{36} erg s^{-1} and an age of 2.2 kyr and with a distance of 6.6 kpc (Manchester et al., 2005b). The distance to the pulsar is considered to have an uncertainty of $\pm$0.89 kpc (Fujita et al., 2014).

Our SNR model centred at the location of PSR J1838-0655 of HESS J1837-069 has a radius of 0.56°, which is in the field of the gamma-ray radiation defined by the 5σ significance level. The radius of our SNR model and this candidate overlaps with three H II regions: G025.86+0.11 which has a distance of 7.3$\pm$0.9 kpc and a radius of 0.17° Quireza (2006). The H II region G024.8+0.1 is at this region and at a distance of 6.3$\pm$0.6 kpc (Anderson et al., 2014).

In addition, The SNR model also overlaps with SNR G24.7-0.6 which is towards the east and has a distance of 3.8 kpc and a radius of 9.9 pc based on HI absorption and CO studies (Ranasinghe et al., 2018). Another SNR G24.7+0.6 has a diameter of 0.58° (Becker and Helfand, 1987) and it is Crab-like due to its compact morphology in radio (Acero et al., 2016) but it does not overlap with our SNR model.

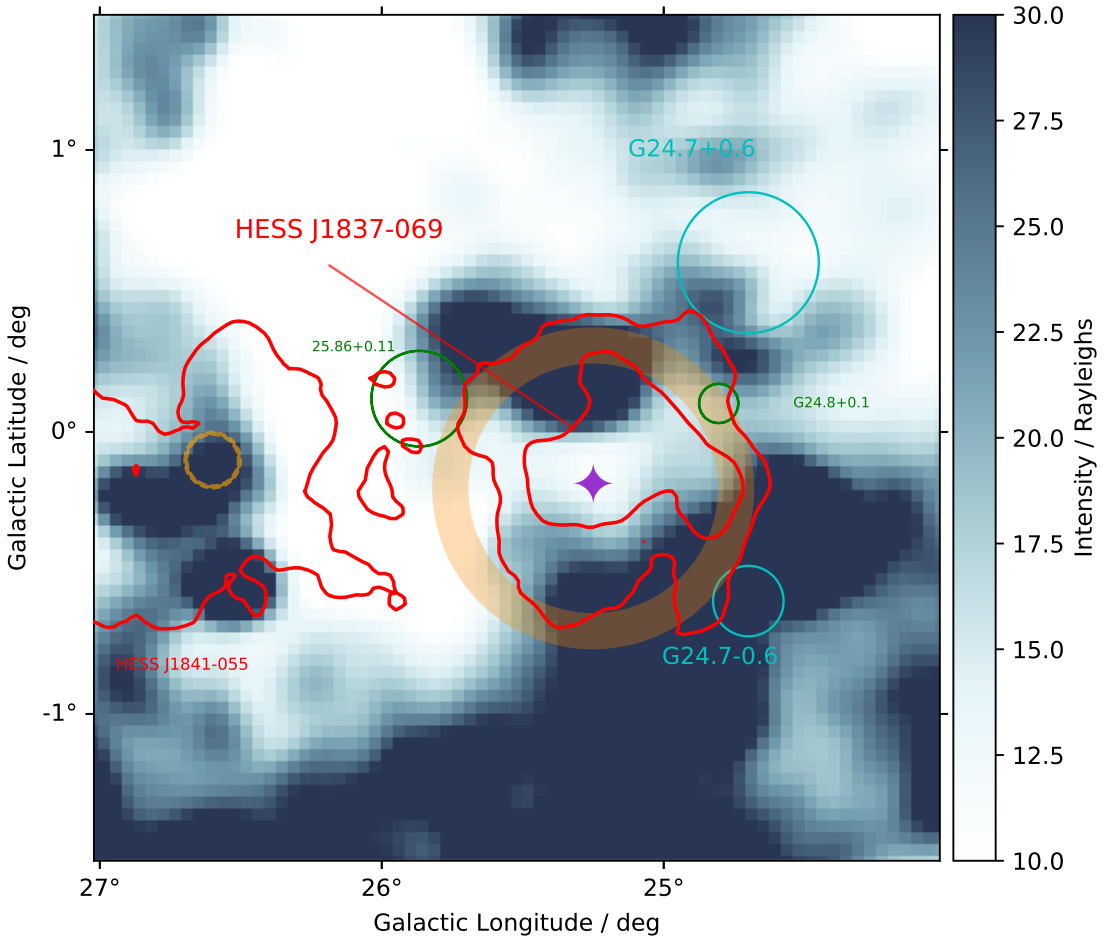

Figure 4.11: Hα image by Finkbeiner (2003) towards HESS J1837-069 (red contours 5σ and 10σ). The SNR model is in orange assuming a density of n=0.1 cm^{-3}. The location of the pulsar PSR J1838-0655 is denoted by ✦. SNR G24.7+0.6 and G24.7-0.6 are indicated as light-blue. The orange circle dashed line the PWN G26.6-0.1 is shown discussed in Chapter 3. The H II region are shown in green circle

In conclusion, the SNR model overlaps with the SNR G24.7-0.6 but due to the distance it is not related to HESS J1837-069. However, SNR model overlaps with the intense Hα emission towards the south. The low resolution Hα observation at this region makes the detection of any morphology hard.

The SWB model for HESS J1837-069 was also applied using a number density 0.1 cm^{-3} and the location and distance of the PSR J1838-0655. However, there are no clear corresponding features in Hα. The SWB model has a radius of 1.2° for a star

with spectral type O9 and 1.9° star with spectral type O2. Therefore, we include it in appendix Figure A.6.

4.8 HESS J1857+026

The most interesting feature towards HESS J1857+026 is the appearance of a ring-like "dip" in Hα that appears to surround HESS J1857+026 (see Figure 3.11). This ring feature may be related to the SN type or the stellar wind bubble created by the progenitor star, which probably contributed to heating of the ambient material to a temperature $> 2 \times 10^4$ K. This will excite the electrons to higher quantum numbers (n>3), as discussed in section 2.3.2, resulting in a lack of Hα emission. PSR J1856+0245 has a spin down power $\dot{E}$ =4.6$\times 10^{36}$ erg s^{-1}, and an age of 21 kyr, and it is located at a distance of 9 kpc (Aleksić et al., 2014).

SNR W44 is found towards HESS J1857+026 and the age of this SNR is $\sim$ 20 kyr with a distance of $\sim$ 3.1 kpc (Clark and Caswell, 1976). There is a 1720 MHz OH maser at the region of the SNR. W44 is prominent in both X-ray and GeV gamma-rays (Hughes and D. J. Helfand, 1985; Cardillo et al., 2014). W44 is clearly not related to the Hα optical band ring due to its location and size compared to this Hα feature. Additionally, SNR G35.6-0.4 is located at a distance of 3.5$\pm$0.4 kpc (Ranasinghe and Leahy, 2018) and is suggested to be related to HESS J1858-020 (Paron et al., 2011).

Our SNR model uses the location and the age of PSR J1856+0245, with ISM number density of n=0.1 cm^{-3}. This gives an SNR radius of 0.4° which overlaps the TeV emission from HESS J1857+026. It also overlaps with the radio 8.35 GHz emission from (Langston et al., 2000) in the east and a Hα emission feature that is also centred on HESS J1857+026 (Figure 4.12).

For our SWB model, we use the distance and location of PSR J1856+0245 and assume an ISM number density of n=0.1 cm^{-3}. Our SWB model shows an overlap with the ring like dip of Hα emission around HESS J1857+026 as shown in Figure 4.12. We suggest

that this dip in Hα may result from the shock front of the SWB or the termination shock of the SWB related to the progenitor star.

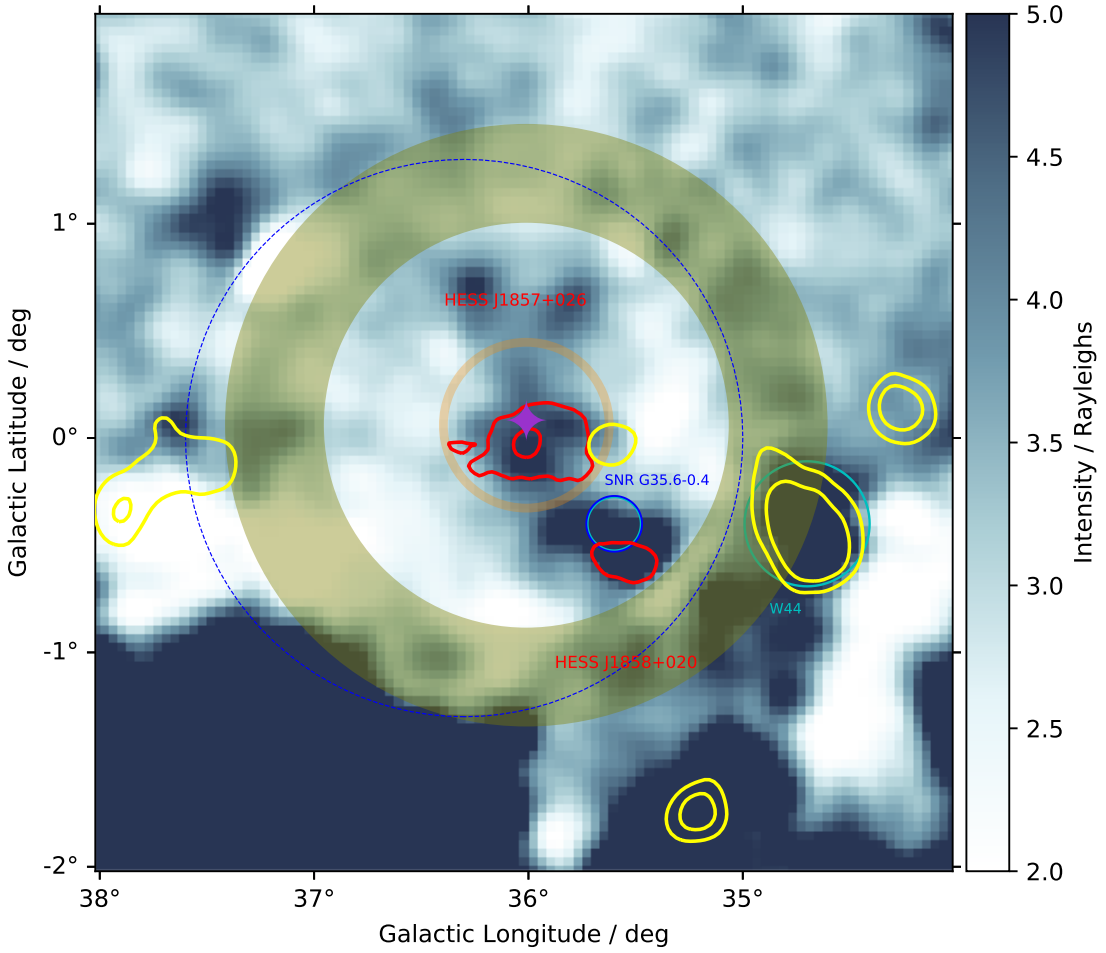

Figure 4.12: Hα image by Finkbeiner (2003) towards HESS J1857+026 (red contour with significance 5σ and 10σ level). The SNR model is in orange assuming a density of n=0.1 particle per cm^3. The location of the pulsar PSR J1856+0245 is denoted by ✦. SNRs are indicated in light-blue. Radio observations by Langston et al. (2000) with contours 5-10 Jy beam^{-1} are shown in yellow. Our SWB model is shown in light green and it overlaps the blue dashed that indicates the ring like dip in Hα emission shown in Figure 3.11. The SNRs G35.6-0.4 and W44 are also shown as cyan circle line.

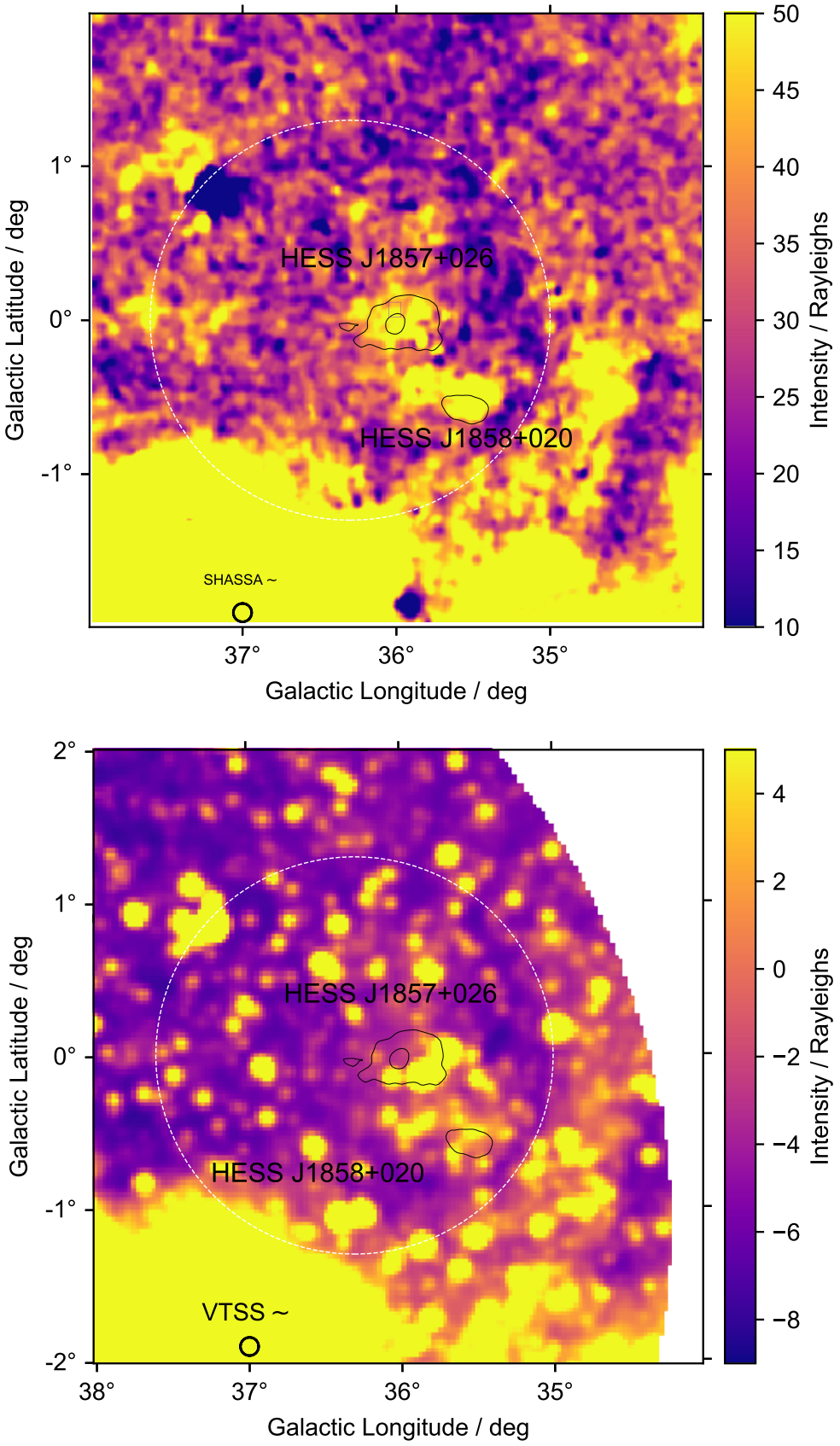

Figure 4.13: Top , Gaustad et al. (2001) SHASSA Hα observation image toward HESS J1857+026 (in black 5σ and 10σ contours). Bottom Figure, Dennison et al. (1998) VTSS Hα image toward HESS J1857+026. The FWHM for each Hα data is shown. The Hα ring like dip feature is shown in a white dashed circle shown in Figure 3.11.

The morphology created by this dip in Hα emission is also observed in two independent optical surveys (VTSS and SHASSA) with an average full width at half maximum (FWHM) of $>$ 2 arc min for VTSS (Dennison et al., 1998) and a FWHM on $\sim$4 arc min for SHASSA (Gaustad et al., 2001) as shown in Figure4.13. This shows that the dip is not related to any systematic effect in the Hα data. One explanation for this dip feature is that the SWB heats up the ISM surrounded HESS J1857+026 to stage where Hα transition could not occur. Unfortunately, the (Parker et al., 2005) 1 to 2 arc second high resolution Hα survey did not cover this region of HESS J1857+026.

4.9 HESS J1912+101

HESS J1912+101 is considered to be a shell-like SNR candidate (Figure 4.14) based on its TeV emission morphology (H.E.S.S. Collaboration, 2018a). Around this region, there are two H II region candidates G45.191-00.486 presented by Anderson et al. (2014) and G45.039–0.643 at a distance of 6$\pm$1.1 kpc (Bania et al., 2012). Figure 4.14 shows HESS J1912-101 and the location of the pulsar PSR J1913+1011 with a spin down power of 2.9×10^{36}erg s^{-1}, a characteristic age of 170 kyr and a distance of 4 kpc.

Studies of the ISM (molecular clouds, atomic gas) in the direction of HESS J1912+101 suggest an old SNR scenario which has an age of (0.7-2.0)$\times$ 10^5 yr (Y. Su et al., 2017). Also, their studies of both CO and H I data suggests that it is a SNR shell type. This result is confirmed by the observation of the 5.0 GHz radio polarization towards HESS 1912+10 (Reich and Sun, 2018). These result suggest give dense ISM surrounding the SNR that may contribute to hadronic TeV emission at this source.

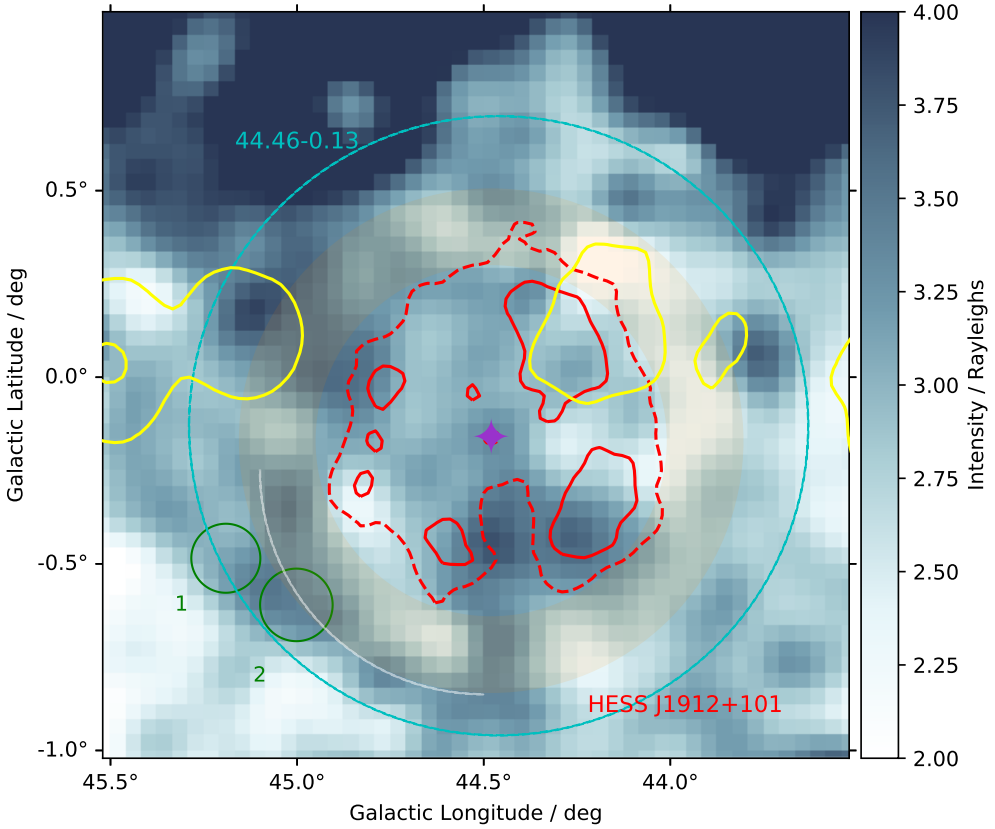

Figure 4.14: Hα image by Finkbeiner (2003) towards HESS J1912-101 (red contours with significance 5σ and red dashed line at 3σ). The SNR model is shown in orange assuming a density of n=6 particle per cm^3. The location of the pulsar PSR J1357-6429 is denoted by ✦. The yellow contours refer to the radio 8.35 GHz emission at 5 and 10 Jy beam^{-1} (Langston et al., 2000). The white arc indicates the interesting Hα emission discussed in Chapter 3. H II regions of interest are in green where (1) is G45.191-00.486 and (2) is G45.039–0.643. SNR candidate G44.6+0.1 in cyan with radius 50 arc min (Reich and Sun, 2018).

Our SNR model used the location and age of PSR J1913+1011 to seek for any interesting features in Hα. We used ISM number density of n=6 cm^{-3} to ensure that our SNR model fits with the observed TeV shell and in the uncertainty range suggested by (Y. Su et al., 2017). The SNR model overlaps with the Hα arc we mentioned in Figure 3.12.

A radio shell SNR (G44.6+0.1) candidate with radius of 50 arc min was later found toward the region of HESS J1912+101 using the Clark Lake Galactic plane survey

(Reich and Sun, 2018). It is possible that the SNR G44.6+0.1 candidate is related to the TeV emission towards HESS J1912+101. The SNR candidate edge overlaps with the interesting arc and H II region (Figure 4.15).

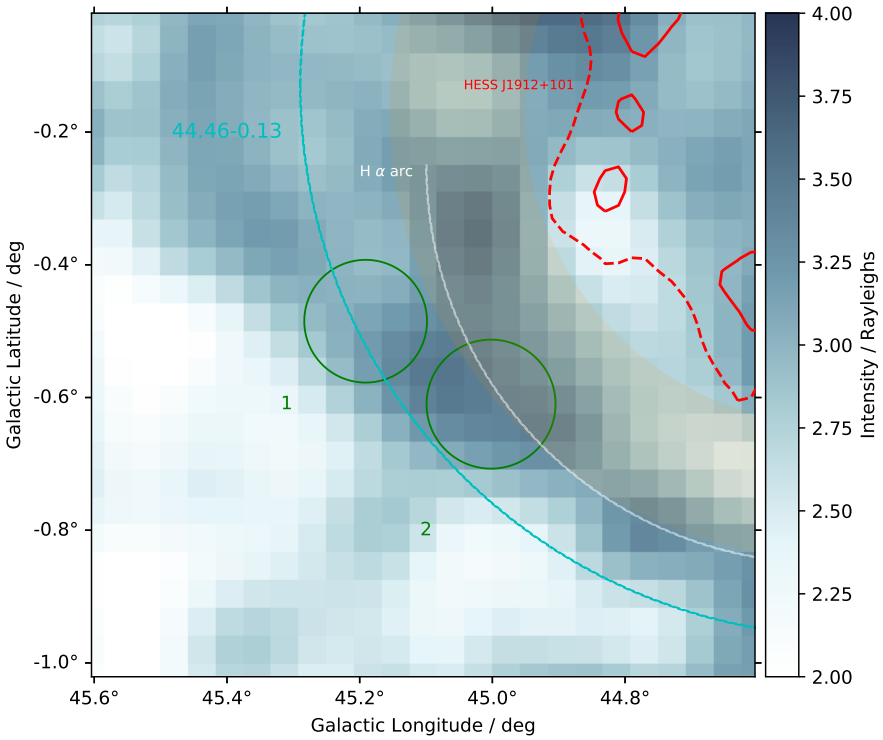

Figure 4.15: Zoom of Hα image from Figure 4.14 towards the interesting Hα region and H II regions G45.191-00.486 and G45.039–0.643 presented by (Anderson et al., 2014). The white line highlight the Hα arc. SNR candidate G44.6+0.1 in cyan with radius 50 arc min (Reich and Sun, 2018).

The H II region G45.002-0.61 (2) in Figure 4.14 and 4.15 has an interesting morphological structure. It has been noted as having an irregular shape (Figure 4.16) by Bania et al. (2012). The morphology of the H II region in Figure 4.16 may show a relationship to the initial SNR of HESS J1912+101, which may influence the morphology of ISM gas. There are no high resolution Hα observations by SHS which would be useful to further study this Hα arc.

NRAO Radio observation with a frequency of 8.35 GHz from Langston et al. (2000) shown two regions in radio that overlap with the Hα emission on the north-west

side of HESS J1912-101. The contour is circular from the radio observations are restricted at 5 and 10 Jy beam^{-1}. However, this area is not classified as an SNR or H II region even though the radio contours radius is $\sim 0.1^{\circ}$. The result in Figure 4.14 shows that H II regions G45.5+0.1 at 9.7 kpc (Zeilik et al., 1975) is not related to the TeV emission due to its distance.

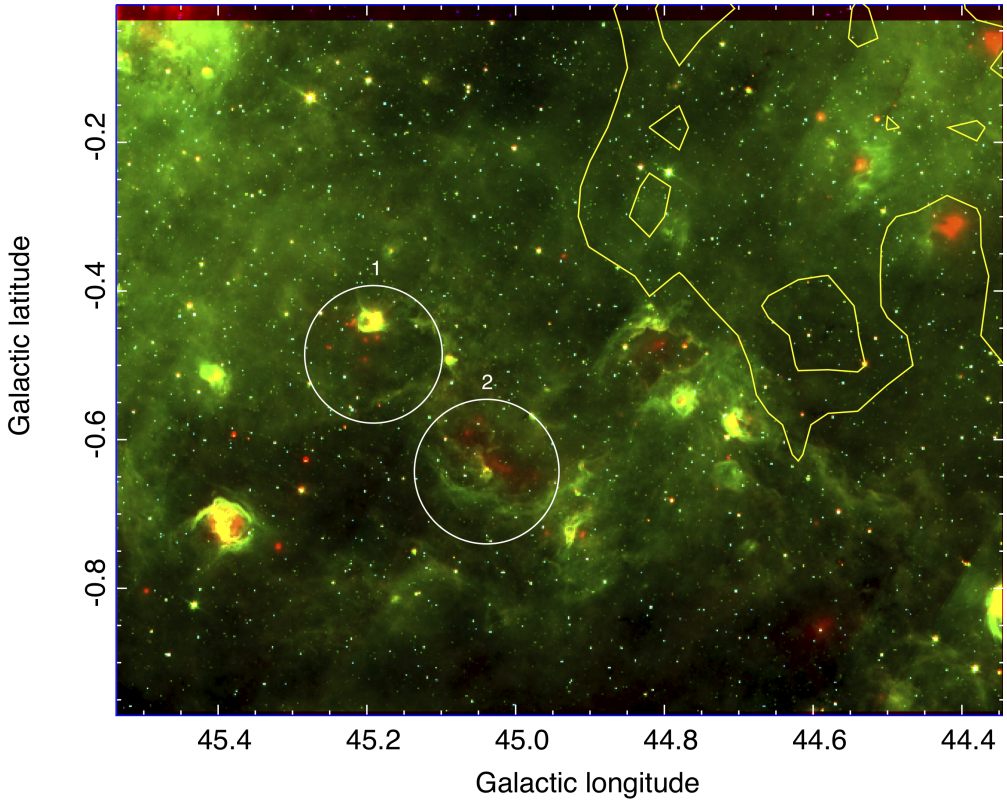

Figure 4.16: Spitzer infrared RGB image from Werner et al. (2004) for the H II region towards HESS J1912+101. The bands of infrared are 24, 8, 3.6 μm with colours red, green, and blue, respectively. H II regions are G45.191-00.486 and G45.039–0.643 presented by (Anderson et al., 2014). HESS J1912+101 TeV contours are in red with significance 3σ and 5σ.

Our SWB model (Figure 4.17) used the distance and location of the pulsar PSR J1913+1011 and an ISM density of 0.1 cm^{-3}. The SWB model predicts an extended ring around the TeV source. The limits of the SWB model is for a star with spectral type of O2 and O9, and the results shows a 3.1° and 2.1° radius for both cases.

The intense Hα emission morphology seems to overlap with the SWB model in the

north and the south directions of HESS J1912-101. This may indicate a cavity created by the the progenitor star.

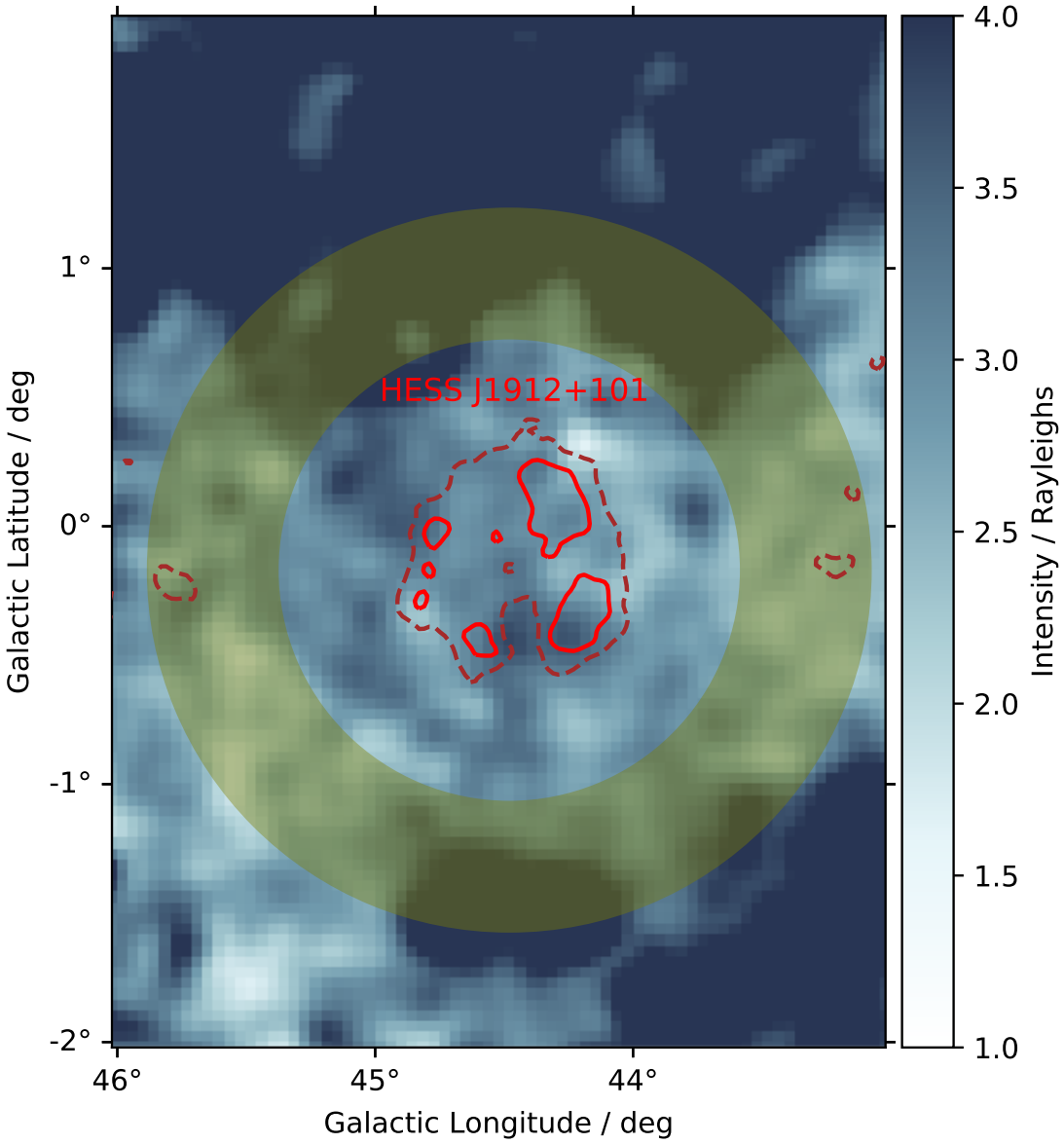

Figure 4.17: Hα image by Finkbeiner (2003) towards HESS J1912-101 in red contours with significance 5σ and the red dashed line is 3σ. The SWB model is shown with light green with ISM density of 0.1 particle per cm^3.

Modelling SNR and SWB shows that the several interesting features in Hα may be associated with HESS J1912+101. The Hα arc overlaps with the SNR model and

two H II regions, one of which is known as G45.039-0.643 and is located within the same distance uncertainty range as PSR J1913+1011. Also, The SNR candidate G44.6+0.1 is almost at the edge of the interesting arc . The SWB model in the north of HESS J1912+101 overlaps an interesting cavity morphology in Hα.

5 Revisiting the HESS 1825-137 Region

The TeV gamma-ray emission observed towards the HESS J1825-137 region is complex and has three prominent regions as discussed in Chapter 3. HESS J1825-137 has been established as a PWN with an associated SNR rim in Hα (Voisin et al., 2016). To the north, HESS J1826-130 is still unidentified, but Voisin et al. (2016) suggest that HESS J1826-130 may be linked to HESS J1825-137 via cosmic rays escaping the progenitor SNR of HESS J1825-137. Also, the nearby powerful pulsar PSR J1826-1256 may contribute to the gamma-ray emission from HESS J1826-130. In addition, a third TeV source is related to the microquasar LS 5039 (HESS J1826-148), and is point-like in morphology (Aharonian et al., 2005a; Aharonian et al., 2006b).
In this chapter, we will further investigate this region seeking for any additional interesting features. Specifically, we will investigate the relationship between Hα in the outflow morphology mentioned in Chapter 3 and any of these HESS sources, using different observations such as X-rays from the Monitor of All-sky X-ray Image (MAXI) (Mihara et al., 2014), Planck radio survey at 545 GHz (Planck Collaboration, 2011), and the Hα survey by Finkbeiner (2003).

5.1 TeV Emission in the Region of HESS J1825-137

The contours of HESS TeV emission towards this region with a significance of 5σ, 10σ, and 50σ are shown in Figure 5.1. The background for the figure is the Hα observation from Finkbeiner (2003). The radio 8.35 GHz contours from Langston et al. (2000) with minimum 5 Jy beam^{-1} are shown in yellow.

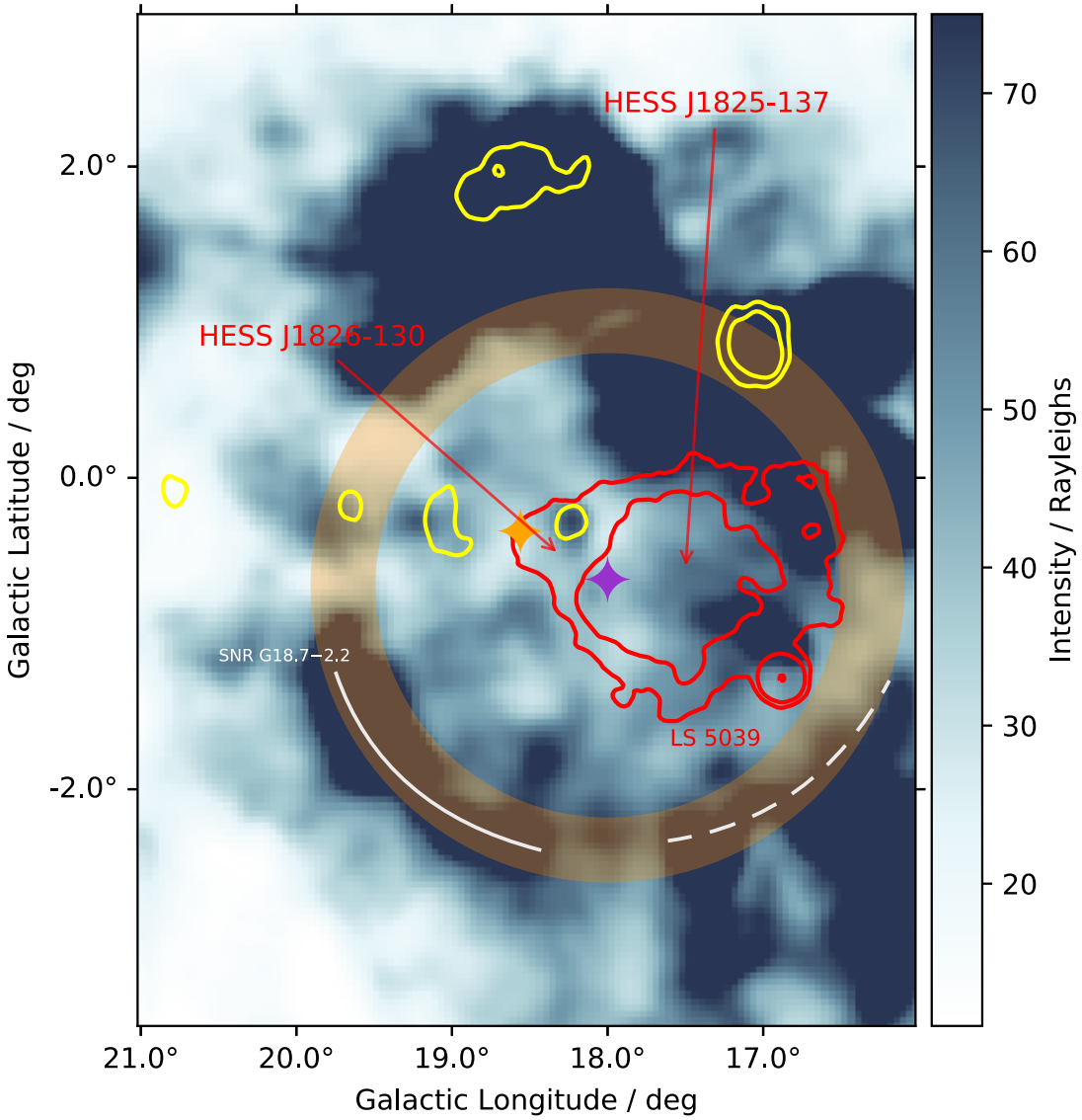

Figure 5.1: Hα image by Finkbeiner (2003) towards the TeV emission (red contours 5σ, 10σ, and 50σ) of HESS J1825-137, HESS 1826-130 and HESS J1826-148. Our SNR model centred on PSR J1826-1334 is shown in orange with density of n=0.006 particle per cm^3. The location of two pulsars PSR J1826-1256 (yellow) and PSR J1826-1334 (purple) is denoted by ✦. The yellow contours are the radio 8.35 GHz survey at 5 and 10 Jy beam^{-1}. SNR candidate G18.7-2.2 is shown and the optical SNR in white solid line (Stupar et al., 2008), and the dashed line is discussed by (Voisin et al., 2016).

First, the TeV PWN HESS J1825-137 is powered by PSR J1826-1334, at a distance of

3.9 ± 0.4 kpc, an age of $\tau_c = 20$ kyr, and a spin down power of $\dot{E} = 2.8 \times 10^{36}$ erg s^{-1} (Figure 5.1). de Jager and Djannati-Ataï (2009) predicted an ISM density of 0.001 cm^{-3} and suggest that by changing the pulsar braking index of the pulsar's spin down power ($\dot{E}$) to 3, the pulsar may be around 40 kyr. This change in the age can affect the model of the SNR spatially for the young SNR. The SNR candidate G18.7-2.2 is in the south-west of HESS J1825-137, and based on a similar SNR radius model that has been used in this thesis as it is likely related to HESS J1825-137 (Voisin et al., 2016). Additionally, the H.E.S.S. Collaboration (2019) suggest that the PWN radius for this source is around 100 pc and is located 4 kpc away. This suggests a SNR with a radius of 400 pc according to the relationship $r_{SNR} \sim 4\, r_{PWN}$ as discussed in chapter 2. However, Voisin et al. (2016) uses a 35 pc radius for HESS J1825-137 PWN and confirmed by the location of the optical SNR rim found by Stupar et al. (2008). Applying the SNR model with ISM number density 0.003 particle per cm^3 indicates that it overlaps with the Hα emission as per Voisin et al. (2016). The SNR model error is the annulus which is due to the 0.5 kpc uncertainty in the distance to PSR J1826-1334.

HESS J1826-130 is on the west side of HESS J1825-137. The PWN G018.5-0.4 is suggested to be associated to HESS J1826-130 and is powered by PSR J1826-1256 which has a spin down power $\dot{E} = 3.6 \times 10^{36}$ erg s^{-1}, an age of 13 kyr, and a distance of 1.7 kpc (Manchester et al., 2005b; Roberts et al., 2007). The origin of HESS J1826-130 emission could be hadronic via cosmic rays from the progenitor SNR of PSR J1826-1334. Voisin et al. (2016) suggest that this hadronic scenario for gamma-rays is plausible due to the proximity of dense molecular clouds towards HESS J1825-137. However, the leptonic scenario can not be entirely neglected, given the powerful pulsar PSR J1826-1256.

The third TeV gamma-ray source to the south east, HESS J1826-148 (LS 5039) is a high mass X-ray binary system at a distance of 2.9$\pm$0.8 kpc (Marcote et al., 2015; Aharonian et al., 2006b). The components of LS 5039 are an O spectral type star

and a compact object which orbits around the O star with a period (P_{orb}) of 3.9 days (Takahashi et al., 2009). The origin of the TeV gamma-ray emission from LS 5039 may be a wind-wind interaction involving a neutron star or a black hole with a sub-relativistic jet (Takahashi et al., 2009). Chang et al. (2016) suggests that the compact object wind and ISM materials collide in this region, and shocked particles accelerated to high energy are generating TeV and X-ray emission. Although the compact object of LS 5039 still unidentified, it has a high mass suggesting that it may be a black hole (Casares et al., 2005). The high mass donor star HD 168075 B, has a spectral type of O7V and a mass of $M_* = 22.9 \pm 3\ M_\odot$ (Casares et al., 2005).

Here, we are mainly interested in the Hα jet-like feature toward the south of LS 5039, HESS J1826-130, and HESS J1825-137 as revealed in Figure 5.2. Here, we can clearly see a blow-out "jet" morphology seen in Hα terminated by a a bow shock structure. The morphology of the bow shock possibly indicates an origin in the direction of the LS 5039 and/or HESS J1825-137.

We have searched the literature and so far the Hα "jet" is not discussed in detail. However, Callaway et al. (2000) discussed the so-called Scutum Supershell GS 018-04+44, at a distance of 3.3 kpc, with diameter of 5°, extending to a b =-11° as shown in Figure 5.3. The Scutum supershell has a similar morphology in both 21 cm H I observation and Hα emission and reveals a low resolution view of the Hα jet. Callaway et al. (2000) suggests that the blow-out in this supershell is generated by multiple SNRs, strong winds from stars with spectral type of O-B, H II regions, or a combination of all these sources powering the outflow. Table 5.1 presents of the Scutum supershell, including its total kinetic energy. Interestingly, this supershell is at the approximate distance of LS 5039, HESS J1826-130, and HESS J1825-137. Also, the H_2O maser G16.86-2.16 is located at a distance of $\sim$ 2 kpc (Kalenskii and Shchurov, 2016). The origin of this H_2O maser is still unidentified but it is suggested to be an outflow related to that (Kalenskii and Shchurov, 2016). However, Callaway et al. (2000) found no solid conclusion for the energetic sources powering the super shell.

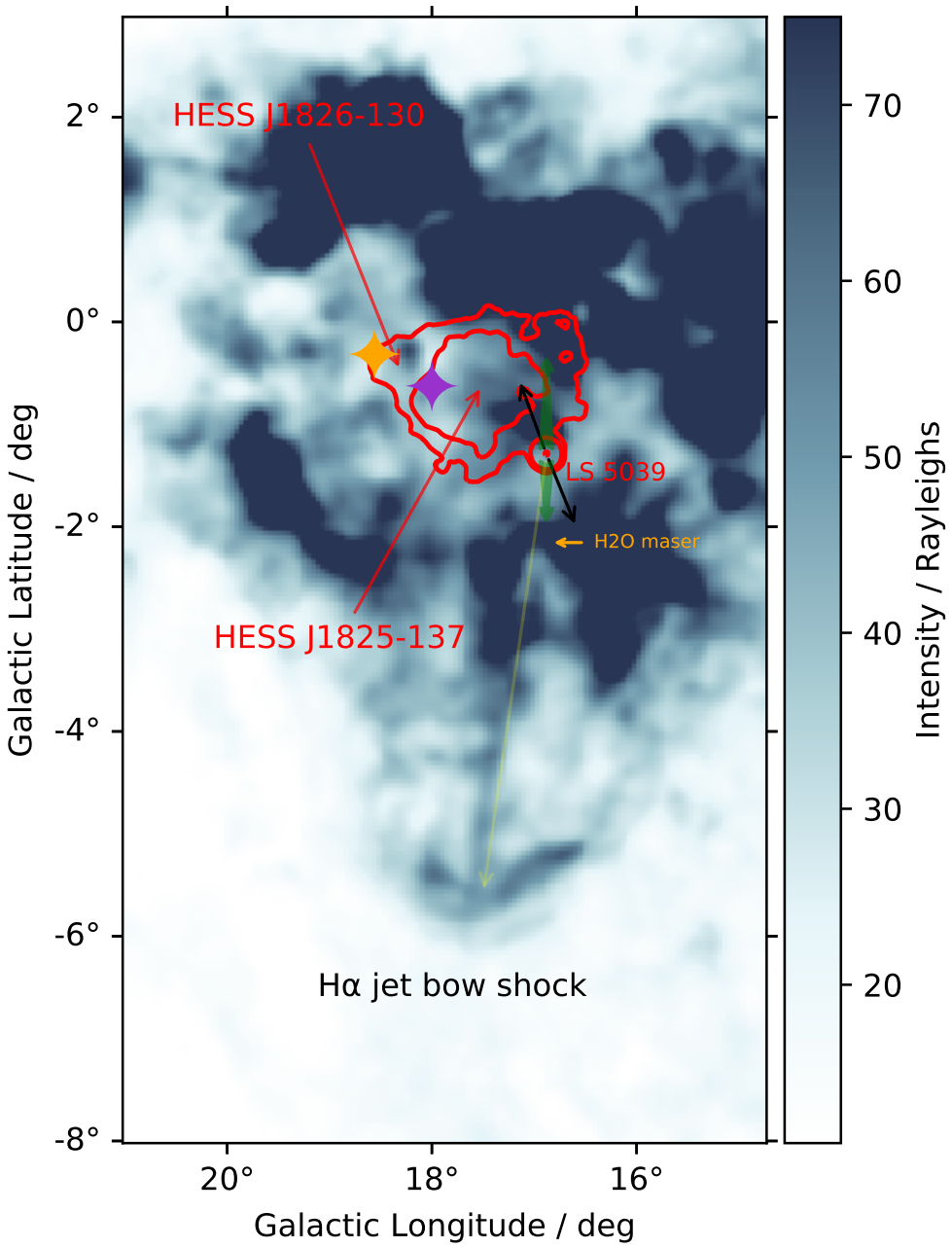

Figure 5.2: Hα image by Finkbeiner (2003) towards LS 5039, HESS J1826-130, and HESS J1825-137 (red contours 5σ, 10σ and 50σ) extended south to highlight the Hα jet and bow shock. The black arrows show the direction of the milliarcsecond radio jets (Paredes, 2002). The green arrows are indicators for the radio structure discussed in Figure 5.6 and the yellow arrow is for the optical Hα. The H2O maser location is noted (Kalenskii and Shchurov, 2016). The location of two pulsars PSR J1826-1256 (yellow) and PSR J1826-1334 (purple) is denoted by ✦.

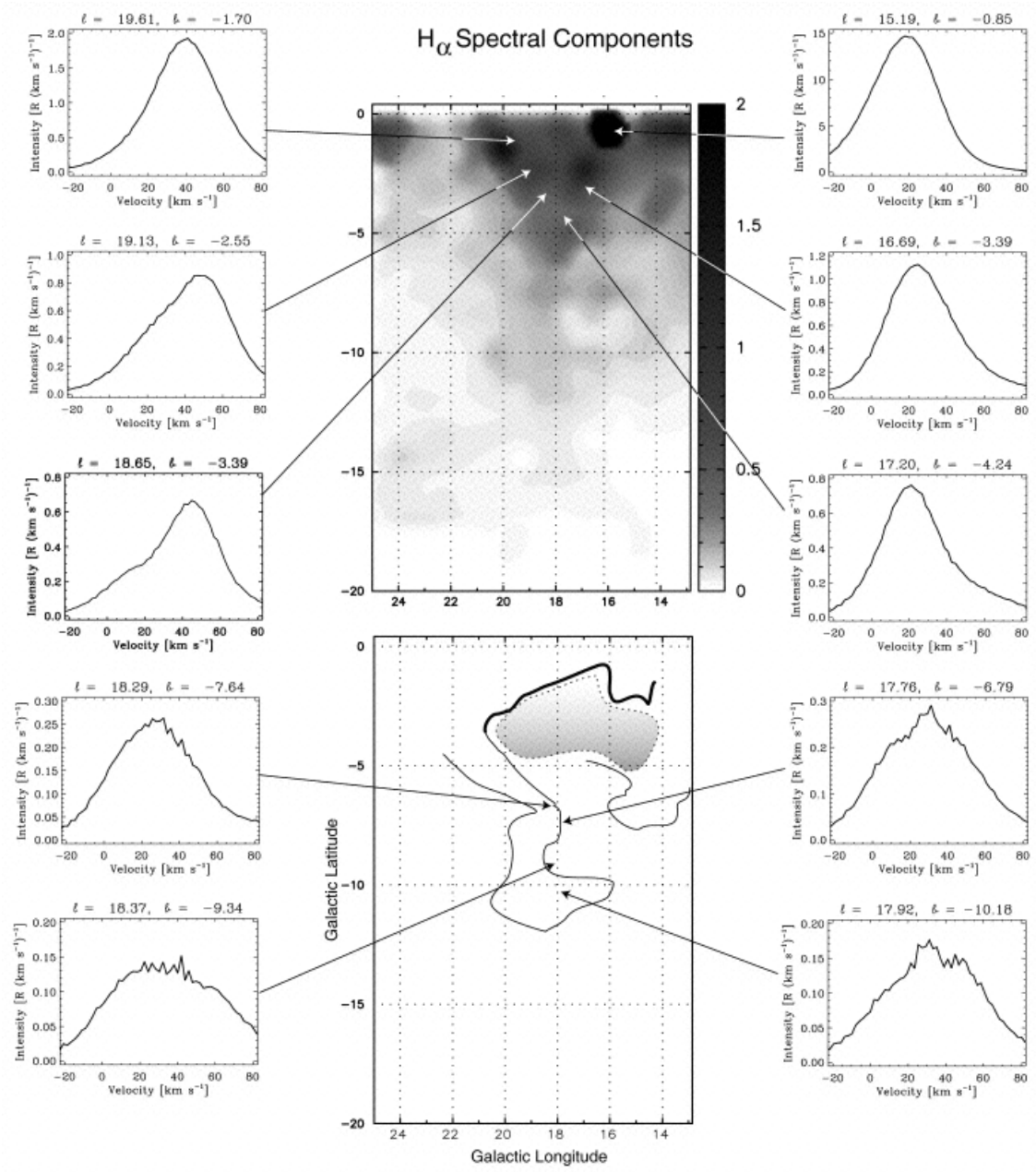

Figure 5.3: (Top) the Scutum Supershell in Hα from WHAM (Callaway et al., 2000). The Hα velocity for each region is in separate panels. (Bottom) HI contours for the Scutum Supershell with additional Hα velocity panels (Callaway et al., 2000).

Scutum Supershell	
Kinematic distance	3.3 (kpc)
Diameter	290 (pc)
Volume	6.2 $\times 10^6$ (pc^3)
H I column	3.6 $\times 10^{20}$ (cm^{-2})
H I density	4.05 (cm^{-3})
Mass	6.20 $\times 10^5$ (M$_\odot$)
Total energy	1.14 $\times 10^{52}$ (ergs)
L_{X-ray}	$\sim$5 $\times 10^{36}$ (ergs s^{-1})

Table 5.1: This Details for the Scutum Supershell from Callaway et al. (2000).

Callaway et al. (2000) in fact mention the existence of blow-out "jet" in the WHAM Hα observations and suggests a distance of 3-4 kpc. However, the WHAM low resolution of 1° was not sufficient to determine the precise direction and the origin of the jet recall that Figure 5.2 shows the Hα jet morphology and its direction quite clearly and the origin of this massive physical structure is still unidentified. This jet has extended to cover almost 4° which no doubt requires an energetic source or multiple sources.

5.2 Jets and Outflows

Astrophysical jet outflows are linear structures that can be collimated over huge distances raging from solar system scales to mega parsecs depending on their origin. Jets usually occur when matter is accelerated to high speed (i.e. much faster than the speed of sound in the local medium), which makes jets very powerful in terms of luminosity and radiation signatures. The majority of astrophysical jets appear to be powered by an accretion disk (J. H. Beall, 2003). There are different types of objects that can create jets, such as extragalactic active galactic nuclei (AGN), quasars, in the Milky Way, microquasars, neutron stars, black holes, young stellar objects, and pulsars. Extragalactic jets can extend mega parsecs in length, while jets within the Milky Way are much shorter, sub-parsec to many parsecs. Micro-quasars generate

the longest jets in the Milky Way, which can reach a hundreds of parsecs. Some jets are bi-polar structured, but on some occasions, only a one-sided jet is visible (Beall, 2014).

There are a number of microquasars[1] which are associated with jets. For example, 1E 1740.7-2942 is a bipolar microquasar at a distance of 12 kpc with jets of length of 1.5 pc and a velocity of around $\sim 75\%$ the speed of light (Luque-Escamilla et al., 2015). GRS 1915+105 is a microquasar discovered by Rosolowsky (2017) using X-ray and radio observations, and was found to be located at a distance of 8.6 kpc with jet lengths of $\sim$ 40 pc from the center. SS 433 is located at a distance of 5.5 kpc towards the SNR W50 (Rosolowsky, 2017). The jets of SS 433 are one of the longest jets so far seen in our galaxy at 80 pc in X-ray and possibly three times the X-ray length based on ^{12}CO observation (Yamamoto et al., 2008).

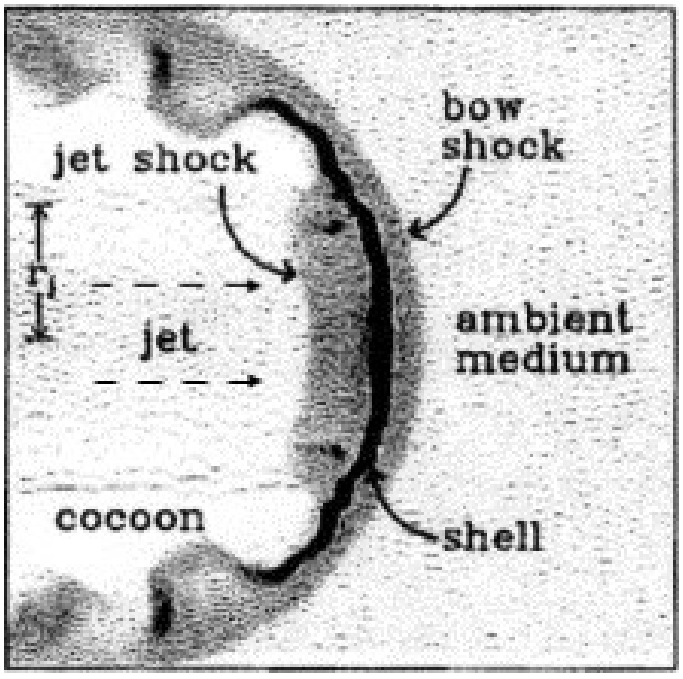

Figure 5.4: The jet direction is indicated by a dashed line and jet structure is shown as the bow shock and the cocoon, as well as the interaction with the ambient ISM (de Gouveia Dal Pino, 2005).

[1] X-ray binary systems launch and collimate jets.

Figure 5.4 shows the basic structure of a jet's bow-shock which is where the streamed material in the jets interacts with the ISM material i.e. the pressure of the jet equals the pressure of the ambient medium (de Gouveia Dal Pino, 2005). The bow-shock generated by jets interacts with the ISM and forms a plasma in the termination shock. The shocked gas flows back towards the side of the jet and forms a cocoon of heated gas. Bow shocks are seen in many astronomical sources such as SNRs, stellar winds by O-B and WR stars, pulsars and in microquasar jets. As far as we know, no previous research has investigated in-detail the bow shock discussed earlier in this chapter observed in Hα.

5.3 H alpha Jets

The detection of jets in the optical band especially in Hα is possible. Since, we know that for the optical line transition the gas temperature should be less than $\sim 2 \times 10^4$K. Panferov et al. (1993) investigated the jets towards SS 433 in various Balmer lines including Hα. They state that the front side of the gas is brighter in the Hα line. Also, the red-shift and blue-shift in both jets shows a pattern where the foreside shock is blue shifted and the backside shock is red shifted.

We first discuss the Hα jet's origin in terms of HESS J1825-137 and the possibility it is related to the pulsar PSR J1826-1334. As the pulsar is located at a distance of ~ 4 kpc, the jet's length is approximately 600 pc. However, pulsar jets such as that for the Crab pulsar and Vela pulsar (seen in X-rays) are much smaller at around 0.15 pc so it is inconceivable that this jet is related to PSR J1826-1256 or PSR J1826-1334. PSR J1826-1334 is located at a distance of 4 kpc with an age of 20 kyr. There is $\sim 1^\circ$ separation between the pulsar and the origin direction of the Hα jet. If they are connected this will make the proper motion for this pulsar suggested by (Pavlov et al., 2008) 400 km s^{-1} larger by factor of 10. The proper motion of PSR J1826-1256 is not discussed, but it is located at least 1° from the jet extrapolation (see Figure 5.5).

This will make the distance to possible origin direction of the Hα jet 30 pc. The age of PSR J1826-1256 suggests the proper motion is $\sim$ 2200 km s^{-1}. For the current work, it is sufficient to point out that the alignment makes this pulsar implausible origin for such a jet.

The velocity for the system LS 5039 is 150 km s^{-1} (Ribó et al., 2002). Tracing back to its origin suggested by (Pavlov et al., 2008) gives us an age of 200 kyr. This makes LS 5039 an old source according to the life of gamma-ray binary systems, which is consistent with a previous estimate for the age of microquasars $\sim$ 100 kyr (Dubus, 2013). Also, McSwain et al. (2004) proposed that the age is less than that suggested by (Ribó et al., 2002) which is 1 Myr.

Figure 5.5 shows the origin birth place for both PSR J1826-1334 and LS 5039, tracing back in time using their proper motion. The possibility of the progenitor supernova of PSR J1826-1334 creating the jet decreases considerably given the large distance towards the jet axis extrapolation. Interestingly however the LS 5039 birth place lines up considerably well with the Hα jet axis in what could be LGRB scenario.

The Hα jet generally points back towards the microquasar LS 5039 as seen in Figure 5.2. Using the minimum distance of 2.5 kpc LS 5039 and assuming that it is the generator of this jet, the length of the Hα jet will be around 187 pc. This is in fact very similar to the length of the SS 433 jets. There are several observations of LS 5039 jets revealing, such as those by the Multi-Element Radio Linked Interferometer Network (MERLIN) and the European VLBI Network (EVN) (Paredes, 2002). They found radio jets with lengths in the order of milliarcsecond (mas) as shown in Table 5.2. As the length of these radio jets are in milliarcsecond, we indicate these jets in Figure 5.2 as black arrows. The alignment of both radio 5 GHz jets and the Hα jets can be related to the curvature which can happen due to the orbital motion and stellar wind in microquasar as shown in (Molina and Bosch-Ramon, 2018). Both radio jets result from recent activity but the Hα jets are not related due to that the Hα jet is likely to be related to much earlier activity from LS 5039, including, potentially, its

progenitor supernova.

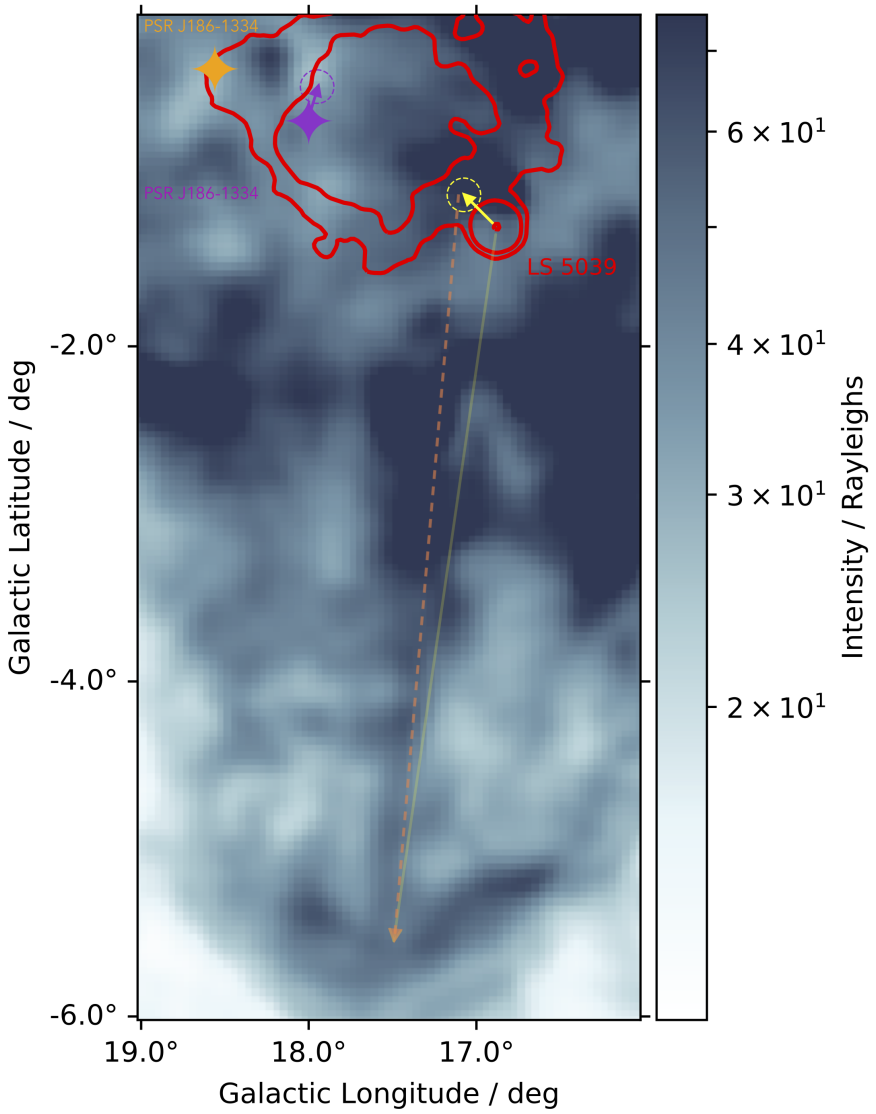

Figure 5.5: Hα image by Finkbeiner (2003) towards LS 5039, HESS J1826-130, and HESS J1825-137 (red contours 5σ, 10σ and 50σ) extended south to highlight the Hα jet and bow shock. The location of two pulsars PSR J1826-1256 (yellow) and PSR J1826-1334 (purple) is denoted by ✦. The dashed circles are the suspected origin of both PSR J1826-1334 and LS 5039. The arrows are indicate the proper motion direction of the sources, going back in time. The dashed orange arrow indicated the jet possibility to be originated for the progenitor supernova of LS 5039 while the yellow line is from the microquasar LS 5039.

	EVN				MERLIN			
	$S_{5\,GHz}$ [mJy]$\pm$0.1	Length [mas]$\pm$2	Length pc	P.A. [°]$\pm$4°	$S_{5\,GHz}$ [mJy]	Length [mas]$\pm$12	Length pc	P.A. [°]$\pm$5°
Core	29.3	—		—	31.6	—		
NW jet	2.6	24	2.5×10^{-3}	−42	4.0	128	1.3×10^{-2}	−29
SE jet	3.3	34	3.6×10^{-3}	140	4.2	174	2×10^{-2}	150

Table 5.2: Jets from 5 GHz radio observations (EVN and MERLIN) towards LS 5039 (Paredes, 2002), where P.A. is the position angle for the jet relative to north.

5.4 Multi Wavelength Search towards the TeV source LS 5039

As discussed previously, astrophysical jets can be detected in many different wavelengths. Therefore, we investigate a range of available public data to enhance our understanding of this Hα jet. We noticed that there are morphologies that agree with the optical Hα jet. We found that besides the HI observation of the Scutum supershell there are radio (Figure 5.6) and X-ray (Figure 5.7) features that may be related to the TeV source LS 5039.

We found a feature in the Planck radio survey data Planck Collaboration (2011) covering frequencies from 30 to 857 GHz (a spatial resolution from about 33 to 4.2 arc-min). Using the high frequency instrument (HFI) in the Planck survey at 545 GHz a clear bipolar outflow structure can be seen as shown in Figure 5.6. This feature is also observed in other (HFI) Planck survey bands (see Appendix A.3). Also, there is H_2O maser G16.86-2.16 located at a distance of $\sim$ 2 kpc is linked to the star formation region (L379IRS1) (Kalenskii and Shchurov, 2016). This maser is believed to result from an outflow coming from the north direction (Taniguchi et al., 2018).

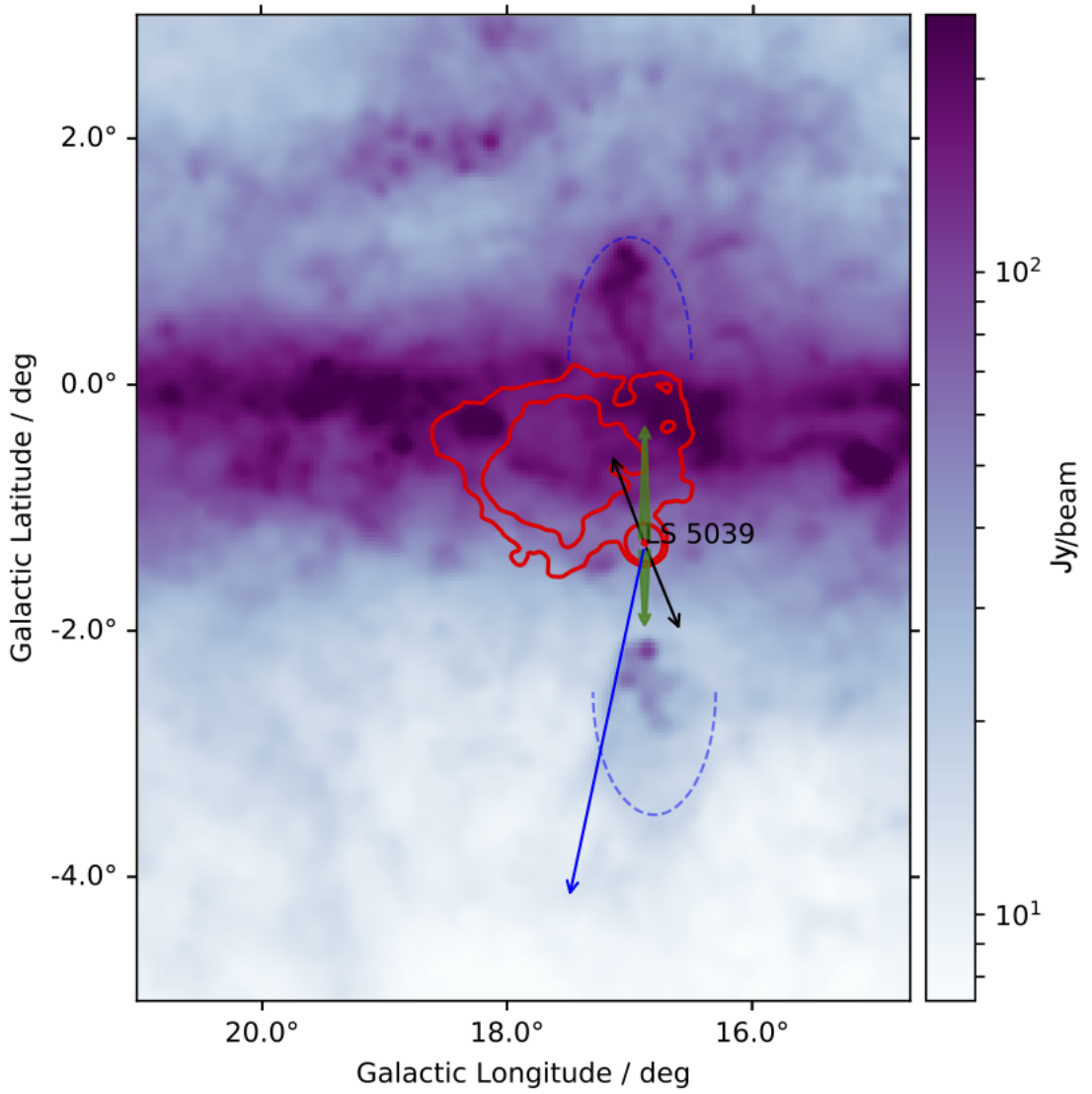

Figure 5.6: Planck Radio 545 GHz image Planck Collaboration (2011) for the region of LS 5039 showing a blow-out structure in two directions. Red contours are for the 5σ, 10σ, and 50σ TeV gamma-ray emission HESS J1825-137, HESS 1826-130 and HESS J1826-148 from HESS. Green arrows show the direction for the jets matching the Planck features. The blue arrow indicates the Hα jet and the X-ray extended feature. The black arrows show the direction of the milliarcsecond radio jets (Paredes, 2002). The H2O maser location is noted (Kalenskii and Shchurov, 2016).

The outflows appears on both sides of the north and south direction along with LS 5039 (Figure 5.6). Both sides are very well aligned with LS 5039 and the distance

between both edges is almost $\sim 4.6^{\circ}$ with LS 5039 located in the middle. These features do not align with the milliarcsecond radio jet nor the Hα jet. LS 5039 at a lower distance 2.1 estimation, suggests that the jet outflow from LS 5039 may be a contribution and it create the H_2O maser.

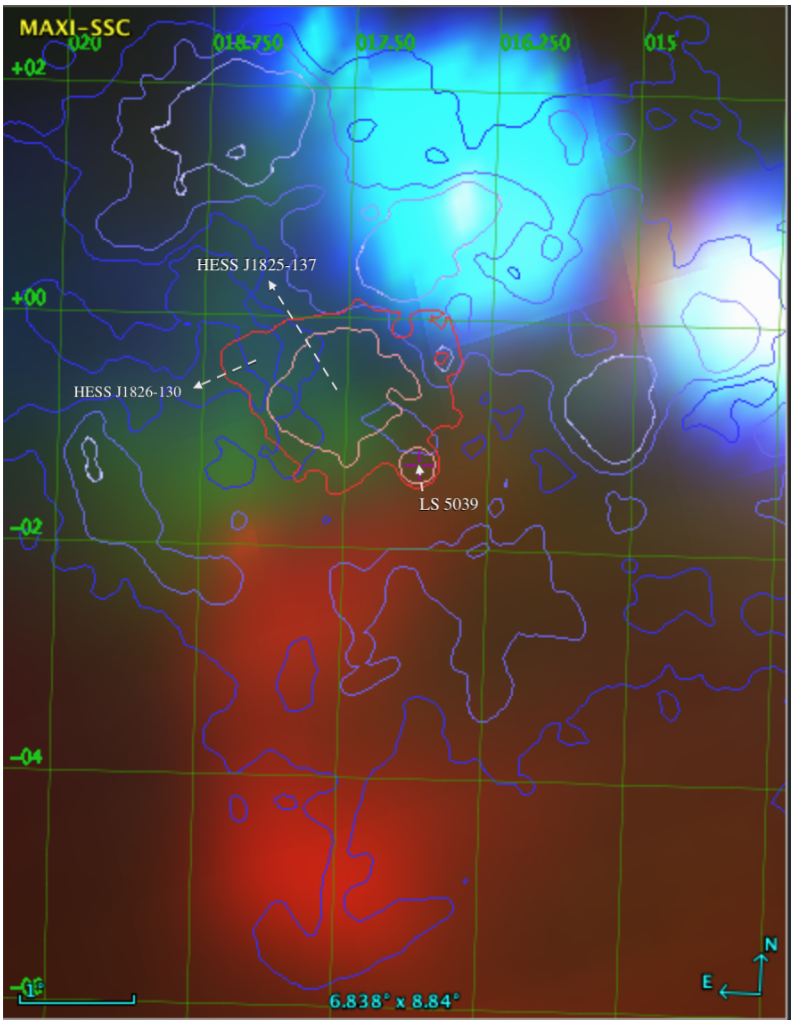

Figure 5.7: X-ray emission from MAXI SSC by Mihara et al. (2014) towards the Hα jet and in Red contours are for the 5σ, 10σ, and 50σ TeV gamma-ray emission HESS J1825-137, HESS 1826-130 and HESS J1826-148 from HESS. Using `Aladin` to produce the X-ray image with in red 0.7-1.7 keV, green 1.7-4 keV and blue in 4.0-7.0 keV. Hα contours in blue with limits of 51, 102, and 204 Rayleigh overlaps the X-ray.

The MAXI solid slit camera (SSC) is an X-ray instrument on the International Space Station, and it observes three different energies from soft to hard X-rays. The first

sky survey using this instrument was released by Mihara et al. (2014). Figure 5.7 shows the total emission in each energy band colour red 0.7-1.7 keV, green 1.7-4 keV, and blue in 4.0-7.0 keV. Using the MAXI/SSC X-ray map 2009-2015 from `Aladin`[2] we can clearly see an overlap between the soft X-ray in the 0.7-1.7 keV (Mihara et al., 2014) and the Hα emission.

For example, the jets of microquasar XTE J1550–564 at a distance of 5.3 kpc have been studied by Corbel et al. (2002). Observation with X-ray in the 0.3 keV to 8 keV band have resolved the length of the jets to be 0.75 pc and 0.59 pc (Corbel et al., 2002). This allows us to use this X-ray band as an indication of jets.

Broadly translated our findings indicate that LS 5039 is the most likely candidate that can produce such jet. The location of the Planck radio outflow and the H2O maser suggests a powerful sources such as LS 5039. Radio jets it is likely to be originate by LS 5039. The direction of X-ray and the Hα jets is different than both VLBI radio jets and Planck radio outflow, but they can be explained by the orbital motion and the magnetic field. Also, there is a possibility that this Hα jet created from the progenitor supernova of LS 5039.

[2] Bonnarel et al. (2000)

6 Conclusions and Future Work

In this study, we searched for Hα counterparts to a number of the HESS TeV gamma-ray sources. We used the Hα emission to search supernova remnants (SNR) and/or a stellar wind bubble (SWB) shock. Models of the SNR and SWB radii were used to predict the size of any interesting features to compare with the Hα and TeV gamma-ray morphology. Here, we summarise the key results of this study. In addition, we identified the uniquely Hα long jet in the HESS J1825-137 and LS 5039 region and discussed its potential origin.

The SNR model calculates a predicted radius for an assumed age, distance, and ISM density. In this study, we used the ISM density, age, and location of the local pulsar thought to be associated with the TeV source mentioned in Table A.1, A.2. The SNR, SWB model was performed and centred at the location of the pulsar. We assumed an average age for the SWB to propagate was 4000 kyr and the average ISM density was 0.1 particles per cm^3. An assumed lower limit of a O9 spectral progenitor star, and a higher limit of O2 spectral type were used in the SWB model.

In this study, we look in all sources listed in Table 3.1. for these sources, we have investigated *HESS J1813-178* , *HESS J1837-069*, and *HESS J1834-087* in the Hα line. SNR and SWB models were applied on each of these sources, and find there are no clear features in the Hα line that overlaps with our SNR and SWB models.

HESS J1303-631 has an interesting Hα morphology which overlaps with the SWB model. The stellar wind from the progenitor star of pulsar PSR J1301-6305 can be related to this feature in Hα.

HESS J1356-645 is classified as a PWN (Acero et al., 2013), and there is a nearby

arc located 2° below the Galactic plane which is not classified as H II or SNR. The morphology of the Hα arc combined with the fact that it overlaps with our model, indicates that it could be a possible SNR related feature.

The regions of HESS J1640-465, and HESS J1641-463 in Hα show an overlap with the SWB model centred at the location of PSR J1641-643. This may indicate a SWB shock caused by the progenitor star which created this emission in Hα.

HESS J1804-216 may be related to the SNR G8.7-0.1. The interesting arc morphology found in high resolution Hα observations indicates a plausible relationship between the TeV emission and the optical arc, suggesting an SNR shock.

HESS J1857+026 has a ring like dip in Hα and we find that this dip overlaps with our SWB model. This implies that this feature may be related to the progenitor star's stellar wind.

HESS J1912+101 is a shell-like TeV source which is important to consider due to the age of the PSR J1912+101 which is $2.0 \pm 0.7 \times 10^5$ yr. The region in the south contains several H II regions, one of which is G45.039-0.643, which has an irregular morphology suggesting that this H II region is related to this given source. We note that the north side of the TeV emission of HESS J1912+101 shows similar Hα morphology.

Hα optical observations towards *HESS J1825-137* , *HESS J1826-130* and *HESS J1826-148* reveals jet structure towards the south of the three TeV sources. In addition we found soft X-ray 0.7 keV to 1.7 keV emission overlaps the Hα jet. The Planck radio survey at high frequencies reveals another interesting bi-lobal jet/outflow structure that centres on LS 5039. There is however no discussion of this jet origin morphology in literature. We find that a potential source that can create this jet is LS 5039, a microquasar binary system, or it is created by the progenitor SN that created the compact object (black hole or neutron star) in LS5039.

6.1 Future Work

The Hα features that we have noticed need further study. Since Hα arcs are overlapping SNRs and other interesting features, we suggest that further detailed spectroscopic studies be taken towards a number of our chosen TeV source (e.g. towards HESS J1912+101, HESS J1804-216 and HESS J1356-645). We suggest taking a spectrum for the noted arcs , by using such analysis we could investigate if the ratio of $[S\,II]/H\alpha > 0.5$ and $[N\,II]/H\alpha > 0.5$. If these ratios are above 0.5 for the arcs, that would suggest that they are SNR related.

In addition, the investigation of the Hα jets toward LS 5039 needs multi-wavelength spectral observations in the direction of the bow shock. This observation will provide the distance to the bow shock which will help pinpoint its origin. Modelling the microquasar from the details provided will help to estimate the relationship between the binary system and the jet.

A Appendix

A.1 SNR and SWB Model Details

Here we present the details for SNR model that we used through out this project. The SNR radius result depends on the age of the SNR, as well as the initial SN type, distance to the source, and ISM number density surrounding the sources. We use the distance from the literature and an uncertainty in the distance of $\pm$ 0.5 kpc to produce a range of SNR radii. Table A.1 shows the ISM number density around the candidates of interest shown in Table 2.2. The ISM number density is one of the variables in the equation 2.9. Table A.1 shows the SNR model radii from the suspected origins of SNRs to the predicted edge of the shock front.

Sources Name HESS	Pulsar PSR	Distance kpc	Age kyr	Radii for Different Number density degree					
				SN II density n			SN Ia density n		
				n=0.1 cm^{-3}	0.35 cm^{-3}	0.006 cm^{-3}	0.1 cm^{-3}	0.35 cm^{-3}	0.006 cm^{-3}
J1303-631	J1301-6305	6.6	11	0.42°	0.33°	0.71°	0.28°	0.22°	0.49°
J1356-645	J1357-6429	2.4	7.3	0.97°	0.76°	1.63°	0.66°	0.52°	1.14°
J1640-465	J1640-4631	8.6	5	0.229°	0.18°	0.37°	0.15°	0.12°	0.26°
J1804-216	J1803-213	3.4	16	0.95°	0.74°	1.64°	0.65°	0.50°	1.13°
J1813-178	J1813-1749	4.7	5.4	0.43°	0.34°	0.71°	0.30°	0.23°	0.51°
J1834-087	J1833-0827	4	6	0.53°	0.42°	0.88°	0.36°	0.28°	0.62°
J1837-069	AX J1838.0-0655	6.6	22.3°	0.56°	0.44°	0.97°	0.38°	0.30°	0.66°
J1857+026	J1856+0245	9	21	0.40°	0.31°	0.69°	0.27°	0.21°	0.47°
J1912+101*	J1913+1011	4	169	2.12°	1.65°	3.72°	1.43°	1.11°	2.51°

Table A.1: SNR model radii used at the pulsar location, the distance to the pulsar and the age to assume the radii. *in HESS J1912+101 we use an ISM number density of n=6 particles percm^3.

Here, we will present the SWB model since we did not change the ISM number density for all of our candidates. These radii in Table A.2 represent the distance between the

initial source of the SNs and the edge of SWB shock propagation.

Sources Name HESS	Pulsar	Distance kpc	density ISM	Age kyr	Radii SWB degree O9	O2
J1834-087	PSR J1833-0827	4	0.1	6000	3.1°	2.1°
J1837-069	AX J1838.0-0655	6.6	0.1	22.3	1.9°	1.2°
J1813-178	PSR J1813-1749	4.7	0.1	5.4	2.7°	1.8°
J1356-645	PSR J1357-6429,	2.4	0.1	7.3	5.2°	3.5°
J1640-465	PSR J1640-4631	8.6	0.1	5	1.4°	0.9°
J1912+101	PSR J1913+1011	4	0.1	169	3.1°	2.1°
J1303-631	PSR J1301-6305	6.6	0.1	11	1.9°	1.2°
J1804-216	PSR J1803-213	3.4	0.1	16	4.8°	3.2°
J1857+026	PSR J1856+0245	9	0.1	21	1.4°	0.9°

Table A.2: SWB model radii used the pulsar location, the distance to the pulsar and the age to assume the radii. We assume an 4000 kyr as an a age for the initial star.

A.2 Formation of Gamma rays

Hadronic process

Gamma-ray from the hadronic scenario result from the collision of cosmic-rays CRs with matter in the ISM,

$$p + N \rightarrow N' + \pi^o \pi^{\pm} \tag{A.1}$$

where N is the material in the ISM and p is the CRs. The decay of the π^0 produces two γ-rays and the decay of $\pi^{\pm}$ gives $\mu^{\pm} + \nu_{\mu}\nu_{\mu} \rightarrow e^{\pm}$. The γ-ray energy band from GeV to TeV results from the decay of the π^0 and $\pi^{\pm}$ which creates the X-ray and radio emission via synchrotron radiation. The energy loss rate for the proton can be found by

$$\frac{dE_p}{dt} = (n\sigma_{pp} f c) E_p \ , \tag{A.2}$$

where n is the ISM number density, σ is the cross section, and $f \sim 0.5$ is the single interaction inelasticity and. dE_p is the proton energy change.

Leptonic process

Gamma-ray from the leptonic scenario occurs due to Inverse Compton (IC) scattering with the up-scatter of a soft photon γ to a gamma-ray and TeV,

$$e^- + \gamma_{soft} \rightarrow e^{'-} + \gamma_{TeV}$$

Bremsstrahlung radiation is also emitted when an electron (e^-) converts its energy to a photon as a result of passing by a nucleus. Synchrotron radiation occurs when the e^- spirals around magnetic field lines, producing either X-ray (keV), optical, radio or ultraviolet (eV),

$$e^- + B \rightarrow e^{'-} + \begin{cases} \gamma_{KeV} \\ \gamma_{eV}. \end{cases}$$

where the B is the strength of magnetic field. γ_{KeV} and γ_{TeV} is the photon energy.
In general, The IC and synchrotron have the same electron population, so the two processes compete. Therefore, there is a relationship between the TeV γ-ray and X-ray synchrotron fluxes as discussed by Aharonian et al. (1997). Equation A.3 describes the relationship between TeV and X-ray with the magnetic field B. The result of Equation A.3 , in the leptonic scenario, the TeV and X-ray have a relationship and the radio and X-ray are correlated through synchrotron of accelerate e^- and/or e^+ from CRs interaction with the ISM in a hadronic process:

$$F_{IC} \sim \frac{F_{synchrotron}}{10(B/10\mu G)^2} \tag{A.3}$$

here, F_{IC} is the flux form IC scattering and $F_{synchrotron}$ is the flux from Synchrotron. B is the magnetic field.

A.3 HFI Planck Survey

The Planck radio survey towards LS 5039 covered the Galactic plane in nine frequencies Planck Collaboration (2011). There are high frequency bands (HFI) 100, 143, 217, 353, 545,

and 857 GHz and Low Frequency Instrument (LFI) 30, 44, and 70 GHz. These observations have a resolution from 33-4.2 arc-min. Here we present the bi-lobal outflow feature observed by Planck survey that discussed in Chapter 5. There are three different bands 857 GHz, 353 GHz, and 217 GHz in Figures A.1 A.2 A.3. This feature is not clearly shown in Planck 143, 70, 44, 30 GHz images.

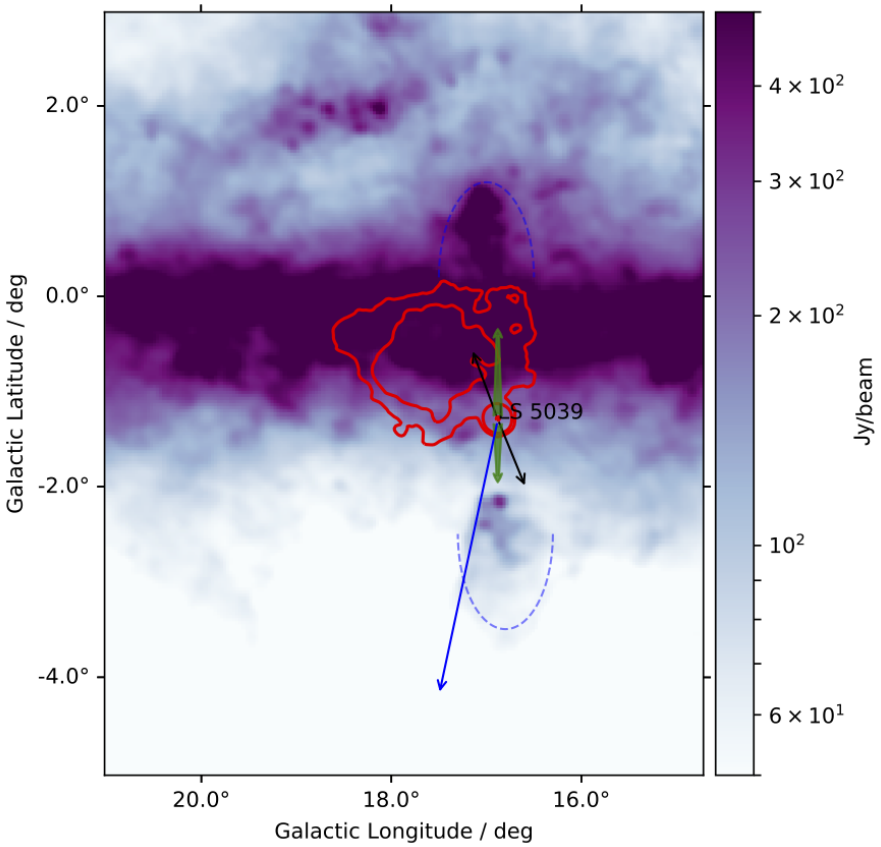

Figure A.1: Planck Radio 857 GHz image Planck Collaboration (2011) for the region of LS 5039 showing a blowout structure in two directions. Red contours are for the 5σ, 10σ, and 50σ TeV gamma-ray emission HESS J1825-137, HESS 1826-130 and HESS J1826-148 from HESS. Green arrows show the direction for the jets matching the Planck features. The yellow arrow indicates the Hα jet and the X-ray extended jet. The black arrows show the direction of the milliarcsecond radio jets (Paredes, 2002). The H2O maser location is noted (Kalenskii and Shchurov, 2016).

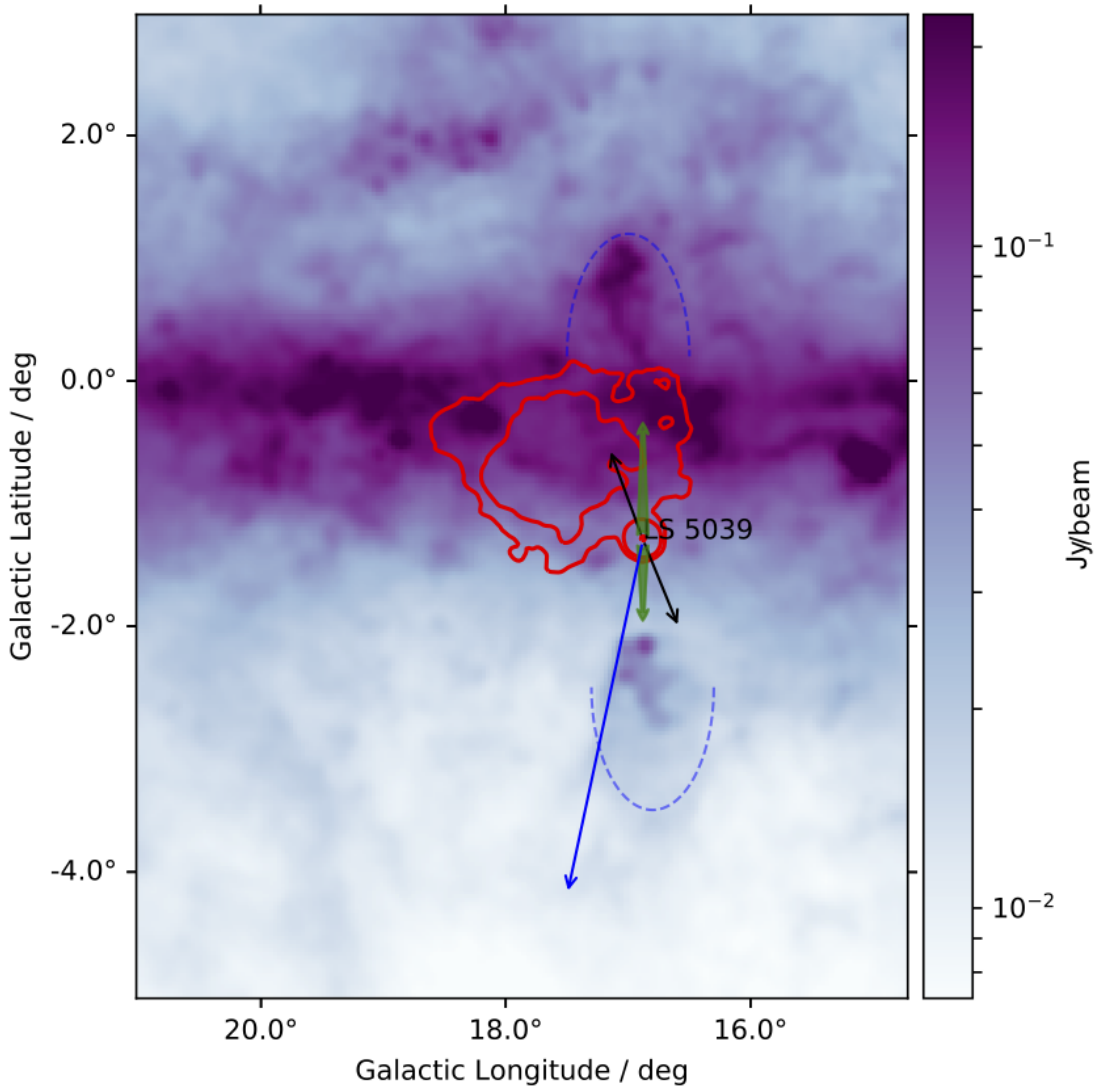

Figure A.2: Planck Radio 353 GHz image Planck Collaboration (2011) for the region of LS 5039 showing a blowout structure in two directions. Red contours are for the 5σ, 10σ, and 50σ TeV gamma-ray emission HESS J1825-137, HESS 1826-130 and HESS J1826-148 from HESS. Green arrows show the direction for the jets matching the Planck features. The yellow arrow indicates the Hα jet and the X-ray extended jet. The black arrows show the direction of the milliarcsecond radio jets (Paredes, 2002). The H2O maser location is noted (Kalenskii and Shchurov, 2016).

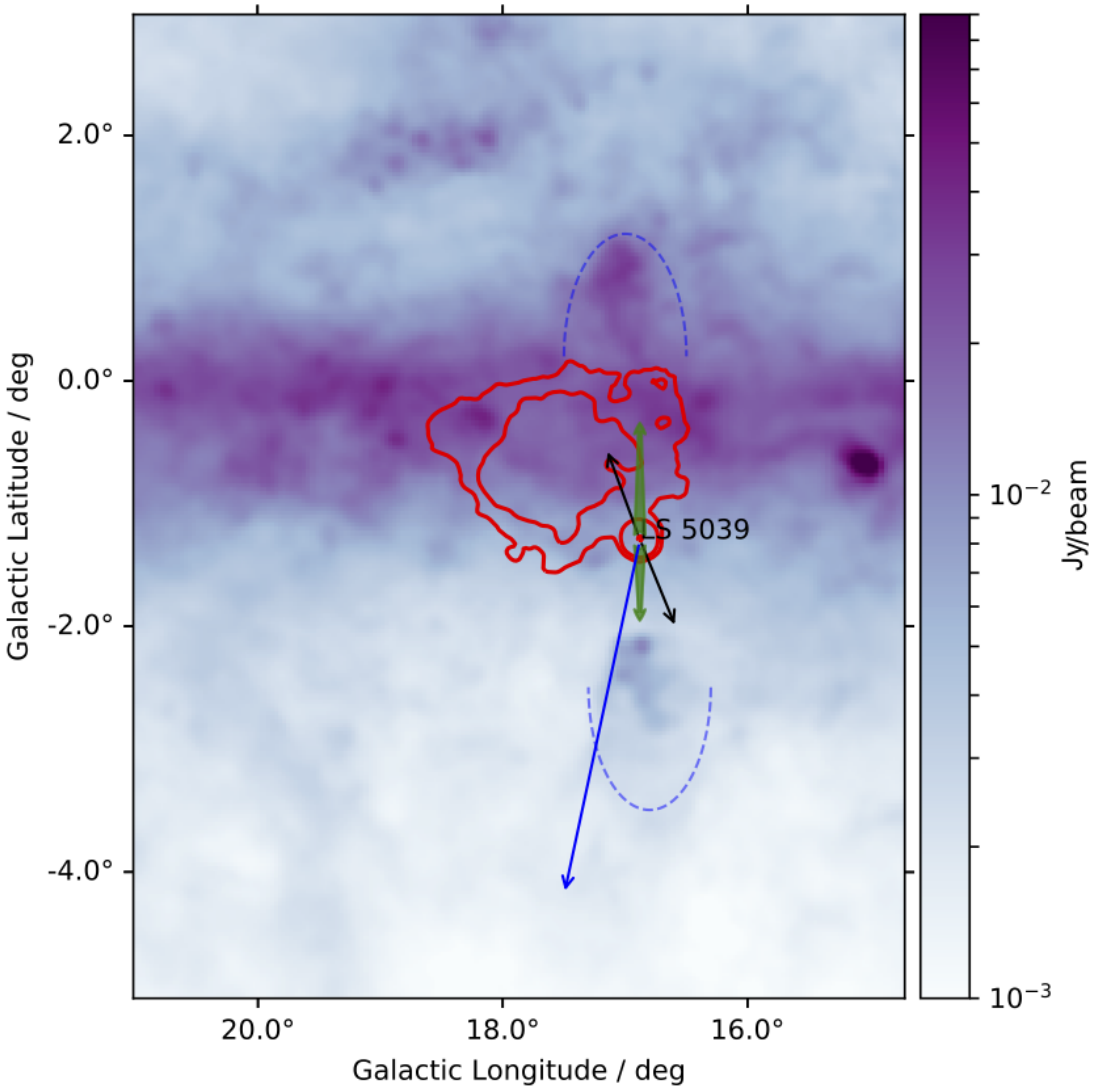

Figure A.3: Planck Radio 217 GHz image Planck Collaboration (2011) for the region of LS 5039 showing a blowout structure in two directions. Red contours are for the 5σ, 10σ, and 50σ TeV gamma-ray emission HESS J1825-137, HESS 1826-130 and HESS J1826-148 from HESS. Green arrows show the direction for the jets matching the Planck features. The yellow arrow indicates the Hα jet and the X-ray extended jet. The black arrows show the direction of the milliarcsecond radio jets (Paredes, 2002). The H2O maser location is noted (Kalenskii and Shchurov, 2016).

A.4 SWB Model for Several Candidates

Here we will present the SWB model for some of our HESS sources that have no indications of any obvious relationship between Hα and the SWB model. We use equation 2.10 to find SWB radius. We assume two limits from the energetics of the progenitor stars having the spectral types O9 and O2 as progenitor star. Also, we assume an age for the progenitor star of 4×10^6 yr. The ISM number density for the SWB model is n=0.1 cm^{-3} as an average Galactic plane ISM density, and the location of the progenitor star is the pulsar possibly associated Table A.2.

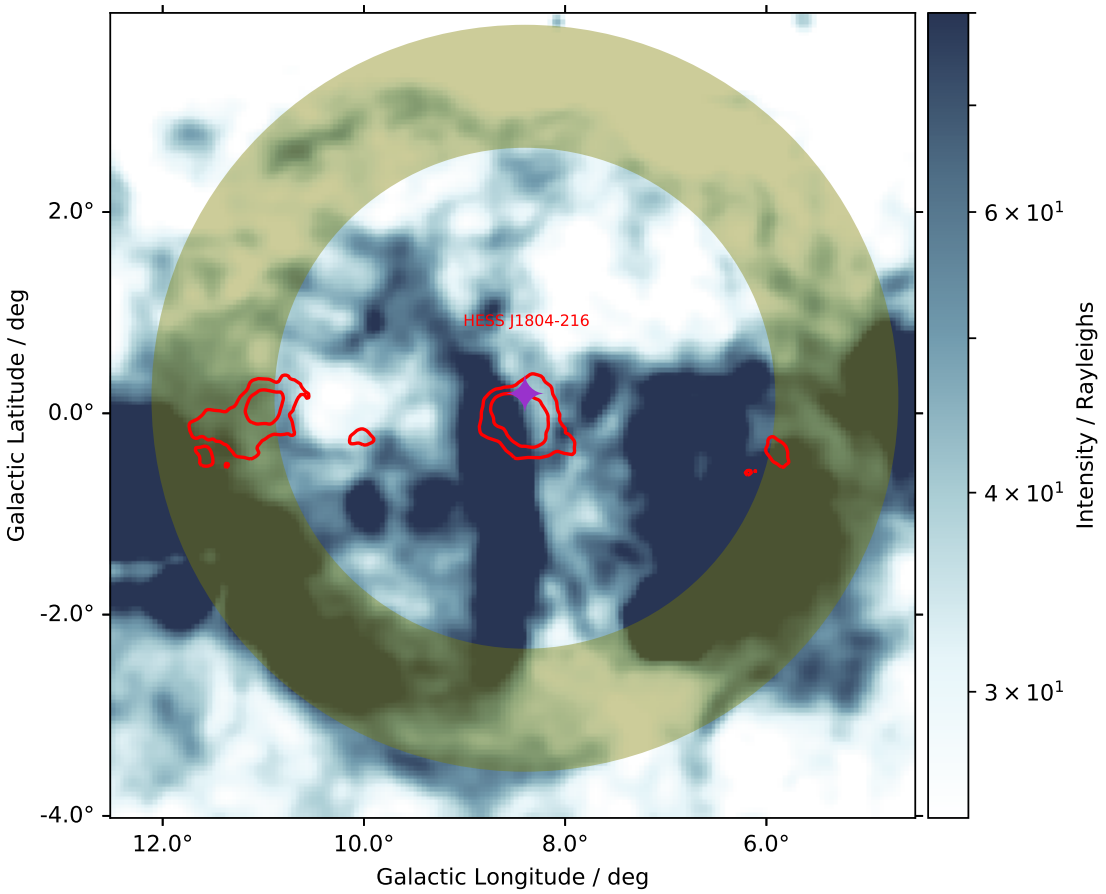

Figure A.4: Hα image by Finkbeiner (2003) towards HESS J1804-216. TeV emission in red contours with 5σ and 10σ significance. The SWB model is in light green assuming a density of n=0.1 particle per cm^3 and centred at PSR J1803-2137.

The SWB model for HESS J1804-216 takes a large scale in the field of view where it extends to

neighbouring TeV emissions (Figure A.4). We use the location and age of the PSR B1800-21 to determine the range of the SWB shock. There is no clear feature that is shown in the Hα emission.

HESS J1813-178 is a well known PWN located at a distance of 4.8 kpc. The SWB model is centred at the location of the pulsar PSR J1813-1749 and assumed an ISM number density n=0.1 cm^{-3} and is shown in Figure A.5. There is no interesting feature that overlaps with the SWB model. Also, the SWB model overlaps with another TeV sources.

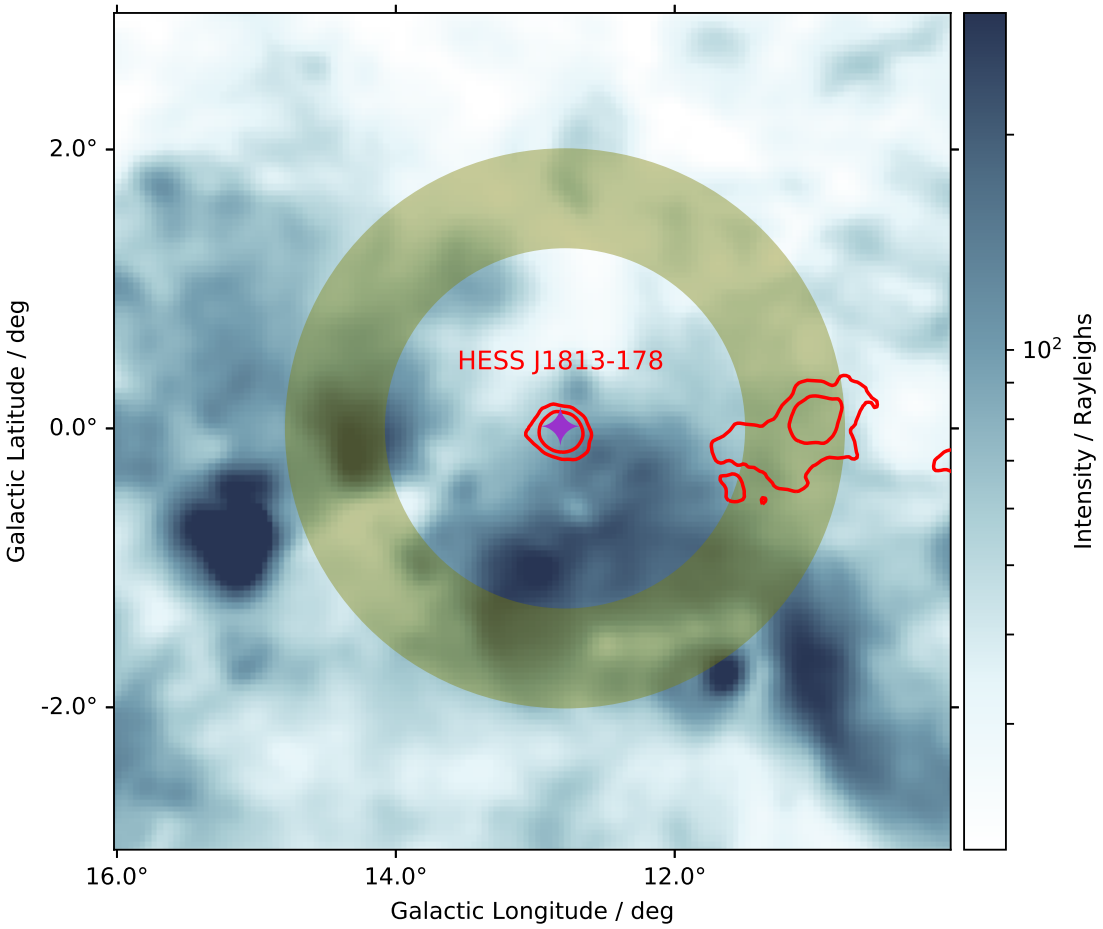

Figure A.5: Hα image by Finkbeiner (2003) towards HESS J1813-178. The red contours shows TeV gamma-ray emission limited with significance 5σ and 10σ. The SWB model is shown in light green assuming a density of n=0.1 particle per cm^3 and centred at PSR J1813-1749.

HESS J1837-069 is an extended TeV emission source.The SWB model is centred at the location

of the pulsar PSR J1838-0655 and assumed an ISM number density n=0.1 cm^{-3} is shown in Figure A.6. There is no interesting feature that overlaps with the SWB model. Also, the SWB model overlaps with another TeV source.

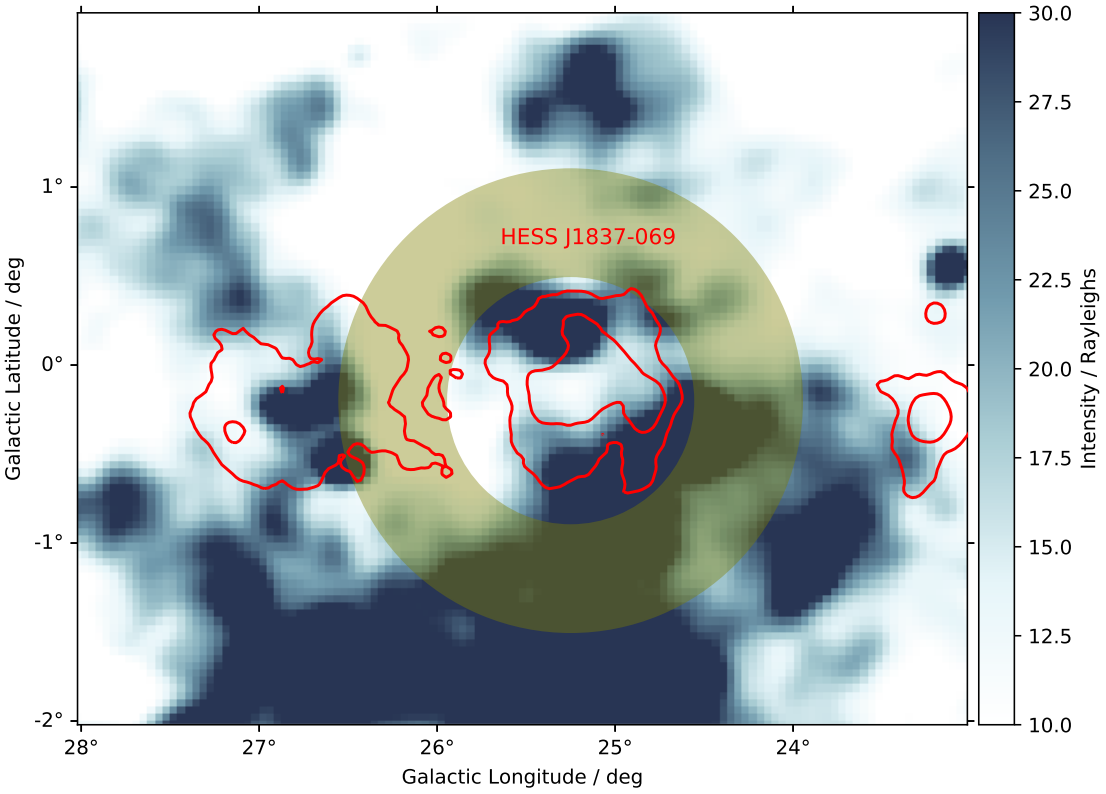

Figure A.6: Hα image by Finkbeiner (2003) towards the TeV emission in red contour 5σ and 10σ of HESS J1837-069. The SWB model is in light green assuming a density of n=0.1 cm^{-3} and centred at PSR J1838-0655.

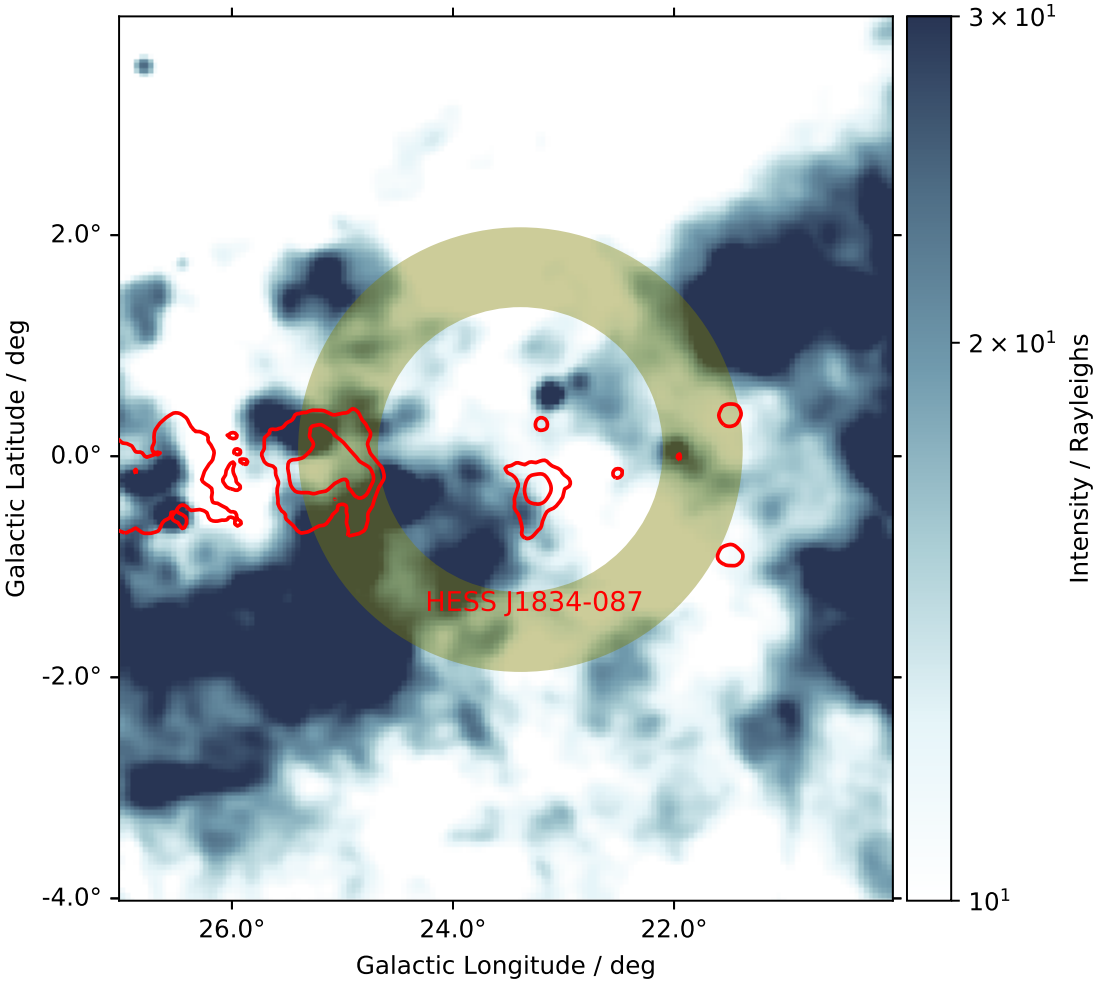

Figure A.7: Hα image by Finkbeiner (2003) towards the HESS J1834-087. The red contour show the TeV significance at the 5σ and 10σ. The SWB model is shown in light green assuming a a number density of n=0.1 particle per cm^3 and centred at PSR J1833-0827.

HESS J1834-087 is an interesting TeV emission due to its overlap with SNR W41. The SWB model is centred at the location of the pulsar PSR J1833-0827 and assumed a ISM number density n=0.1 cm^{-3} is shown in Figure A.7. There is no interesting feature that overlaps with the SWB model. Also, the SWB model overlaps with another TeV source.

A.5 H II Regions towards GS 018-04+44

Here we present all the H II regions with known distance toward the Scutum supershell. There are 23 known H II regions with distance 2-4 kpc which is almost located at the Scutum supershell. These regions have different radius varying from 31 to 1130 arc-second.

H II region Name	l degree	b degree	Radius arc-sec	Distance kpc	$\pm$Distance kpc
G016.285-00.171	16.2	-0.17	113	4.1	0.4
G016.424-00.201	16.4	-0.2	60	3.9	0.4
G016.583-00.053	16.5	-0.05	29	3.6	0.3
G016.648-00.357	16.6	-0.35	485	3.9	0.4
G016.856-01.156	16.8	-1.15	718	2.2	0.6
G016.993+00.873	16.9	0.87	1124	2.6	0.5
G018.144-00.281	18.1	-0.28	183	4.2	0.4
G018.152+00.090	18.1	0.09	93	4.1	0.4
G018.187-00.415	18.18	-0.41	226	3.6	0.4
G018.253-00.298	18.2	-0.29	205	4.0	0.4
G018.305-00.391	18.3	-0.39	60	3.0	0.5
G018.371-00.382	18.37	-0.38	26	3.7	0.4
G018.669+01.965	18.67	1.96	272	2.6	0.5
G018.824-00.467	18.82	-0.46	50	4.5	0.4
G018.881-00.493	18.88	-0.49	109	4.6	0.4
G018.978+00.030	18.97	0.03	275	4.0	0.4
G019.045-00.588	19.04	-0.58	120	4.7	0.4
G019.064-00.282	19.06	-0.28	79	4.6	0.4
G019.077-00.291	19.07	-0.29	31	4.6	0.4
G019.489+00.135	19.49	0.13	52	1.9	0.6
G019.504-00.449	19.50	-0.44	51	4.5	0.4
G019.611-00.254	19.61	-0.25	31	3.4	0.4
G019.821-00.325	19.82	-0.32	63	3.5	0.4

Table A.3: H II regions towards HESS J1825 area (Anderson et al., 2014).

A.6 H-alpha Maps for all HESS TeV Sources

Here we present an overlapped image for all the sources in the HESS galactic plane survey from the Gamma-ray map with 3 σ cutoff level counters for TeV emissions with optical Hα map. This maps covers between $\pm$ 6 degrees galactic latitude and 265 to 60 degrees galactic longitude. HESS J0835-455, related to the Vela supernova remnant and well known radio source at a distance of approximately 250 pc, can be seen at $l \sim 265^{\circ}$. Additionally, this source is observable in the optical Hα.

There are two different images for each field of view of the galactic plane. The low intensity which will help to investigate features low Hα emission region. The high intensity will use the image, which will make the region with low Hα emission bright to search for features surrounding it. This will allow us to have idea in both high and low Hα intensity.

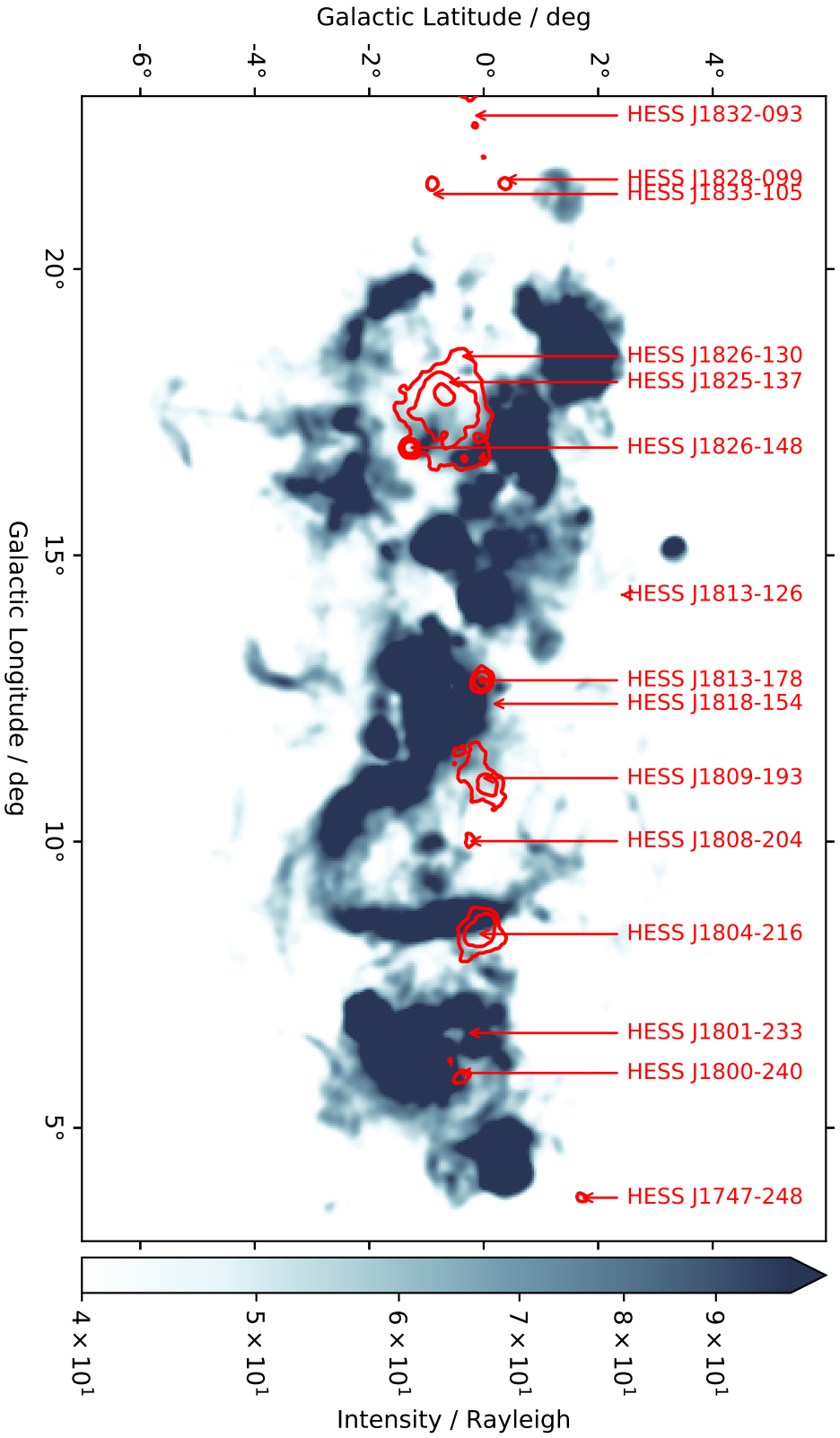
Galactic Latitude / deg
-6°
-4°
-2°
0°
2°
4°
HESS J1832-093
HESS J1828-099
HESS J1833-105
HESS J1826-130
HESS J1825-137
HESS J1826-148
HESS J1813-126
HESS J1813-178
HESS J1818-154
HESS J1809-193
HESS J1808-204
HESS J1804-216
HESS J1801-233
HESS J1800-240
HESS J1747-248
Galactic Longitude / deg
20°
15°
10°
5°
4 × 10¹
5 × 10¹
6 × 10¹
7 × 10¹
8 × 10¹
9 × 10¹
Intensity / Rayleigh

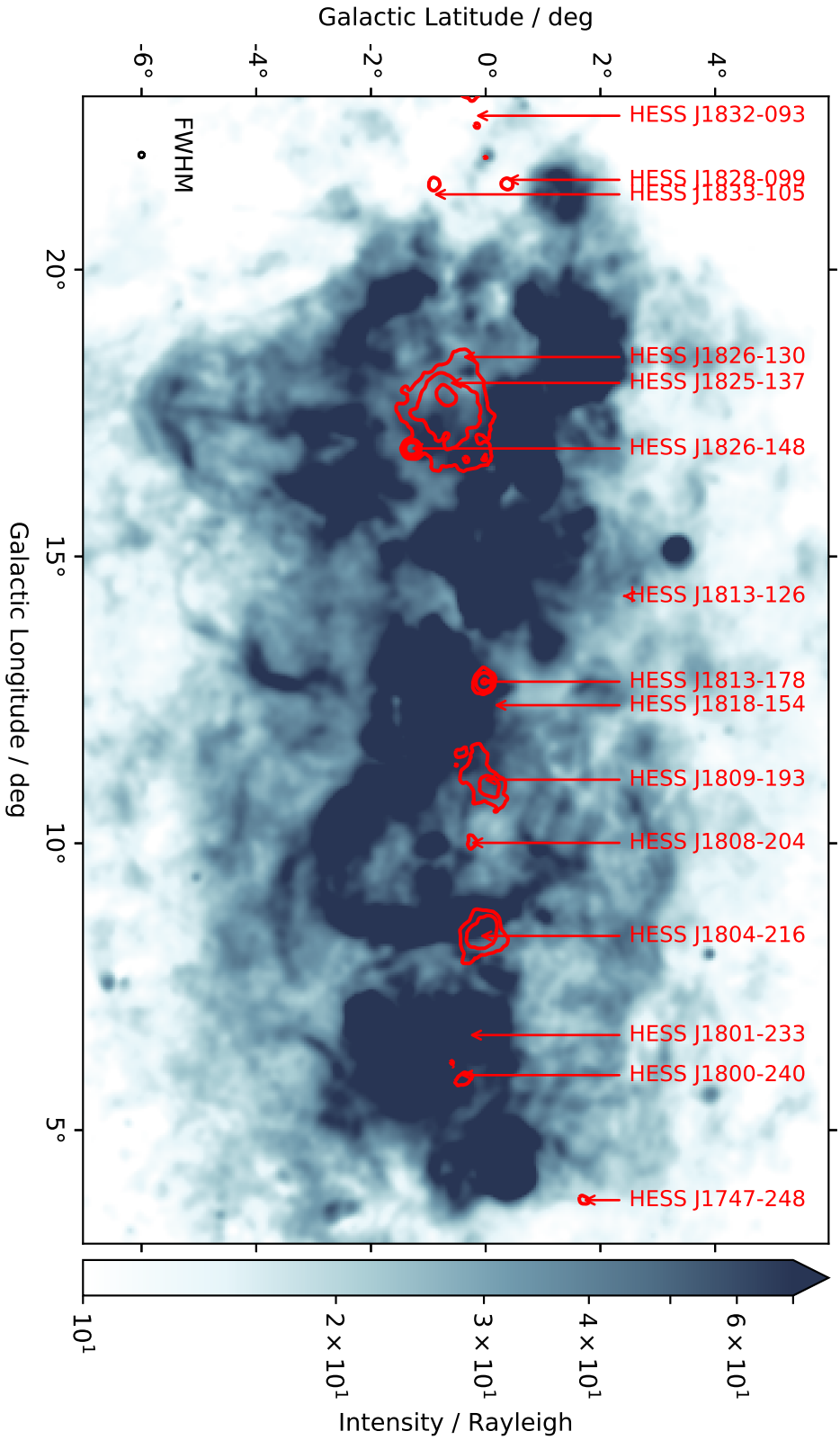
Galactic Latitude / deg
-6°
-4°
-2°
0°
2°
4°
FWHM
HESS J1832-093
HESS J1828-099
HESS J1833-105
20°
HESS J1826-130
HESS J1825-137
HESS J1826-148
15°
HESS J1813-126
HESS J1813-178
HESS J1818-154
HESS J1809-193
10°
HESS J1808-204
HESS J1804-216
HESS J1801-233
HESS J1800-240
5°
HESS J1747-248
Galactic Longitude / deg
10^1
2×10^1
3×10^1
4×10^1
6×10^1
Intensity / Rayleigh

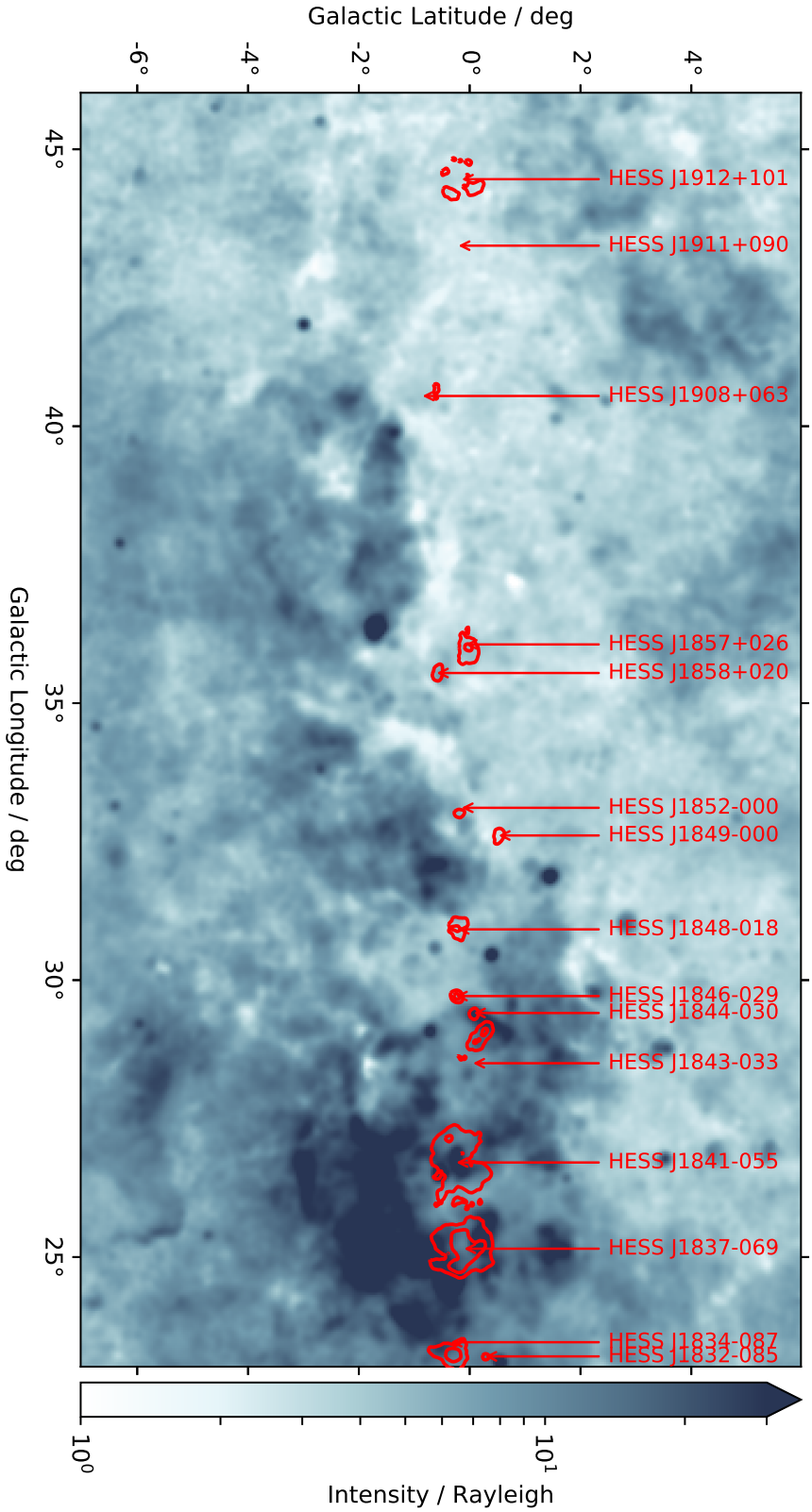
Galactic Latitude / deg
-6°
-4°
-2°
0°
2°
4°
45°
40°
35°
30°
25°
Galactic Longitude / deg
HESS J1912+101
HESS J1911+090
HESS J1908+063
HESS J1857+026
HESS J1858+020
HESS J1852-000
HESS J1849-000
HESS J1848-018
HESS J1846-029
HESS J1844-030
HESS J1843-033
HESS J1841-055
HESS J1837-069
HESS J1834-087
HESS J1832-085
10^0
10^1
Intensity / Rayleigh

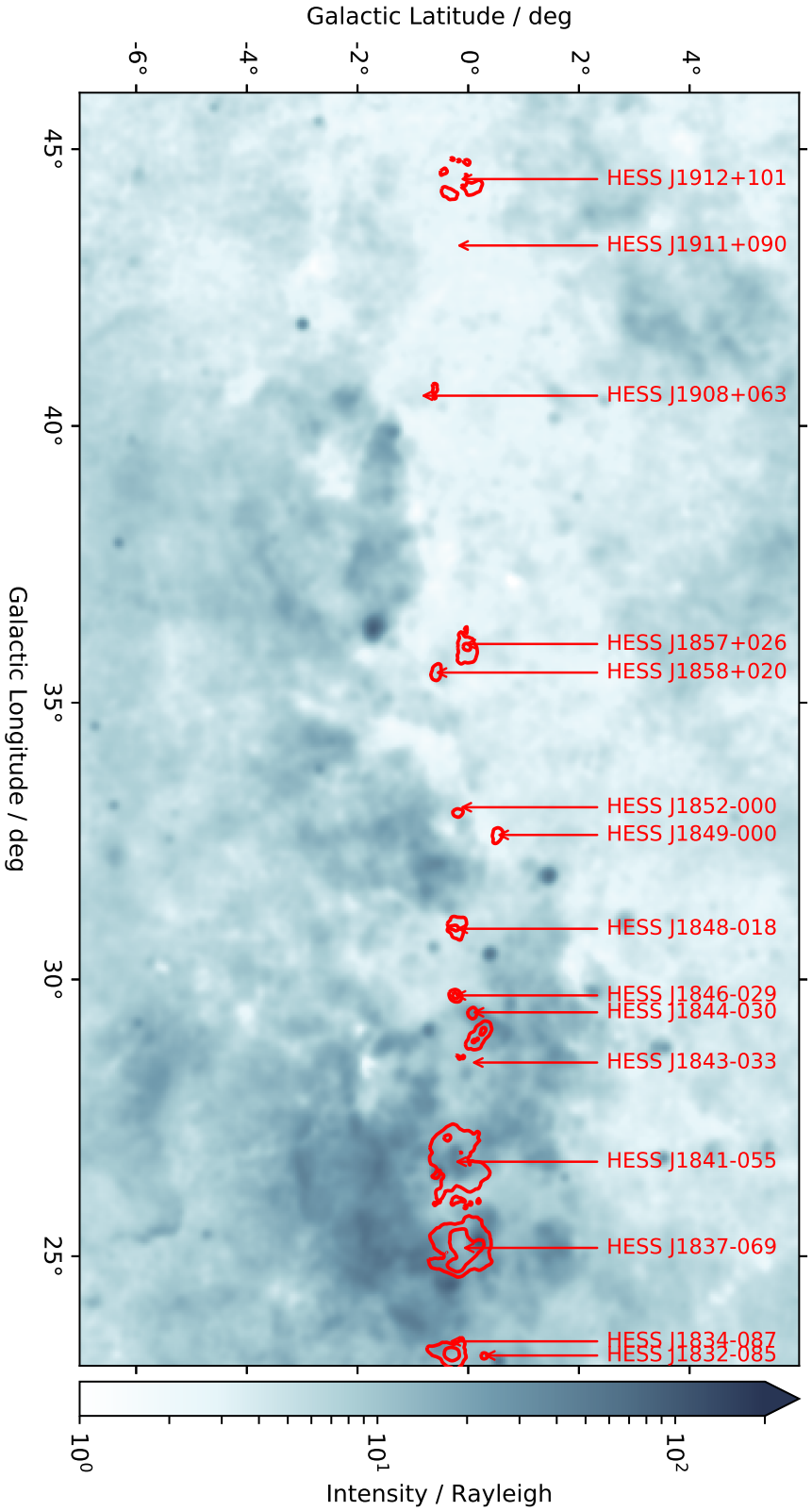
Galactic Latitude / deg
-6°
-4°
-2°
0°
2°
4°
Galactic Longitude / deg
45°
40°
35°
30°
25°
HESS J1912+101
HESS J1911+090
HESS J1908+063
HESS J1857+026
HESS J1858+020
HESS J1852-000
HESS J1849-000
HESS J1848-018
HESS J1846-029
HESS J1844-030
HESS J1843-033
HESS J1841-055
HESS J1837-069
HESS J1834-087
HESS J1832-085
10^0
10^1
10^2
Intensity / Rayleigh

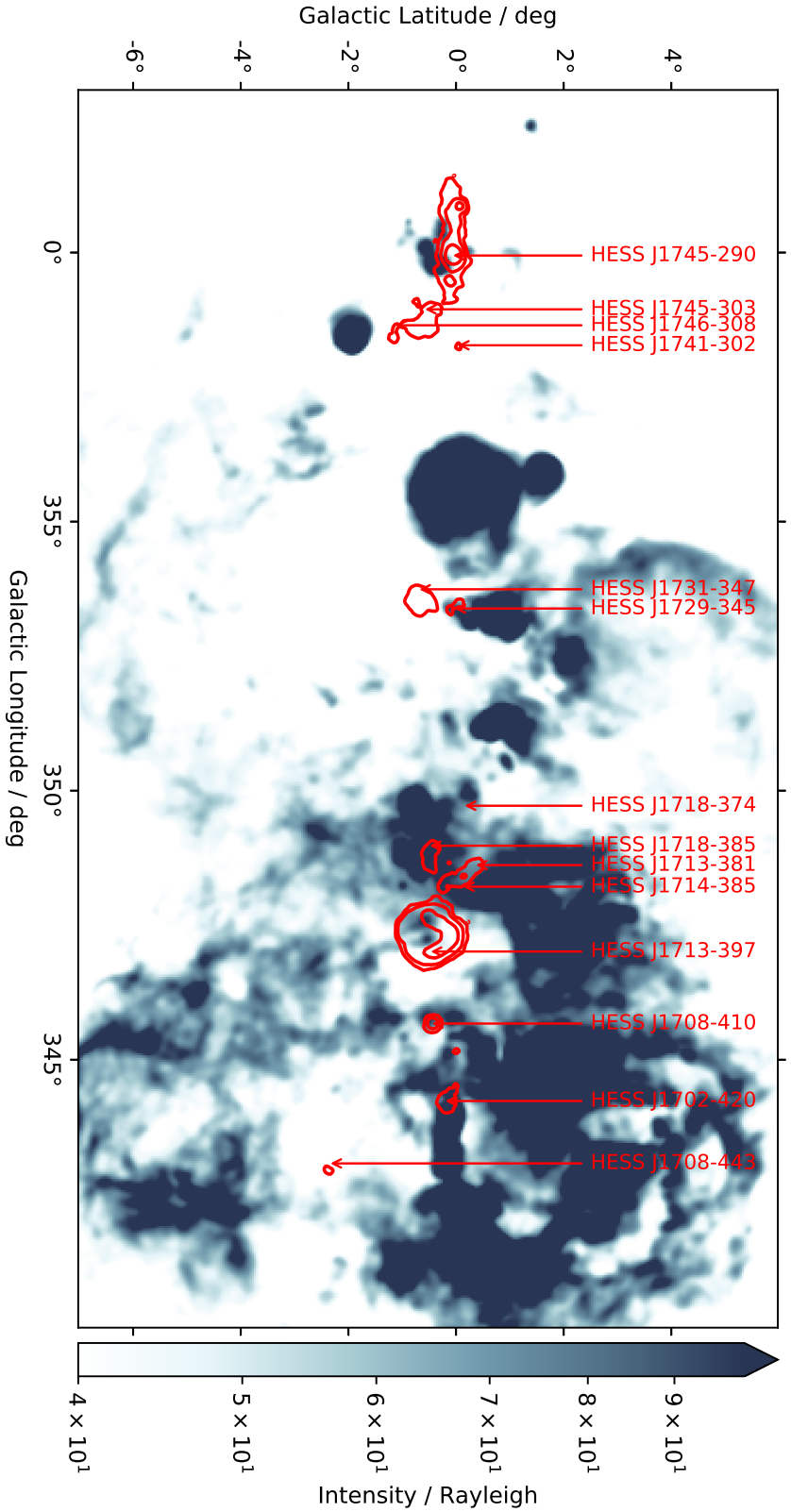
Galactic Latitude / deg
-6°
-4°
-2°
0°
2°
4°
Galactic Longitude / deg
0°
355°
350°
345°
HESS J1745-290
HESS J1745-303
HESS J1746-308
HESS J1741-302
HESS J1731-347
HESS J1729-345
HESS J1718-374
HESS J1718-385
HESS J1713-381
HESS J1714-385
HESS J1713-397
HESS J1708-410
HESS J1702-420
HESS J1708-443
4 × 10¹
5 × 10¹
6 × 10¹
7 × 10¹
8 × 10¹
9 × 10¹
Intensity / Rayleigh

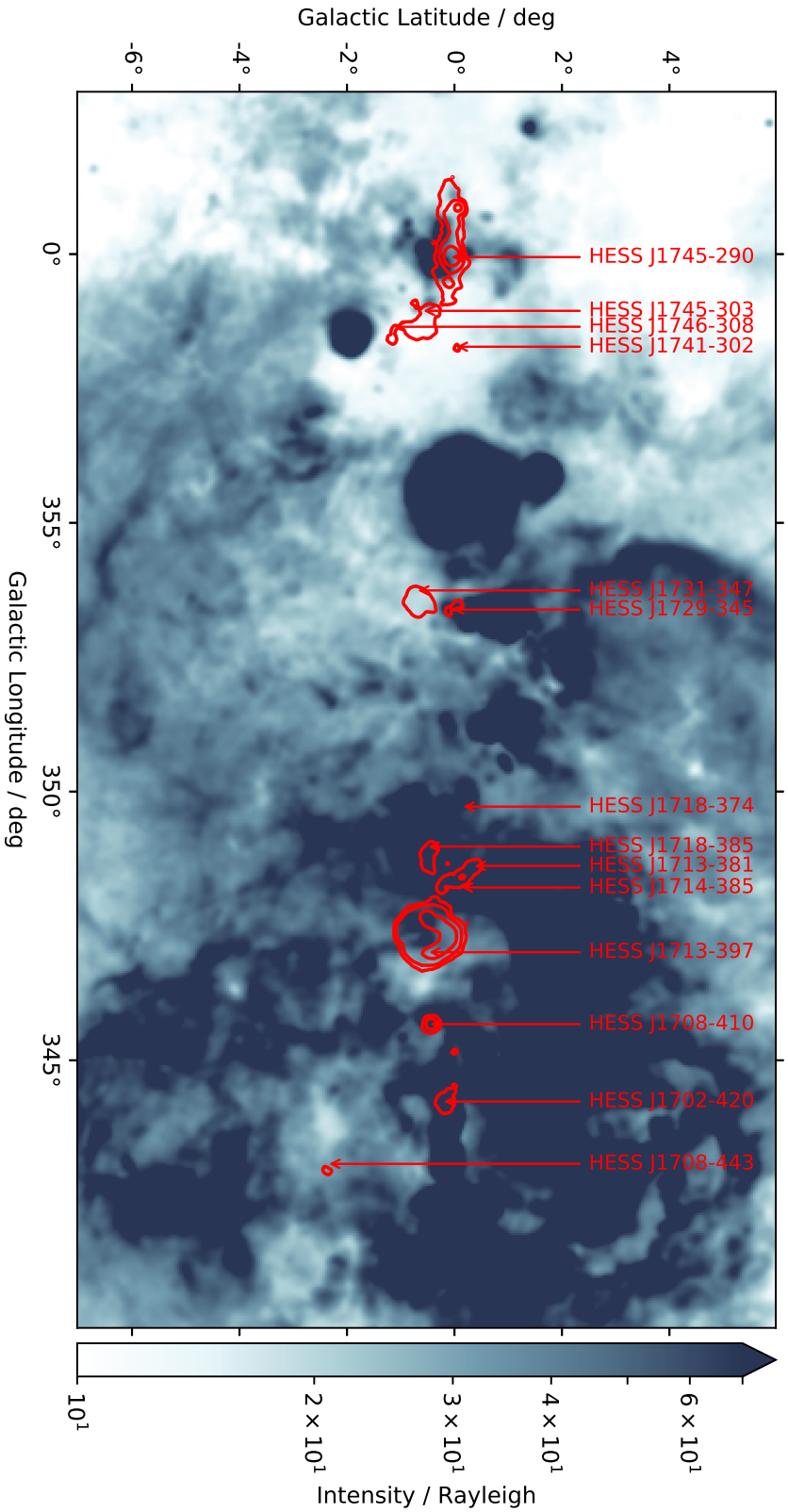
Galactic Latitude / deg
-6°
-4°
-2°
0°
2°
4°
Galactic Longitude / deg
0°
355°
350°
345°
HESS J1745-290
HESS J1745-303
HESS J1746-308
HESS J1741-302
HESS J1731-347
HESS J1729-345
HESS J1718-374
HESS J1718-385
HESS J1713-381
HESS J1714-385
HESS J1713-397
HESS J1708-410
HESS J1702-420
HESS J1708-443
10^1
2×10^1
3×10^1
4×10^1
6×10^1
Intensity / Rayleigh

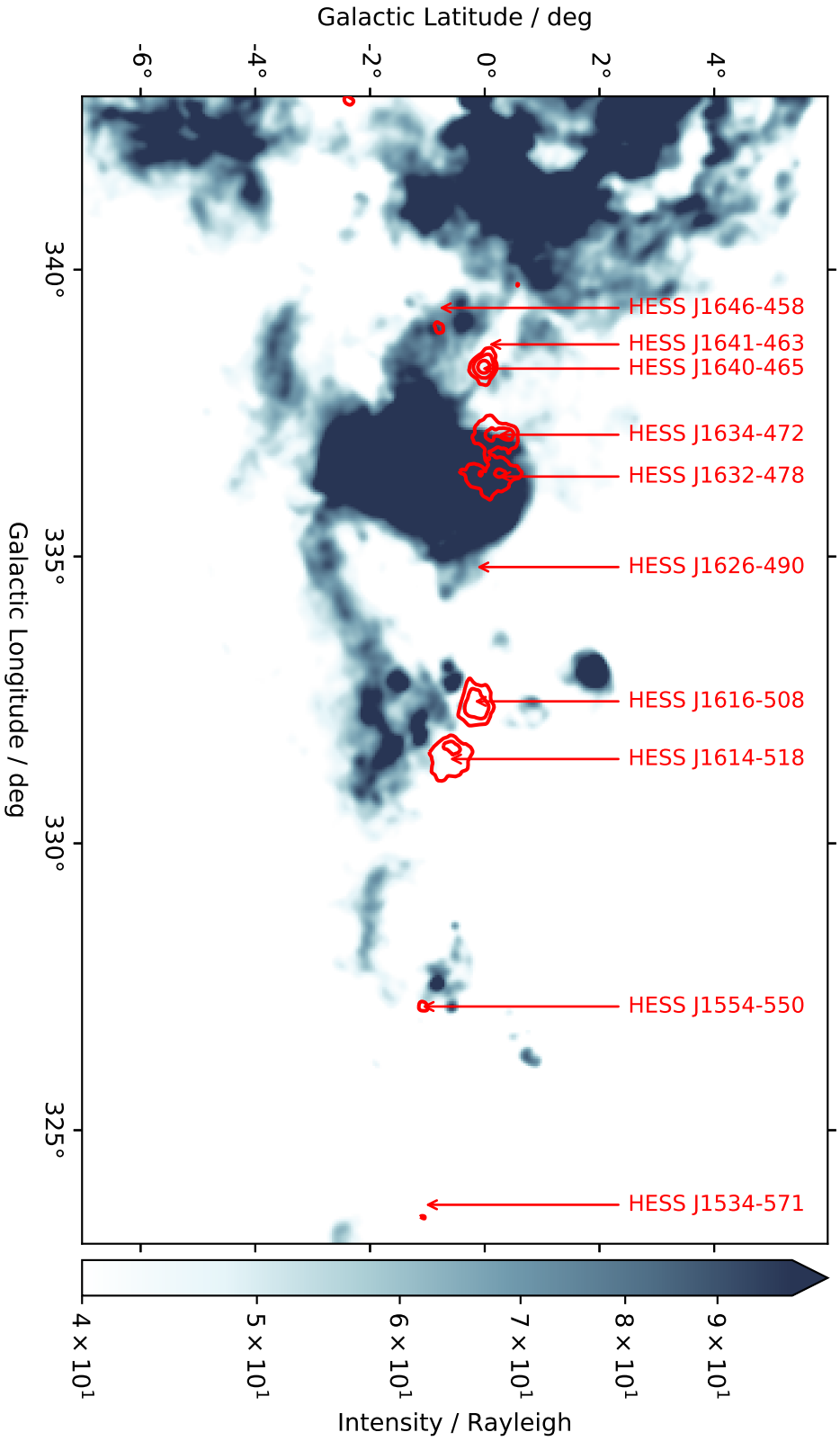
Galactic Latitude / deg
-6°
-4°
-2°
0°
2°
4°
Galactic Longitude / deg
340°
335°
330°
325°
HESS J1646-458
HESS J1641-463
HESS J1640-465
HESS J1634-472
HESS J1632-478
HESS J1626-490
HESS J1616-508
HESS J1614-518
HESS J1554-550
HESS J1534-571
4 × 10¹
5 × 10¹
6 × 10¹
7 × 10¹
8 × 10¹
9 × 10¹
Intensity / Rayleigh

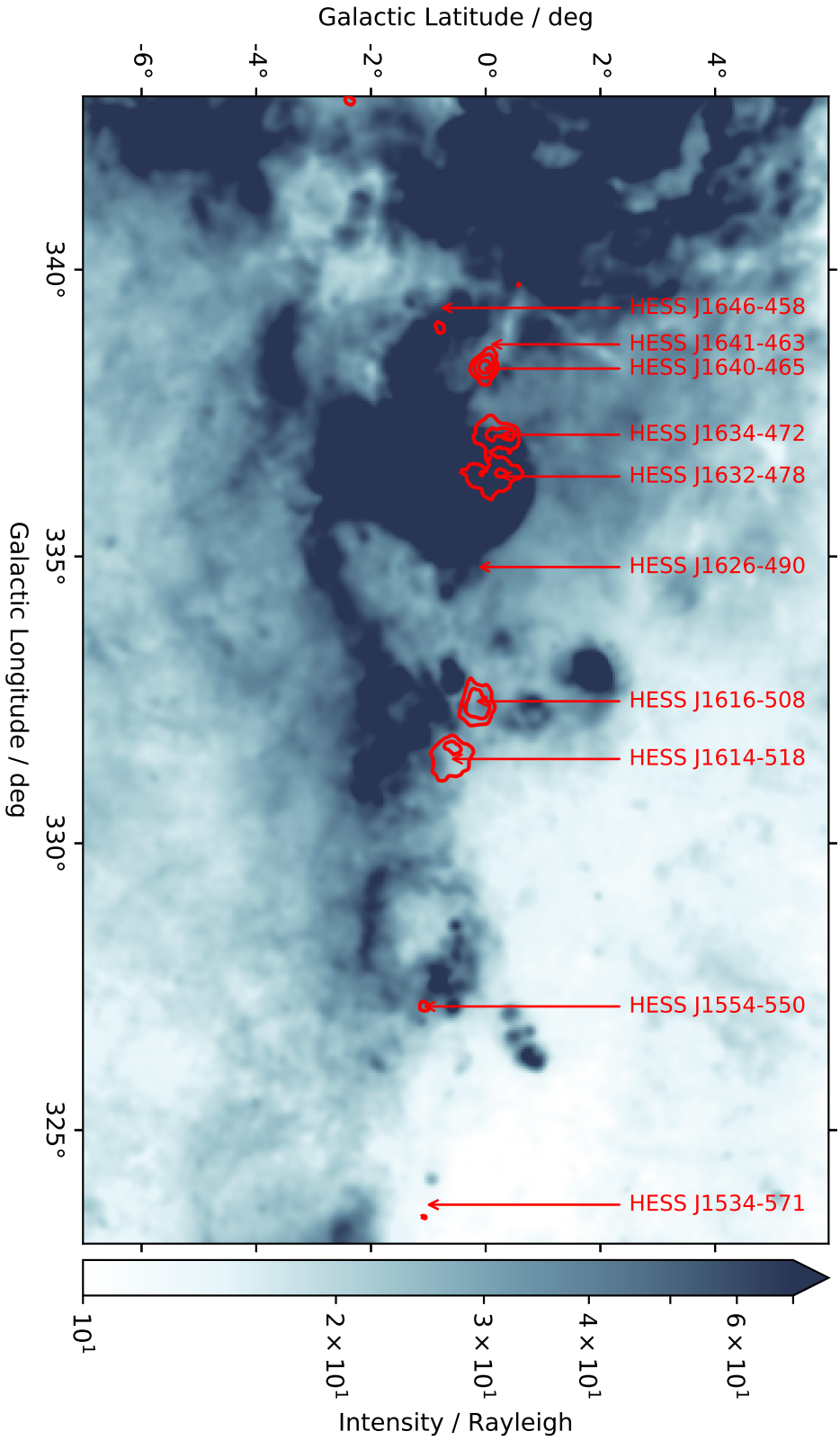
Galactic Latitude / deg
-6°
-4°
-2°
0°
2°
4°
Galactic Longitude / deg
340°
335°
330°
325°
HESS J1646-458
HESS J1641-463
HESS J1640-465
HESS J1634-472
HESS J1632-478
HESS J1626-490
HESS J1616-508
HESS J1614-518
HESS J1554-550
HESS J1534-571
10^1
2×10^1
3×10^1
4×10^1
6×10^1
Intensity / Rayleigh

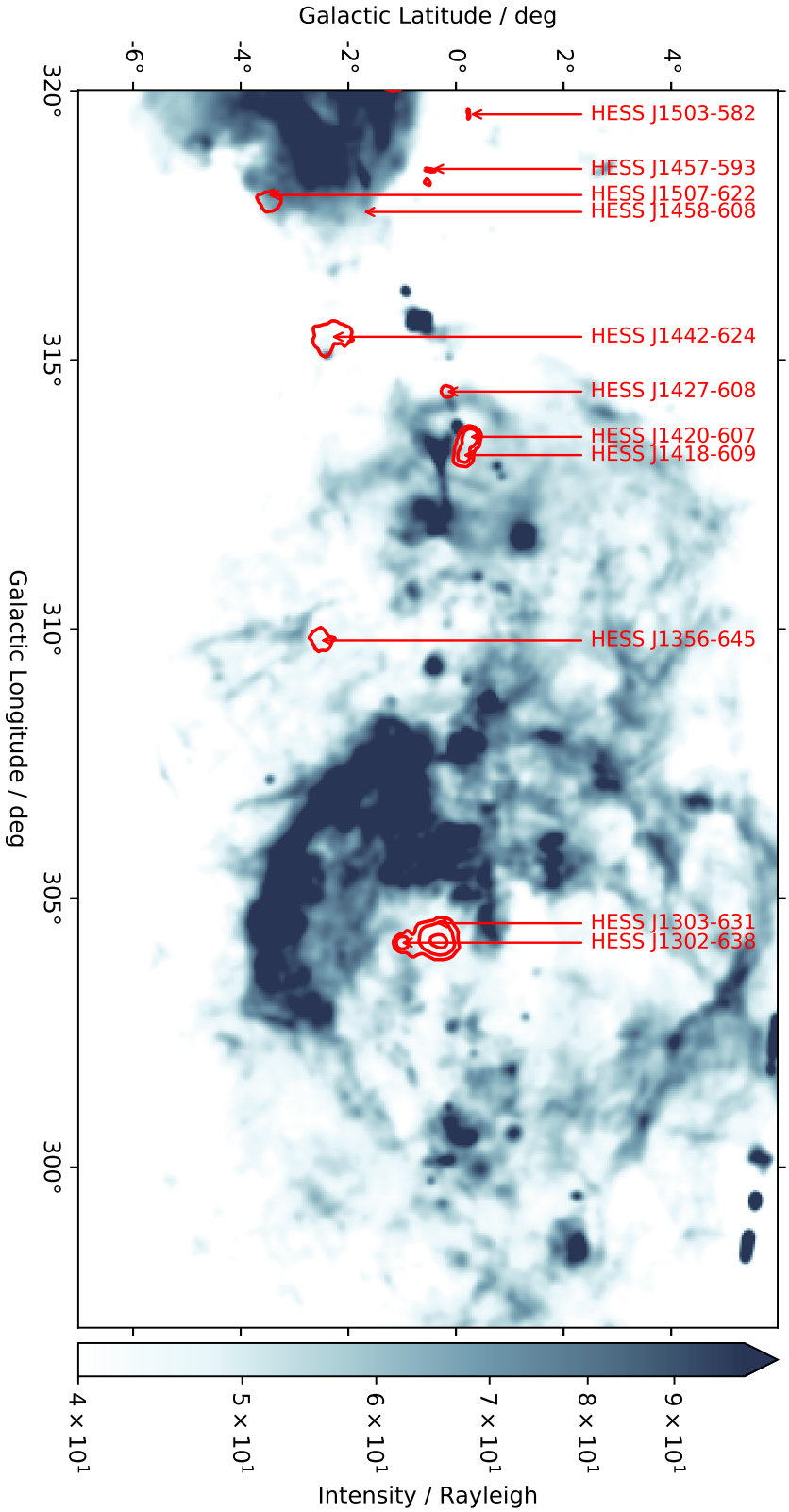
Galactic Latitude / deg
-6°
-4°
-2°
0°
2°
4°
320°
315°
310°
305°
300°
Galactic Longitude / deg
HESS J1503-582
HESS J1457-593
HESS J1507-622
HESS J1458-608
HESS J1442-624
HESS J1427-608
HESS J1420-607
HESS J1418-609
HESS J1356-645
HESS J1303-631
HESS J1302-638
4 × 10¹
5 × 10¹
6 × 10¹
7 × 10¹
8 × 10¹
9 × 10¹
Intensity / Rayleigh

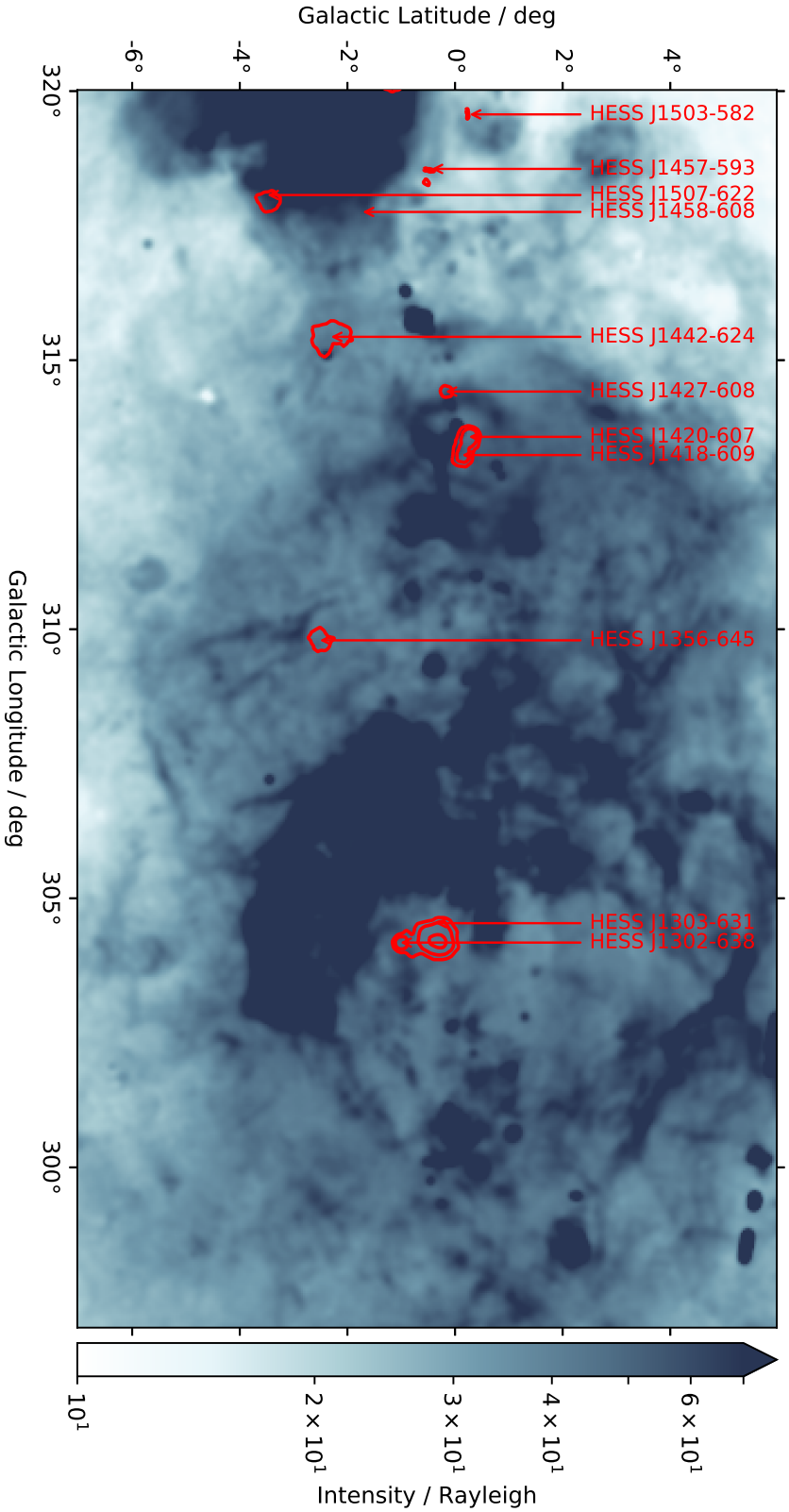
Galactic Latitude / deg
-6°
-4°
-2°
0°
2°
4°
320°
315°
310°
305°
300°
Galactic Longitude / deg
HESS J1503-582
HESS J1457-593
HESS J1507-622
HESS J1458-608
HESS J1442-624
HESS J1427-608
HESS J1420-607
HESS J1418-609
HESS J1356-645
HESS J1303-631
HESS J1302-638
10^1
2×10^1
3×10^1
4×10^1
6×10^1
Intensity / Rayleigh

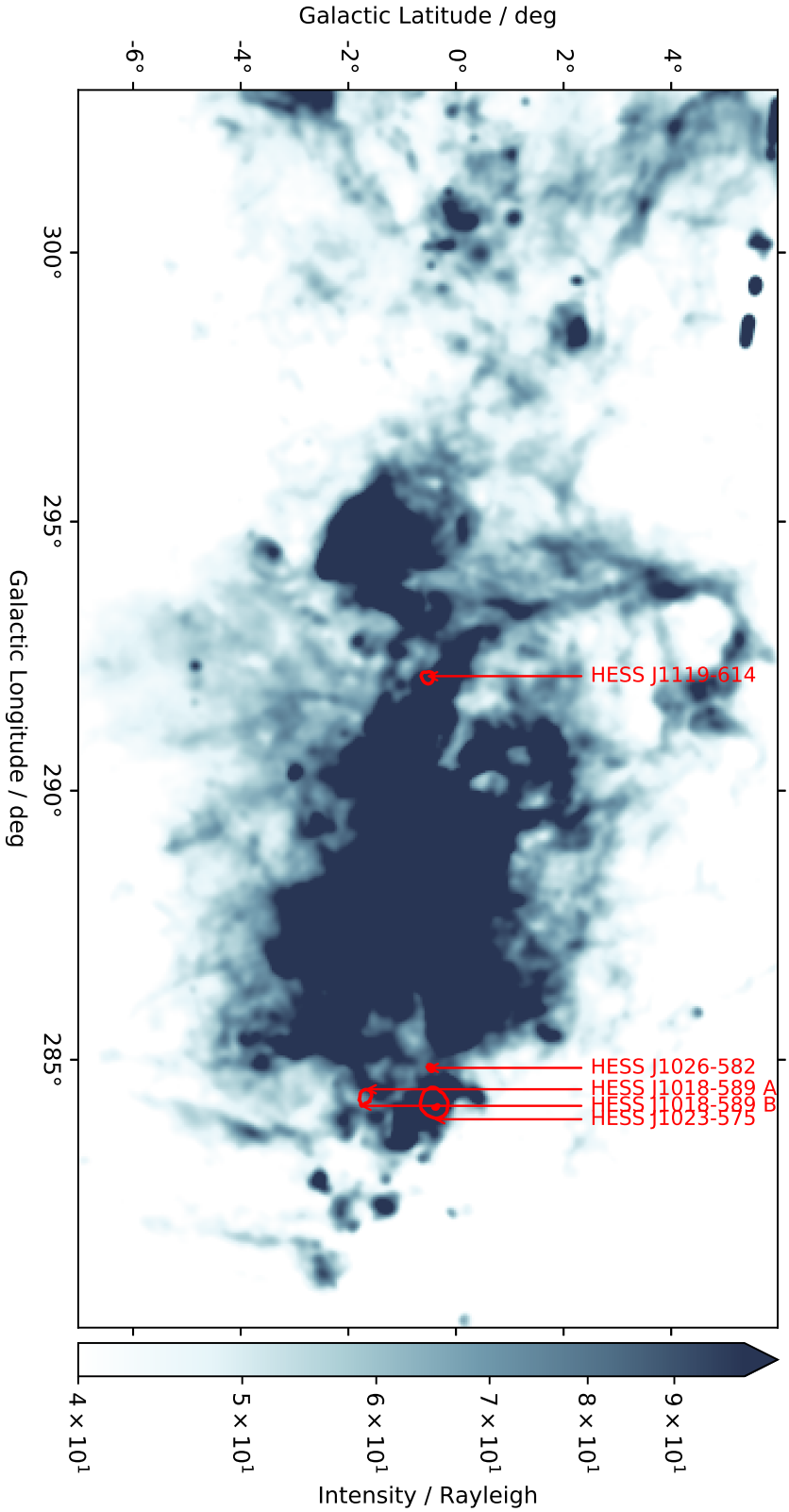
Galactic Latitude / deg
-6°
-4°
-2°
0°
2°
4°
Galactic Longitude / deg
300°
295°
290°
285°
HESS J1119-614
HESS J1026-582
HESS J1018-589 A
HESS J1018-589 B
HESS J1023-575
4 × 10¹
5 × 10¹
6 × 10¹
7 × 10¹
8 × 10¹
9 × 10¹
Intensity / Rayleigh

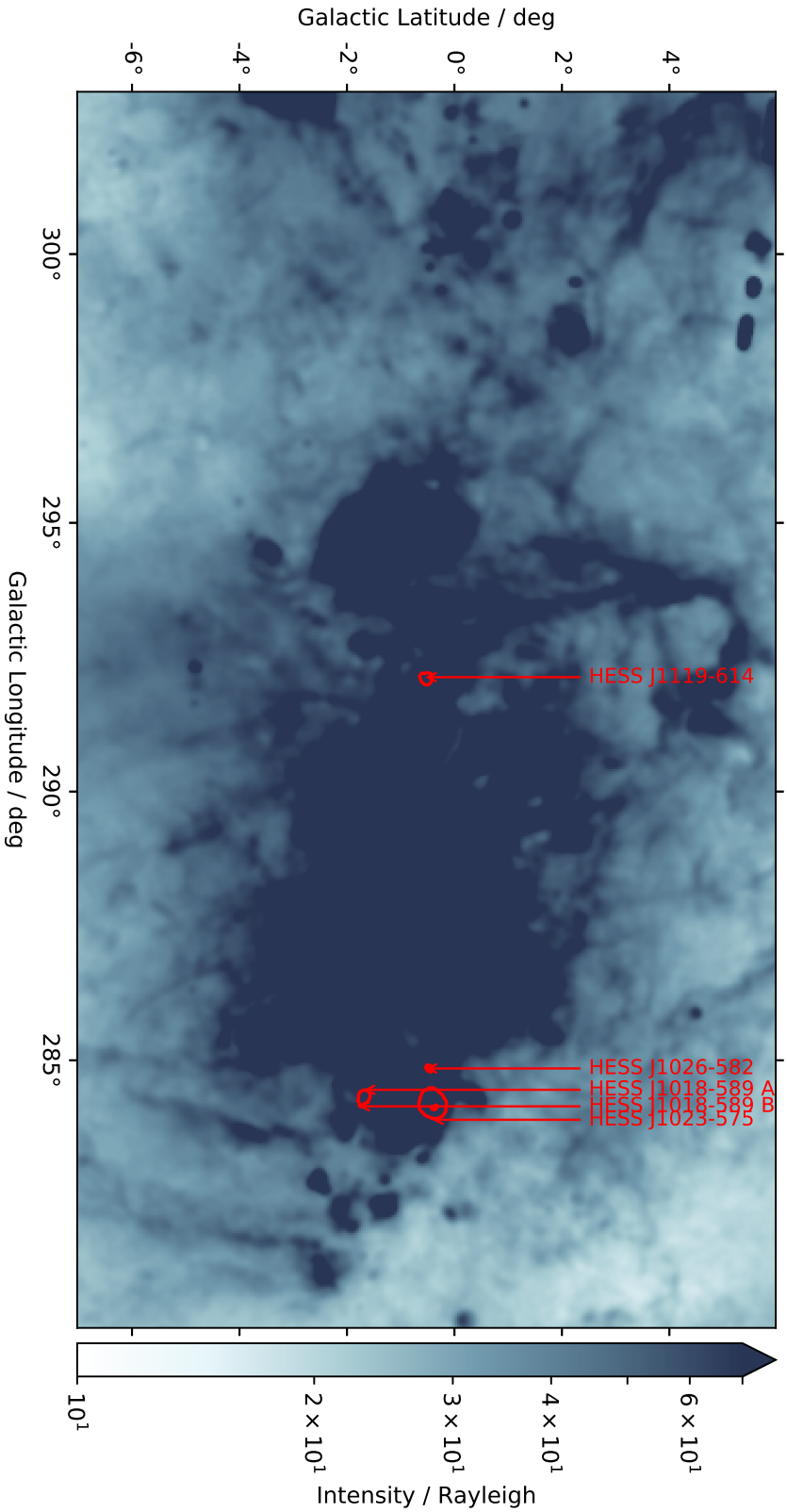
Galactic Latitude / deg
-6°
-4°
-2°
0°
2°
4°
Galactic Longitude / deg
300°
295°
290°
285°
HESS J1119-614
HESS J1026-582
HESS J1018-589 A
HESS J1018-589 B
HESS J1023-575
10^1
2×10^1
3×10^1
4×10^1
6×10^1
Intensity / Rayleigh

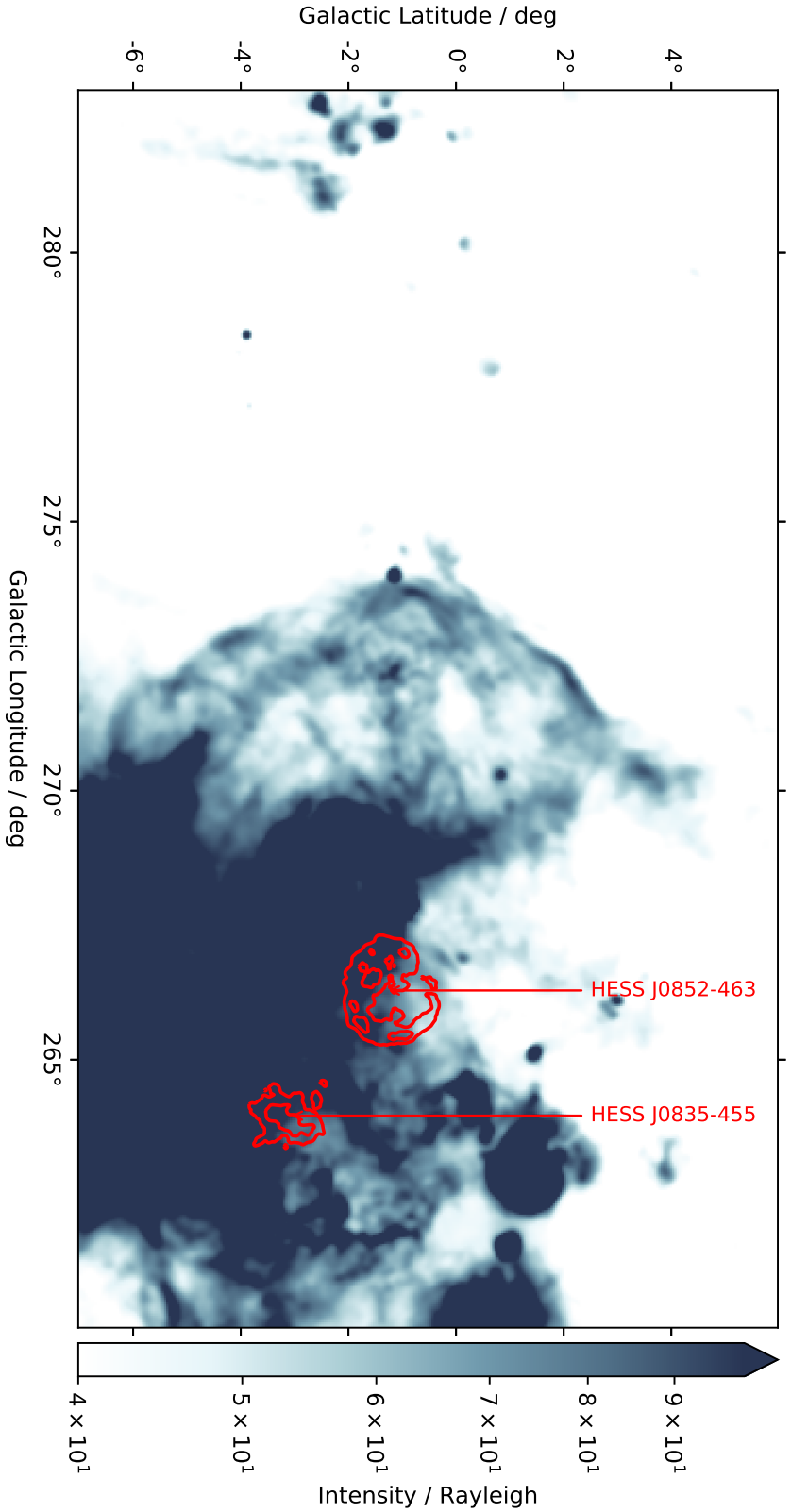
Galactic Latitude / deg
-6°
-4°
-2°
0°
2°
4°
Galactic Longitude / deg
280°
275°
270°
265°
HESS J0852-463
HESS J0835-455
4 × 10¹
5 × 10¹
6 × 10¹
7 × 10¹
8 × 10¹
9 × 10¹
Intensity / Rayleigh

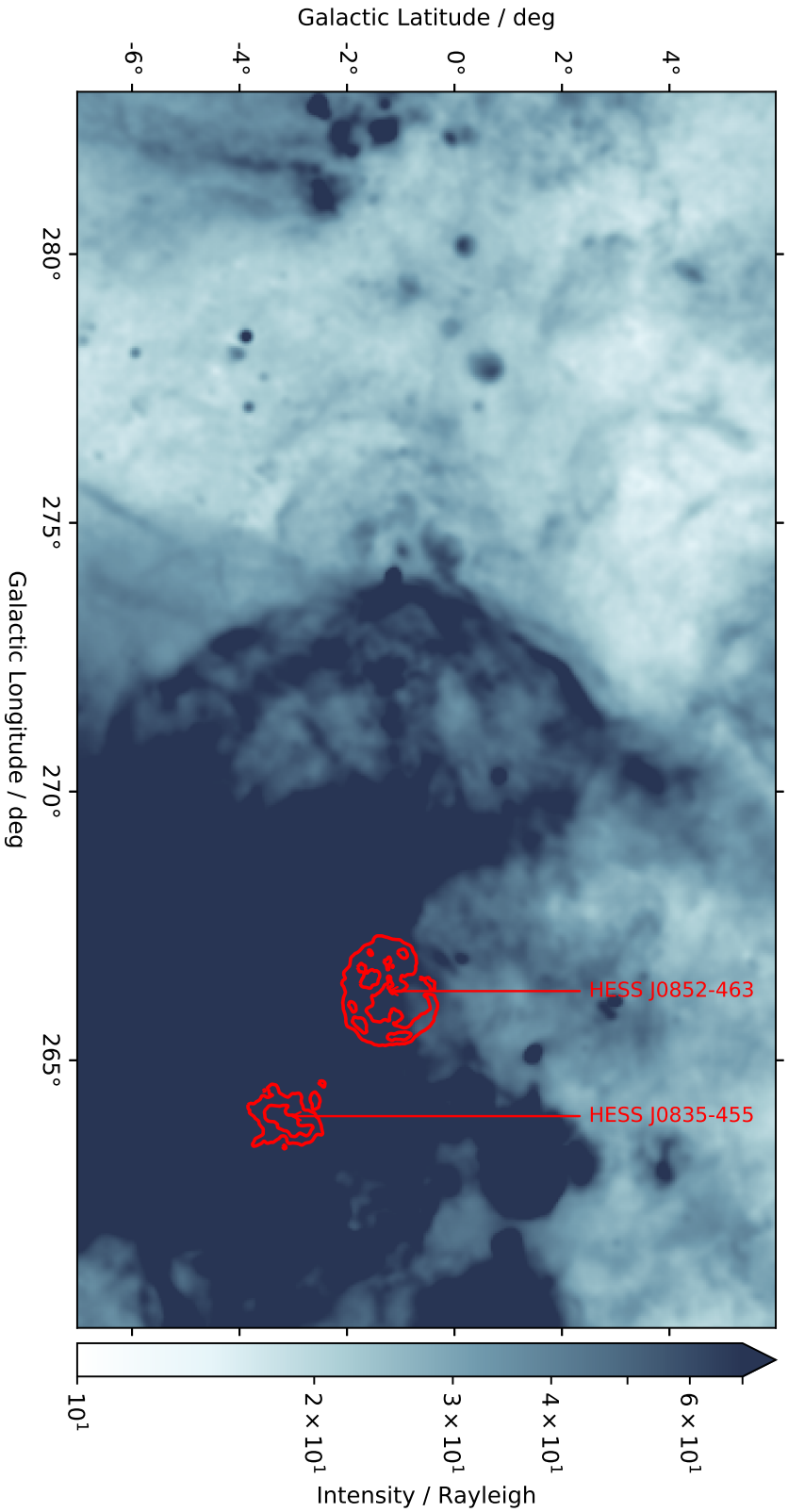
Galactic Latitude / deg
-6°
-4°
-2°
0°
2°
4°
Galactic Longitude / deg
280°
275°
270°
265°
HESS J0852-463
HESS J0835-455
10^1
2×10^1
3×10^1
4×10^1
6×10^1
Intensity / Rayleigh

Bibliography

Abeysekara, AU et al. (2017). In: *ApJ* 843.1, p. 40.

Abramowski et al. (2011). In: *A & A* 533, A103.

Acero et al. (Aug. 2013). In: *ApJ* 773.1, 77, p. 77.

Acero et al. (May 2016). In: *ApJs* 224.1, 8, p. 8.

Aharonian et al. (Oct. 1997). In: *MNRAS* 291, p. 162.

Aharonian et al. (July 2005a). In: *Science* 309.5735, p. 746.

Aharonian et al. (Sept. 2005b). In: *A & A* 439, p. 1013.

Aharonian et al. (Dec. 2006a). In: *A& A* 460.2, p. 365.

Aharonian et al. (Dec. 2006b). In: *A & A* 460.3, p. 743.

Aharonian et al. (Jan. 2008a). In: *A & A* 477.1, p. 353.

Aharonian et al. (Apr. 2008b). In: *A & A* 481, p. 401.

Aharonian et al. (June 2008c). In: *A & A* 484.2, p. 435.

Albert, J. et al. (May 2006). In: *ApJ* 643.1, p. L53.

Aleksić, Jelena et al. (2014). In: *A & A* 571, A96.

Anada, Takayasu et al. (2009). In: *PASJ* 61.sp1, S183.

Anderson, L. D. et al. (May 2014). In: *ApJ* 212, p. 1.

Angüner, O. E. et al. (Jan. 2017). In: *International Cosmic Ray Conference* 35, p. 686.

Araya, M. (May 2018). In: *ApJ* 859, p. 69.

Atwood, W. B. et al. (June 2009). In: *ApJ* 697, p. 1071.

Bania, T. M. et al. (Nov. 2012). In: *ApJ* 759, p. 96.

Bartko, Hendrik and WŁODEK Bednarek (2008). In: *MNRAS* 385.3, p. 1105.

Beall (Nov. 2014). In: *Multifrequency Behaviour of High Energy Cosmic Sources*, p. 259.

Beall, J. H. (Dec. 2003). In: *Chinese Journal of Astronomy and Astrophysics Supplement* 3, p. 373.

Becker and Helfand (May 1987). In: *ApJ* 316, p. 660.

Blair, William P and Knox S Long (2004). In: *ApJ Supplement Series* 155.1, p. 101.

Bock, D. C.-J., M. I. Large, and E. M. Sadler (Mar. 1999). In: *AJ* 117, p. 1578.

Bonnarel, F. et al. (Apr. 2000). In: *A & A* 143, p. 33.

Brisken et al. (Nov. 2006). In: *ApJ* 652.1, p. 554.

Brogan, Crystal L et al. (2005). In: *ApJ* 629.2, p. L105.

Callaway et al. (Apr. 2000). In: *ApJ* 532.2, p. 943.

Cardillo, M. et al. (May 2014). In: *A& A* 565, A74, A74.

Casares et al. (Dec. 2005). In: *MNRAS* 364, p. 899.

Castelletti et al. (Dec. 2011). In: *A & A* 536, A98.

Chang, Z. et al. (Nov. 2016). In: *MNRAS* 463, p. 495.

Clark, D. H. and J. L. Caswell (Feb. 1976). In: *MNRAS* 174, p. 267.

Corbel et al. (Oct. 2002). In: *Science* 298.5591, p. 196.

Cordes, J. M. and T. J. W. Lazio (July 2002). In: *arXiv e-prints*, astro–ph/0207156.

de Gouveia Dal Pino, Elisabete M. (Jan. 2005). In: *Advances in Space Research* 35, p. 908.

de Jager, O. C. and A. Djannati-Ataï (2009). In: *Astrophysics and Space Science Library*. Vol. 357, p. 451.

de Wilt, P. et al. (2017). In: *MNRAS* 468.2, p. 2093.

Dennison et al. (Apr. 1998). In: *PASA* 15.1, p. 48.

Dermer, C. D. and G. Powale (May 2013). In: *A & A* 553, A34, A34.

Di Palma, Irene, Dafne Guetta, and Elena Amato (2017). In: *ApJ* 836.2, p. 159.

Dopita et al. (1984). In: *ApJ* 276, p. 653.

Dubus, Guillaume (Aug. 2013). In: *A& A* 21, 64, p. 64.

Duvidovich, L. et al. (Feb. 2019). In: *A & A*, A115, A115.

Esposito et al. (2011). In: *MNRAS* 416.1, p. 205.

Fang, Li Zhang (July 2010). In: *ApJ* 718.1, p. 467.

Ferrière, Katia M. (Oct. 2001). In: *Reviews of Modern Physics* 73, p. 1031.

Fesen et al. (Feb. 1997). In: *AJ* 113, p. 767.

Fesen, W. P. Blair, and R. P. Kirshner (May 1985). In: *ApJ* 292, p. 29.

Finkbeiner, Douglas P (2003). In: *ApJ Supplement Series* 146.2, p. 407.

Frew et al. (June 2018). In: *MNRAS* 479.4, p. 4432.

Fujita et al. (Feb. 2014). In: *PASJ* 66, 19, p. 19.

Funk, S. et al. (2007). In: *A & A* 470.1, p. 249.

Funk et al. (July 2007). In: *A & A* 470, p. 249.

Gaustad et al. (2001). In: *PASP* 113.789, p. 1326.

Gotthelf et al. (June 2014). In: *ApJ* 788.2, p. 155.

Green (Aug. 2019). In: *Journal of Astrophysics and Astronomy* 40.4, 36, p. 36.

H.E.S.S. Collaboration (Jan. 2006). In: *ApJ* 636.2, p. 777.

– (Dec. 2012). In: *A & A* 548, A46, A46.

– (2014). In: *MNRAS* 439.3, p. 2828.

– (2018a). In: *A & A* 612, A8.

– (Apr. 2018b). In: *A & A* 612, A1.

– (Apr. 2018c). In: *A & A* 612, A2.

– (Jan. 2019). In: *A & A* 621, A116, A116.

Haffner, L Matthew et al. (2003). In: *ApJ* 149.2, p. 405.

Halpern et al. (Sept. 2004). In: *ApJ* 612.1, p. 398.

Halpern, EV Gotthelf, and F Camilo (2012). In: *ApJ* 753.1, p. L14.

Heng, Kevin (2010). In: *Publications of the Astronomical Society of Australia* 27.1, p. 23.

Hewitt, John W. and Farhad Yusef-Zadeh (Mar. 2009). In: *ApJ* 694.1, p. L16.

Hill et al. (2012). In: *Proceedings of the International Astronomical Union* 10.H16, p. 574.

Hughes, J. P. and D. J. Helfand (Apr. 1985). In: *ApJ* 291, p. 544.

Hunter, J. D. (May 2007). “Matplotlib: A 2D Graphics Environment”. In: *Computing in Science Engineering* 9.3, p. 90.

Izawa, Masaharu et al. (2015). In: *PASJ* 67.3, p. 43.

Kalenskii and M. A. Shchurov (Apr. 2016). In: *Astronomy Reports* 60.4, p. 438.

Kijak, Jarosław et al. (Feb. 2016). In: *MNRAS* 458.3, p. 2509.

Kirichenko, and others (Sept. 2015). In: *MNRAS* 452.3, p. 3273.

Koo, B.-C. et al. (Apr. 2016). In: *ApJ* 821, 20, p. 20.

Langston, G. et al. (June 2000). In: *AJ* 119.

Lau, J. C. et al. (Jan. 2017). In: *MNRAS*, p. 3757.

Leahy et al. (Jan. 2008). In: *AJ* 135, p. 167.

Lin, Dacheng, Natalie A Webb, and Didier Barret (2013). In: *ApJ* 766.1, p. 29.

Luque-Escamilla, Pedro L. et al. (Dec. 2015). In: *A & A* 584, A122.

Manchester et al. (Apr. 2005a). In: *The Astronomical Journal* 129.4, p. 1993.

Manchester, G. B. Hobbs, A. Teoh, and M. Hobbs (Aug. 2005b). In: *VizieR Online Data Catalog* 7245.

Marcote et al. (July 2015). In: *MNRAS* 451.1, p. 59.

Maxted, Nigel I. et al. (Oct. 2018). In: *ApJ* 866.2, 76, p. 76.

Maxted, Nigel I. et al. (Aug. 2019). In: *arXiv*, arXiv:1908.09269.

McSwain et al. (Jan. 2004). In: *ApJ* 600.2, p. 927.

Mihara et al. (July 2014). In: vol. 9144, 91441O.

Misanovic, Zdenka et al. (2011). In: *ApJ* 735.1, p. 33.

Molina and V. Bosch-Ramon (Oct. 2018). In: *A& A* 618, A146, A146.

Mori, Kaya et al. (Oct. 2017). In: *ApJ* 848.2, p. 80.

Mori et al. (Oct. 2017). In: *ApJ* 848.2, p. 80.

Osterbrock, D. E. (1989), p. 422.

Oya, S. Casanova, F. Aharonian, and M. Dalton (Oct. 2014). In: *ApJl* 794.1, L1, p. L1.

Panferov, S. N. Fabrika, and L. V. Bychkova (1993). In: Dordrecht: Springer Netherlands, p. 197.

Pannuti, Thomas G. et al. (Apr. 2017). In: *ApJ* 839.1, p. 59.

Paredes, J. M.and others (Oct. 2002). In: *A & A* 393, p. L99.

Parker et al. (Sept. 2005). In: *MNRAS* 362, p. 689.

Parker, DJ Frew, M Stupar, et al. (2004). In: *AAO Newslet* 104, p. 9.

Paron, S. et al. (June 2011). In: *A & A* 530, A25, A25.

Pavlov, O. Kargaltsev, and W. F. Brisken (Mar. 2008). In: *ApJ* 675.1, p. 683.

Petroff et al. (Oct. 2013a). In: *MNRAS* 435, p. 1610.

Petroff, M. J. Keith, S. Johnston, W. van Straten, and R. M. Shannon (2013b). In: *MNRAS* 435.2, p. 1610.

Planck Collaboration (Dec. 2011). In: *A & A*, A7, A7.

Prinz, T. and W. Becker (July 2014). In: *The X-ray Universe 2014*, p. 165.

Quireza, C.and others (Dec. 2006). In: *ApJ* 653.

Ranasinghe et al. (June 2018). In: *MNRAS* 477.2, p. 2243.

Ranasinghe and Leahy (May 2018). In: *AJ* 155.5, p. 204.

Reich, W. and X. H. Sun (Oct. 2018). In: *RAA*, 045, p. 045.

Ren, Juan-Juan et al. (Aug. 2018). In: *Research in Astronomy and Astrophysics* 18.9, p. 111.

Reynolds, S. P. (Sept. 2008). In: *ARAA* 46, p. 89.

Ribó et al. (Mar. 2002). In: *A & A* 384, p. 954.

Roberts et al. (2001). In: *ApJ Supplement Series* 133.2, p. 451.

Roberts, E. V. Gotthelf, Jules P. Halpern, Crystal L. Brogan, and Scott M. Ransom (Jan. 2007). In: p. 24.

Rosolowsky, E W aand others (Dec. 2017). In: *MNRAS* 475.1, p. 448.

Saraph, H. E. and M. J. Seaton (1970). In: *MNRAS* 148, p. 367.

Sedov, LI (1959). In: p. 210.

Sguera, V. et al. (June 2009). In: *ApJ* 697.2, p. 1194.

Shan, Su-Su et al. (Jan. 2019). In: *RAA*, 092, p. 092.

Stafford et al. (Oct. 2019). In: *ApJ* 884.2, 113, p. 113.

Stupar, M., Q. A. Parker, and M. D. Filipović (Apr. 2011). In: *APSS* 332.2, p. 241.

Stupar, M et al. (2007a). In: *MNRAS* 381.1, p. 377.

Stupar, M and Q A Parker (July 2011). In: *MNRAS* 414, p. 2282.

Stupar, Milorad and Quentin A Parker (Jan. 2012). In: *MNRAS* 419.2, p. 1413.

Stupar et al. (2007b). In: *Anglo-Australian Observatory Epping Newsletter* 112, p. 12.

Stupar and Parker (2009). In: *MNRAS* 394.4, p. 1791.

Stupar, Q. A. Parker, and M. D. Filipović (Nov. 2008). In: *MNRAS* 390, p. 1037.

Stupar, Quentin A Parker, and MD Filipović (2007c). In: *MNRAS* 374.4, p. 1441.

Su, Y. et al. (Aug. 2017). In: *ApJ* 845.

Su et al. (Dec. 2014). In: *ApJ* 796.2, 122, p. 122.

Supan, L. et al. (May 2016). In: *A & A* 589.

Sushch, Iurii et al. (Sept. 2017). In: *A & A* 605.

Takahashi, Tadayuki et al. (May 2009). In: *ApJ* 697, p. 592.

Taniguchi et al. (Oct. 2018). In: *ApJ* 866.2, 150, p. 150.

Taylor, Geoffrey Ingram (1950). In: *Proc. R. Soc. Lond. A* 201.1065, p. 159.

Tian, Wen-Wu, Z Li, et al. (2007). In: *ApJ* 657.1, p. L25.

Van der Swaluw, E.and others (Dec. 2001). In: *A & A* 380, p. 309.

Virtanen, Pauli et al. (July 2019). In: *arXiv*, arXiv:1907.10121.

Voisin et al. (2016). In: *MNRAS* 458.3, p. 2813.

Weaver et al. (1977). In: *ApJ* 218, p. 377.

Weiler, Kurt W. and Richard A. Sramek (Jan. 1988). In: *ARAA* 26, p. 295.

Werner, M. W. et al. (Sept. 2004). In: *ApJ* 36.6, p. 1048.

Williams, Brian J. et al. (Oct. 2011). In: *ApJ* 741.2, p. 96.

Yamaguchi et al. (Mar. 2018). In: *MNRAS* 474, p. 4756.

Yamamoto, Hiroaki et al. (Aug. 2008). In: *PASJ* 60, p. 715.

Yamazaki et al. (Oct. 2006). In: *MNRAS* 371, p. 1975.

Zeilik II, M. et al. (July 1975). In: *ApJ* 199, p. 401.